I. A Seismotectonic Study of the Middle America Subduction Zone

II: Lithosphere and Upper Mantle Structure of the Canadian Shield and Eastern North America

Thesis by

L. Victoria LeFevre

In Partial Fulfillment of the Requirements
for the Degree of
Doctor of Philosophy

California Institute of Technology
Pasadena, California

1990

(Submitted April 10, 1990)

Acknowlegements

The Seismo Lab is a unique place, and I wish I had taken more advantage of it while I was there. I would like to thank the faculty for their patience during my long and somewhat wandering path through the lab. For the most part they "stayed off my back" and let me do what I wanted to, and this has been very much appreciated.

I would like to acknowledge two groups of people who have been very important to me during my time at the lab. First are Holly Eissler, Marianne Walck, Pat Scott, and the other women who were already at the lab when I arrived. Their presence made my first few years much easier, they did a lot to humanize the lab, and they spared me from being the first. Second, I would like to thank all of my officemates through the years: John Ebel, Jaime Gonzalez, Chris Creaven, Holly Eissler, Pat Scott, Sally Rigden, Marcus Bursick, Jaijun Zhang, Luciana Astiz, John Louie, and Steve Grand. They are an extraordinary group of people, many of whom I never would have known well if we hadn't ended up in the same room for countless hours, and each one of whom has taught me a great deal (scientific or otherwise).

Phil Ihinger and his various housemates have provided great hospitality during my visits back over the last three years.

Finally, I would like to thank my daughter Hannah for coming along when she did and saving me from complete burnout, and the next one for coming along and making me get this done.

General Abstract

This thesis consists of two separate parts. Part I (Chapter 1) is concerned with seismotectonics of the Middle America subduction zone. In this chapter, stress distribution and Benioff zone geometry are investigated along almost 2000 km of this subduction zone, from the Rivera Fracture Zone in the north to Guatemala in the south. Particular emphasis is placed on the effects on stress distribution of two aseismic ridges, the Tehuantepec Ridge and the Orozco Fracture Zone, which subduct at seismic gaps. Stress distribution is determined by studying seismicity distribution, and by analysis of 190 focal mechanisms, both new and previously published, which are collected here. In addition, two recent large earthquakes that have occurred near the Tehuantepec Ridge and the Orozco Fracture Zone are discussed in more detail. A consistent stress release pattern is found along most of the Middle America subduction zone: thrust events at shallow depths, followed down-dip by an area of low seismic activity, followed by a zone of normal events at over 175 km from the trench and 60 km depth. The zone of low activity is interpreted as showing decoupling of the plates, and the zone of normal activity as showing the breakup of the descending plate. The portion of subducted lithosphere containing the Orozco Fracture Zone does not differ significantly, in Benioff zone geometry or in stress distribution, from adjoining segments. The Playa Azul earthquake of October 25, 1981, M_S=7.3, occurred in this area. Body and surface wave analysis of this event shows a simple source with a shallow thrust mechanism and gives

M_o=1.3x10^{27} dyne-cm. A stress drop of about 45 bars is calculated; this is slightly higher than that of other thrust events in this subduction zone. In the Tehuantepec Ridge area, only minor differences in stress distribution are seen relative to adjoining segments. For both ridges, the only major difference from adjoining areas is the infrequency or lack of occurrence of large interplate thrust events.

Part II involves upper mantle P wave structure studies, for the Canadian shield and eastern North America. In Chapter 2, the P wave structure of the Canadian shield is determined through forward waveform modeling of the phases P_{nl}, P, and PP. Effects of lateral heterogeneity are kept to a minimum by using earthquakes just outside the shield as sources, with propagation paths largely within the shield. Previous mantle structure studies have used recordings of P waves in the upper mantle triplication range of 15-30°; however, the lack of large earthquakes in the shield region makes compilation of a complete P wave dataset difficult. By using the phase PP, which undergoes triplications at 30-60°, much more information becomes available. The WKBJ technique is used to calculate synthetic seismograms for PP, and these records are modeled almost as well as the P. A new velocity model, designated S25, is proposed for the Canadian shield. This model contains a thick, high-Q, high-velocity lid to 165 km and a deep low-velocity zone. These features combine to produce seismograms that are markedly different from those generated by other shield structure models. The upper mantle discontinuities in S25 are placed at 405 and 660 km, with a simple linear gradient in velocity between them. Details of the shape of the discontinuities are not well constrained. Below 405 km, this model is not very different from many

proposed P wave models for both shield and tectonic regions.

Chapter 3 looks in more detail at recordings of P_{nl} in eastern North America. First, seismograms from four eastern North American earthquakes are analyzed, and seismic moments for the events are calculated. These earthquakes are important in that they are among the largest to have occurred in eastern North America in the last thirty years, yet in some cases were not large enough to produce many good long-period teleseismic records. A simple layer-over-a-halfspace model is used for the initial modeling, and is found to provide an excellent fit for many features of the observed waveforms. The effects on P_{nl} of varying lid structure are then investigated. A thick lid with a positive gradient in velocity, such as that proposed for the Canadian shield in Chapter 2, will have a pronounced effect on the waveforms, beginning at distances of 800 or 900 km. P_{nl} records from the same eastern North American events are recalculated for several lid structure models, to survey what kinds of variations might be seen. For several records it is possible to see likely effects of lid structure in the data. However, the dataset is too sparse to make any general observations about variations in lid structure. This type of modeling is expected to be important in the future, as the analysis is extended to more recent eastern North American events, and as broadband instruments make more high-quality regional recordings available.

Table of Contents

Part I:

A Seismotectonic Study of the Middle America Subduction Zone

Chapter 1

Stress Distribution and Subduction of Aseismic Ridges in the Middle America Subduction Zone

Note

The research described in this chapter was done from 1981-1984, and published in May of 1985. Much of the discussion in this paper concerns the subduction processes and the seismic potential of the Michoacan seismic gap. This gap was filled by the September 19, 1985 M_S = 8.1 Michoacan earthquake, the event that devastated Mexico City. That earthquake ended any discussion of whether or not the Michoacan area represented a permanent seismic gap. As of 1989, a significant seismic slip deficit remains in the Tehuantepec region, the other seismic gap discussed in this paper. An updated overview of this region can be found in Astiz (1987).

Some of the descriptions in this chapter of the seismicity in the Michoacan region (as an area of low activity and no historic large events) are no longer valid, and some of the speculation done here is no longer necessary. However, the chapter is presented here in the form in which it was published in 1985.

Abstract

The regional distribution of stresses associated with the subduction of the Cocos plate is inferred from a synthesis of 190

earthquake focal mechanisms, body and surface wave analyses of large earthquakes, and seismicity distributions. Broad patterns of consistent behavior are found across the region, from the Rivera Plate boundary in the northwest to the Guatemala/El Salvador border in the southeast, and are used as a framework to evaluate evidence for variations in local stresses that are due to the subduction of two aseismic ridges, the Tehuantepec Ridge and the Orozco Fracture Zone. Information bearing on the seismic potential at locations of aseismic ridge subduction is particularly important in that no large ($M_s \geq 7.5$) earthquakes have occurred historically.

We identify three major zones with consistent patterns in focal mechanisms and hypocentral distributions of seismicity. The first, closest to the trench and reflecting the mechanical interaction of the converging plates, is a zone of shallow thrust earthquakes extending 100–150 km inland from the trench. The second is a zone of normal faulting, beginning at about 200 km inland from the trench, $h \geq 60$ km, which extends continuously along the entire length of the descending plate throughout the region. The third distinct zone exhibits a relatively low level of activity and separates the zones of thrust and normal faulting at about 150–200 km inland from the trench. This zone extends from the Rivera plate boundary in the northwest to the Guatemala region in the southeast. At this point, the quiet region pinches out, and the thrust and normal faulting zones abut and overlap.

Superimposed on this overall pattern, we find locally only minor changes in areas of aseismic ridge subduction, aside from the prominent seismic slip gaps. Furthermore, on October 25, 1981, the Playa Azul earthquake ($M_s = 7.3$) occurred in the midregion of the Orozco Fracture

Zone. Body and surface wave analyses of this event show a simple source rupture and shallow thrust fault mechanism, as are found elsewhere in the region. The seismic moment is $M_o = 1.3 \times 10^{20}$ Nm; the calculated stress drop is 4.5 MPa, not extraordinarily high, as might be expected in these pervasive seismic gaps. An event in the Tehuantepec Ridge region, on January 24, 1983, $M_s = 6.7$, was a large, normal faulting event, but further interpretation is ambiguous because of the proximity of other normal faulting. We conclude that while aseismic slip may be occurring in the areas of ridge subduction, the possibility of large thrust earthquakes cannot be ruled out, because of the overall similarities with adjacent regions.

Introduction

The Middle America Trench marks the location of northeastward subduction of the Cocos plate under the North American and Caribbean plates. Plate geometry is shown in Figure 1.1. This is an area of rapid convergence, subduction of a very young oceanic plate, and short recurrence intervals (roughly 35 years) for large interplate thrust earthquakes (McNally and Minster, 1981). Characteristics of subduction in this area are well documented. Previous studies have detailed the structure and bathymetry of the trench and ocean floor (Klitgord and Mammerickx, 1982; Aubouin et al., 1982), accretionary processes at various parts of the margin (Karig et al, 1978; Moore et al., 1979; von Heune et al., 1980; Aubuoin et al, 1982), volcanism (Nixon, 1982; Robin, 1982; Carr et al., 1982), seismicity and seismic slip history (McNally and Minster, 1981; Singh et al., 1981), and Benioff zone geometry (Burbach et al., 1984; Dean and Drake, 1978; Molnar and Sykes,

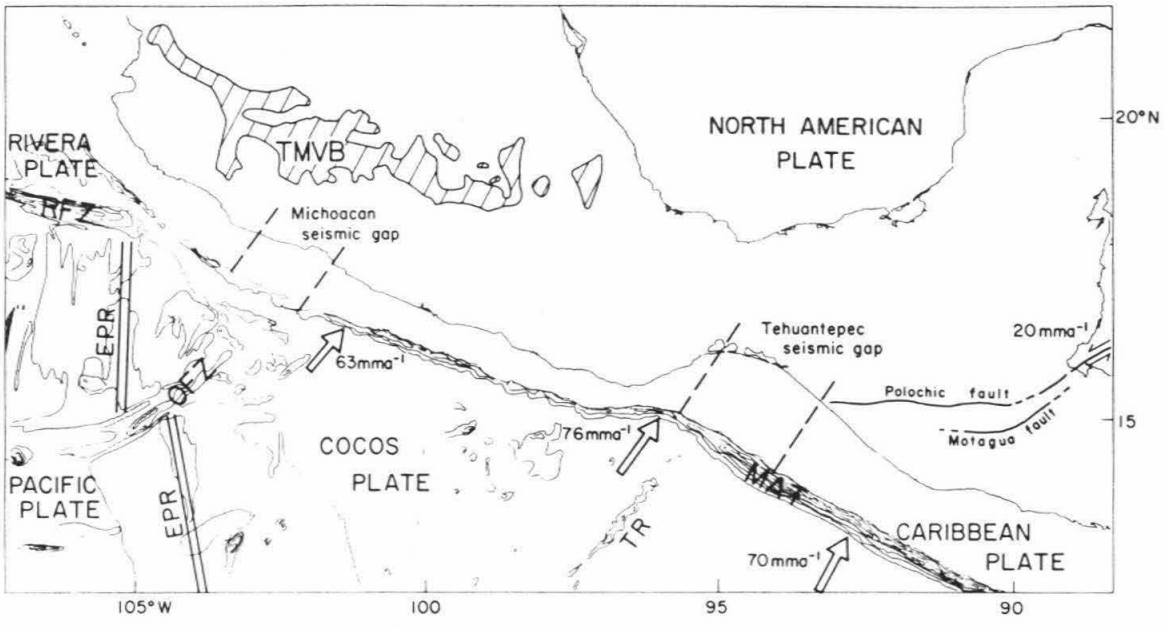

Figure 1.1: Plate geometry and bathymetry of the study area (Lambert projection). Bathymetry is from Chase et al. (1970). Contours of depth greater than 4000 m are shown for the trench. Depths less than 3300 m are shown for the ridges and fracture zones. The contour interval is 200 m. Features of the seafloor shown are the Rivera Fracture Zone (RFZ), East Pacific Rise (EPR), Orozco Fracture Zone (OFZ), Tehuantepec Ridge (TR), and Middle America Trench (MAT). The Trans-Mexican Volcanic Belt (TMVB) is also shown. Plate rates are calculated from Minster and Jordan (1978). The North American/Caribbean plate boundary on land is along the Polochic-Motagua fault system; offshore its location is uncertain but probably extends westward to roughly the area of intersection of the Tehuantepec Ridge with the trench. Both the Orozco Fracture Zone and the Tehuantepec Ridge are subducting in areas of seismic gaps.

1969).

Two topographic ridges on the oceanic plate, the Orozco Fracture Zone and the Tehuantepec Ridge, are being subducted at the Middle America Trench (Figure 1.1). The intersections of both of these ridges with the trench are the sites of gaps in large ($M_S > 7.5$) interplate thrust events and deficiency in seismic moment release. In contrast to other seismic gaps along this boundary, these areas are not known to have ever experienced a large earthquake, and aseismic subduction that is due in some way to the presence of the ridges has been suggested (McNally and Minster, 1981; Singh et al., 1981; Kelleher et al., 1973; Vogt et al., 1976). Several recent studies have discussed the effects of subduction of bathymetric features such as those found here. Effects on seismicity include a gap in large interplate thrust events (Vogt et al., 1976; Kelleher and McCann, 1976), reduced activity at shallow and/or intermediate depths (Chung, 1979; Kelleher and McCann, 1976), and a shallowing of the dip of the Benioff zone (Chung and Kanamori, 1978a; Pilger, 1981). However, in some cases these effects are clearly not found, and in the case of intermediate depth activity, the opposite effect has also been found (Chung, 1979). Focal mechanisms of events along subducted portions of ridges may be different from those of adjacent areas (Chung and Kanamori, 1978a; Richter, 1979). In the overriding plate, unusual seismic events, uplift, and other deformation have been attributed to the subducting ridge (Chung and Kanamori, 1978b; Stein et al., 1982).

These observations show that the presence of a ridge may change the stresses involved in the subduction process. Various mechanisms have been proposed to explain these effects, involving positive or

negative buoyancy of the ridge, its topographic irregularity, and weakness of the ridge relative to adjacent crust. Different mechanisms are expected to cause different changes in stress regimes in the subduction zone. For example, buoyancy of the ridge material might cause increased downdip extension along the subducted portion of the ridge, as adjacent areas subduct more easily. However, although ridges formed as hot spot traces are typically isostatically compensated, buoyant features (Detrick and Watts, 1979), other types of ridges such as fracture zones may be negatively buoyant relative to normal seafloor (Cochran, 1973; Robb and Kane, 1975; Detrick and Purdy, 1980). This negative buoyancy would decrease coupling of the plates, possibly allowing aseismic slip. The decoupling of the plates might also allow forces that normally dominate in deeper portions of the slab, such as gravitational pull, to be seen at shallower depths (Kanamori, 1977). In addition to buoyancy effects, the topographic irregularity of the ridge alone may be important, possibly being responsible for deformation of the overriding plate (Stein et al., 1982). Evoking the asperity model for plate interactions, the irregularity would create smaller, more heterogeneously distributed asperites, causing partial decoupling and smaller interplate earthquakes (see Ruff and Kanamori, 1980; Lay and Kanamori, 1981). It is also possible that the crust within ridges, particularly fracture zones, is extensively hydrothermally altered, serpentinized, and hence is more deformable, allowing aseismic slip (Engel and Fisher, 1975; Bonatti, 1976; Sclater et al., 1978; Macdonald et al., 1979). A detailed knowledge of the stress regime in the subduction zone may allow determination of which mechanisms are predominant and the way in which the ridge is

influencing the subduction process. It will obviously be necessary to know the stress orientation in adjacent, "normal" sections of the subduction zone in order to recognize any deviations that can be attributed to the ridge.

In this chapter, we survey the stress distribution and seismicity patterns in the Middle American subduction zone to characterize the stress patterns present. Our area of study extends from southern Guatemala (12^{o} N) north to the Rivera Fracture Zone (21^{o} N). Seismicity has been studied using hypocenters as reported by NOAA for the period 1962-1981. The stress distribution in the subducting plate is determined largely through focal mechanisms, 190 of which have been gathered for this study. We then look in more detail at the areas of the Orozco Fracture Zone and Tehuantepec Ridge. We also use information from two recent large events, the Playa Azul earthquake of October 25, 1981, in the Orozco area and an event on January 24, 1983, in the Tehuantepec area.

Bathymetric Features of the Northern Cocos Plate

The Orozco Fracture Zone is a broad, complex feature, yet it offsets the East Pacific Rise by only 90 km (Figure 1.1). The age difference across the fracture zone is about 2 Ma. Just east of the East Pacific Rise, the fracture zone is marked by several parallel troughs and ridges and is probably actually two narrowly separated fracture zones (Mammerickx and Klitgord, 1982). As it nears the trench, it spreads out into a still broader feature, and ridges and troughs paralleling the trench are superimposed. The average elevation of this area of seafloor is not extreme, differing by less than 200 m

from the relatively regular seafloor to the south. The complexity of the Orozco Fracture Zone, given its offset of only 2 Ma, can be attributed to its tectonic history. Several jumps in spreading ridge position and changes in pole of rotation have occurred in this area, causing the fracture zone to be reoriented (Sclater et al., 1971; Lynn and Lewis, 1976; Handschumacher, 1976; Klitgord and Mammerickx, 1982). According to the plate reconstruction of Mammerickx and Klitgord (1982), from 13 to 5 Ma, the Orozco Fracture Zone was a major tectonic feature, the plate boundary between the Rivera and Cocos plates.

The Tehuantepec Ridge is a narrow, linear feature, with maximum vertical relief of almost 2000 m. It is paralleled on both sides by small depressions and separates shallower seafloor to the north from the deeper Guatemala Basin to the south. Several recent studies point to a fracture zone origin, although its orientation is not appropriate relative to the present position of the East Pacific Rise (Lynn and Lewis, 1976; Couch and Woodcock, 1981; Schilt et al., 1982; Klitgord and Mammerickx, 1982; Mammerickx and Klitgord, 1982). Mammerickx and Klitgord (1982) detail several plate reorganization events within the last 25 Ma. Their plate reconstruction allows the Tehuantepec Ridge to be recognized as a fracture zone. The age contrast across the zone is 10-25 Ma (Couch and Woodcock, 1981). Klitgord and Mammerickx (1982) interpret the topographic Tehuantepec Ridge as a ridge on the north side of the Tehuantepec Fracture Zone, which is a broader feature.

Several studies have noted marked changes in subduction zone characteristics across the Tehuantepec Ridge. South of the ridge, the maximum depth of the trench is greater, and the depth to the Moho increases (Shor and Fisher, 1961). To the south, there is a well-

developed forearc basin, while to the north, there is not (Ross and Shor, 1965; Couch and Woodcock, 1981). Recent Deep Sea Drilling Project results indicate that active accretion is currently occurring in the northern part of the Middle America Trench but not in the southern part (Aubouin et al., 1982; Moore et al., 1979; von Huene et al., 1980). There is a normally positioned volcanic belt to the south, while to the north the volcanic belt is oblique to, and at a greater distance from, the trench. Seismicity effects include a change in dip angle, steeper to the south, and an increase in the maximum depth of earthquakes south of the ridge. The ratio of seismic slip to plate rate changes, with a greater deficiency in seismic slip to the south. There are fewer large interplate events but more small events, and recurrence intervals of large earthquakes are longer (McNally and Minster, 1981). Many of these changes have been attributed to a change in age of seafloor across the ridge. Less coupling between the plates in the south, because of the greater age of the subducting plate, may explain some of these observations (see Ruff and Kanamori, 1980). In addition, the North American/Caribbean plate boundary is in this area (Figure 1.1). The convergence rate is at least 15 mm yr^{-1} less south of this boundary (calculated from Minster and Jordan (1978)), and new estimates of North American/Caribbean motion predict that the drop in convergence rate may be much greater (Sykes et al., 1982). Uyeda (1982) proposes that the difference in convergence rate causes many of the changes in style of subduction. A recent detailed study of Benioff zone geometry (Burbach et al., 1984) suggests that some of the changes are gradational rather than in the form of a sharp discontinuity at the ridge and that the changes begin well north of the ridge.

Seismicity and Focal Mechanism Data

Seismicity for the period 1962-1981 is shown in Figure 1.2. This time period was chosen to be as long as possible while still having fairly accurate locations and complete recording of events of $m_b > 4$. Locations are taken from the NOAA catalog. Also shown are the locations of cross sections that have been prepared using the same events.

Several features of the seismicity of this area can be seen on this map. The shallow dip of the subduction zone in the north is shown by the distance from the trench to the intermediate depth activity. In the southern part of the zone, an increased overall level of seismicity is shown, and the intermediate activity moves closer to the trench as the dip of the Benioff zone increases. Slightly reduced shallow activity is seen in the Orozco area (area of cross section 2). There is a less pronounced reduction in shallow activity in the Tehuantepec area (area of cross section 9). Large thrust events are absent from this area but present to the north and south. In Guatemala, the southernmost area shown, a reduction in shallow seismicity is also seen. This area is recognized as having unusually low activity during the last 30 years and high seismic potential (McNally and Minster, 1981).

We have compiled 190 focal mechanisms for the same time period, 1962-1981. Sources for focal mechanisms are Molnar and Sykes (1969), Dean (1976), Chael and Stewart (1982), Mota (1979), Gonazlez-Ruis (1986) and 23 new mechanisms prepared for this study. The focal mechanism parameters are listed in the Appendix. New focal mechanisms that have been prepared for this study are presented in Figure 1.3.

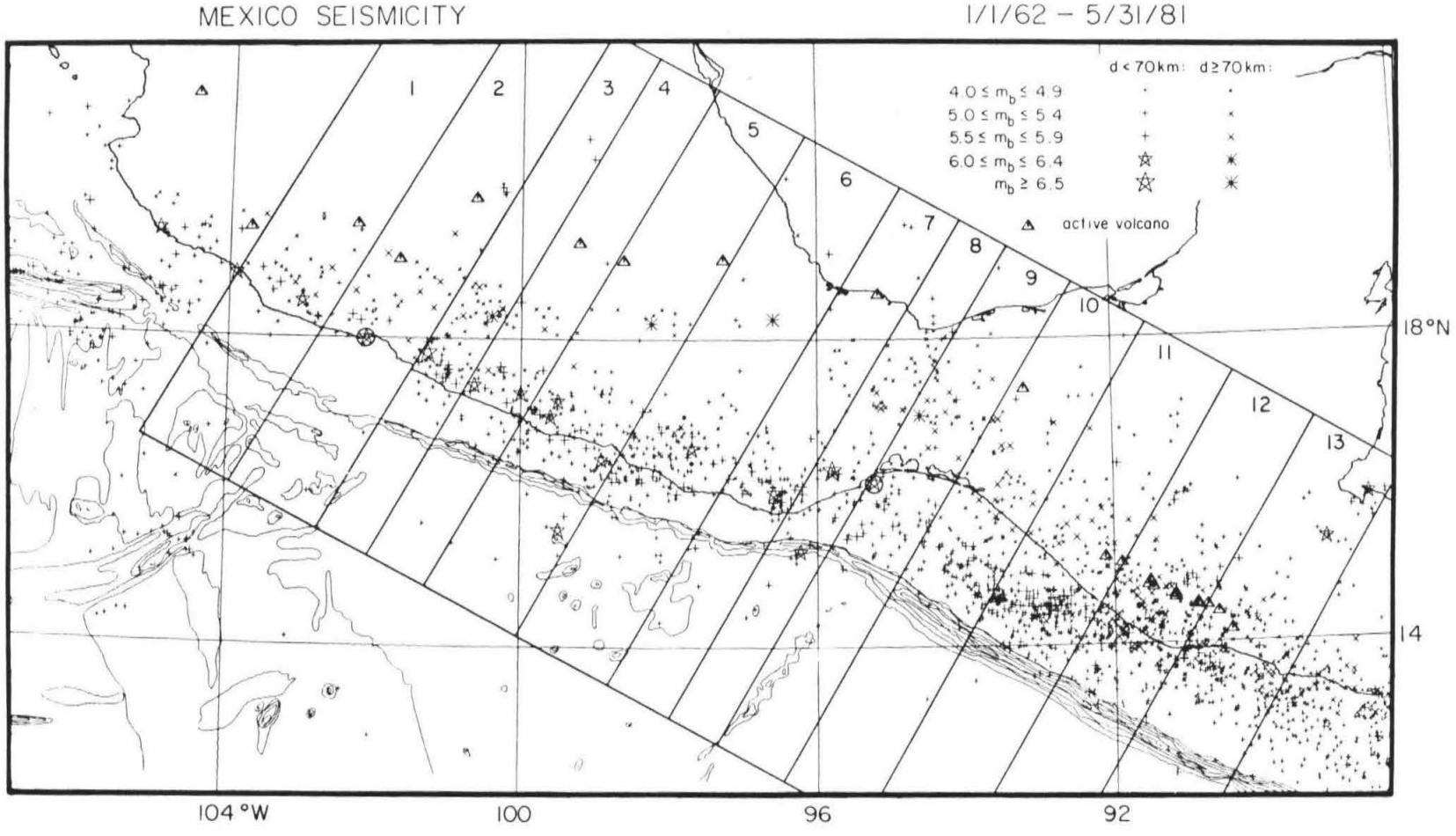

Figure 1.2: Seismicity of the study area for the period January 1, 1962, to May 31, 1981, is shown. In addition, the epicenters of the October 25, 1981, and January 24, 1983, events, which are discussed in the text, are shown and circled. The locations of the cross sections shown in Figures 5-7 are indicated.

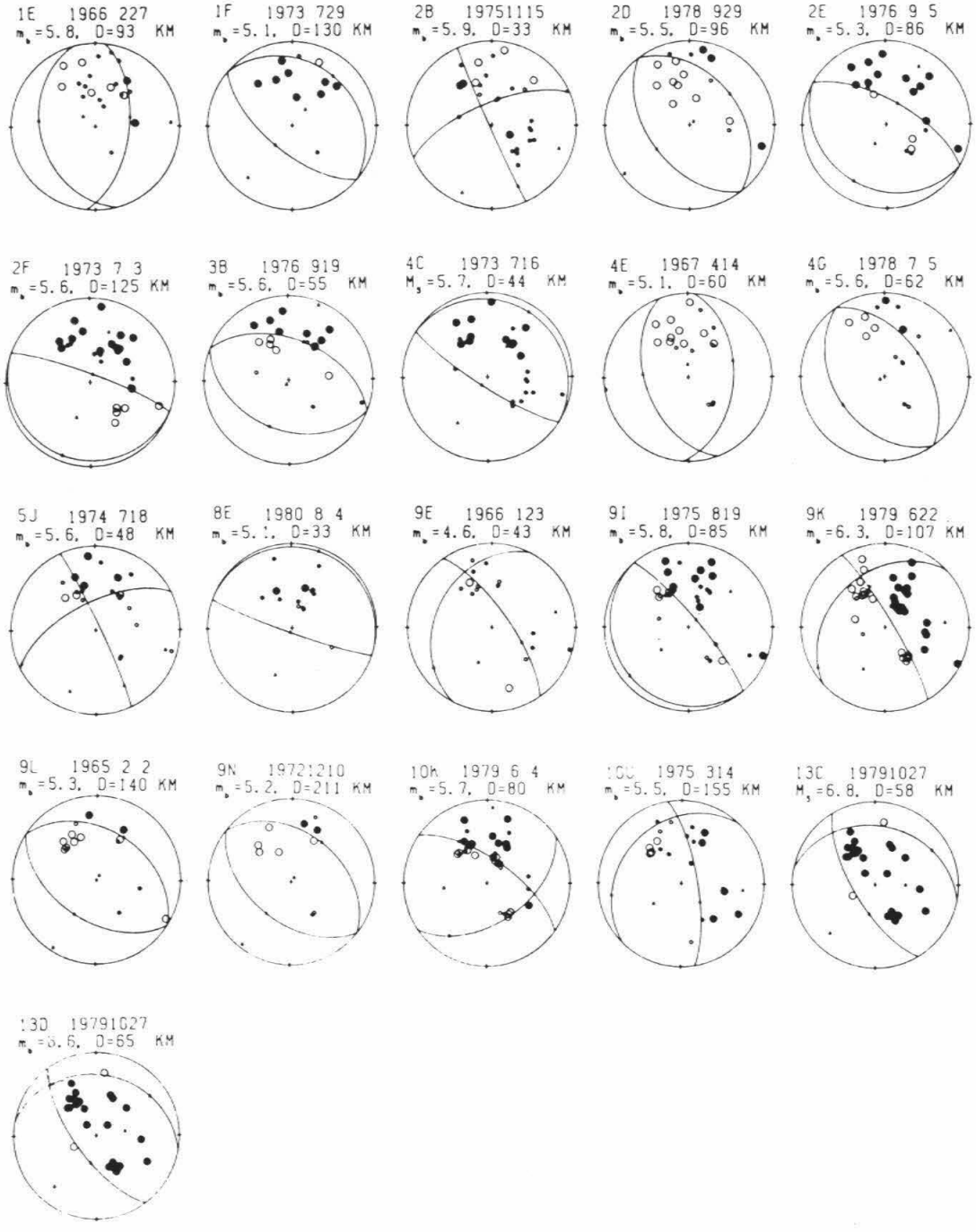

Figure 1.3: New focal mechanisms determined for this study. P wave first motions are shown, lower hemisphere projection. Solid circles indicate compression, open circles, dilatation. Smaller circles indicate less certain readings.

The mechanisms are shown in map view in Figure 1.4 and are later presented in cross section. We present almost all known mechanisms rather than eliminate some on the basis of constraint of the nodal planes. Since we hope to resolve any difference in stress distribution around the subducting ridges, it is important to have as much spatial coverage as possible. Many first-motion mechanisms from this area have poor or no data from the west and south, and some adjustments of the nodal planes are possible. However, the general character of the events, as to strike slip, thrust, or normal, is well determined.

Stress Distribution Determined from Focal Mechanisms

Cross sections through the subduction zone are presented in Figures 1.5-1.7. Hypocenters are shown on the left in each figure. On the right, the focal mechanism data of Figure 1.4 are shown projected onto the cross sections. The cross sections are oriented N30^{o}E, which is roughly perpendicular to the trench, although the trend of the trench varies by 10^{o}-20^{o}. The convergence direction is slightly oblique to the cross sections: N40^{o}E by the Orozco Fracture Zone to N36^{o}E by the Tehuantepec Ridge, as calculated from Minster and Jordan (1978). The strike of the subducted plate may not parallel the trench. In northern and central Mexico, Burbach et al. (1984) define a direction of about N12^{o}E as being perpendicular to the strike of the subducted plate, although this is not well constrained. Changes in orientation of less than about 15^{o}, which would account for any of these different directions, are not significant in the appearance of the cross sections.

All events of $m_b \geq 4$ located in this area by NOAA for the time

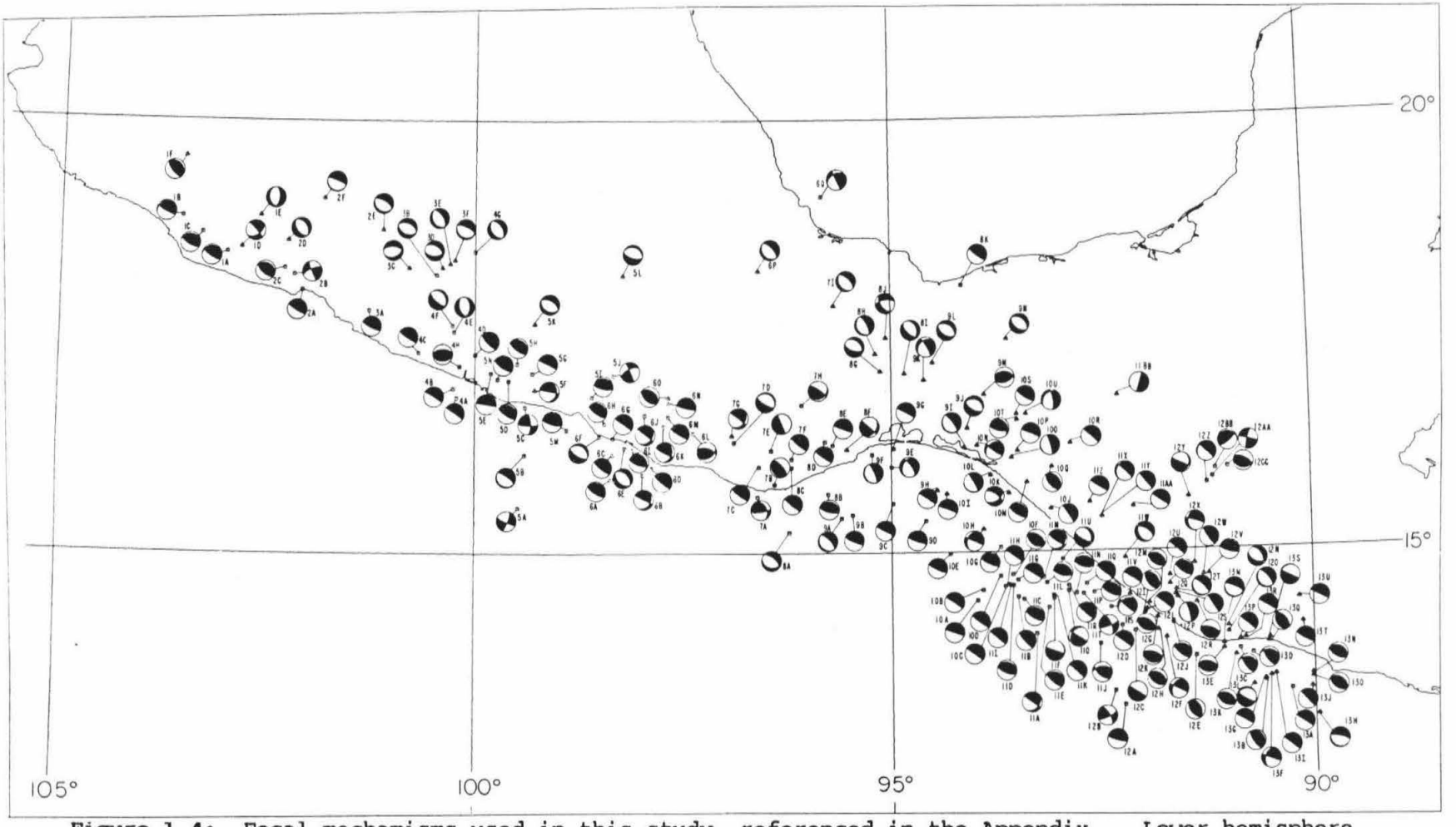

Figure 1.4: Focal mechamisms used in this study, referenced in the Appendix. Lower hemisphere projections are shown. Solid quadrants indicate compressional first mostions. Numbering indicates the cross section in which events are contained (e.g., events 3A-3F are found in cross section 3 of Figure 2, and also cross section 3 of Figures 5-7). Epicenters are shown, with squares indicating depths less than 70 km and triangles indicating depths greater than 70 km.

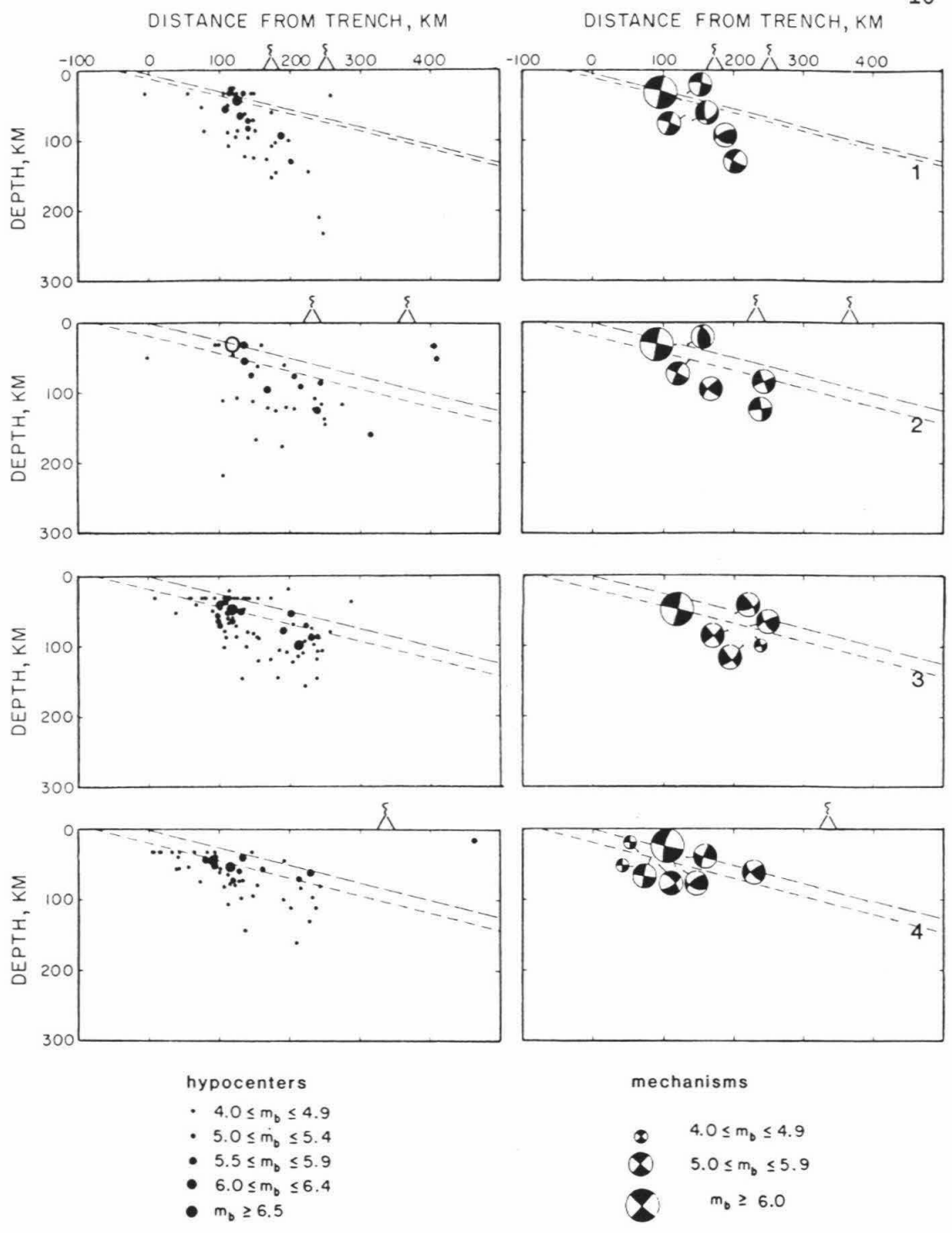

Figure 1.5: Cross sections 1-4. Location of cross sections is indicated in Figure 2. On the left, hypocenters are shown of all events with $m_b > 4$ from the NOAA catalog, January 1, 1962, to May 31, 1981. Dashed reference lines indicate hypothetical extension of interplate surface from shallow depth, from large shallow events modeled by Chael and Stewart (1982). Smaller dashes are drawn through the catalog hypocenter, larger dashes through the relocated hypocenter. On the right, focal mechanisms are shown projected on the cross section as equal-area projections of the half of the focal sphere on the side of the viewer. The Playa Azul event, $m_b = 6.2$, is shown as an open circle in cross section 2.

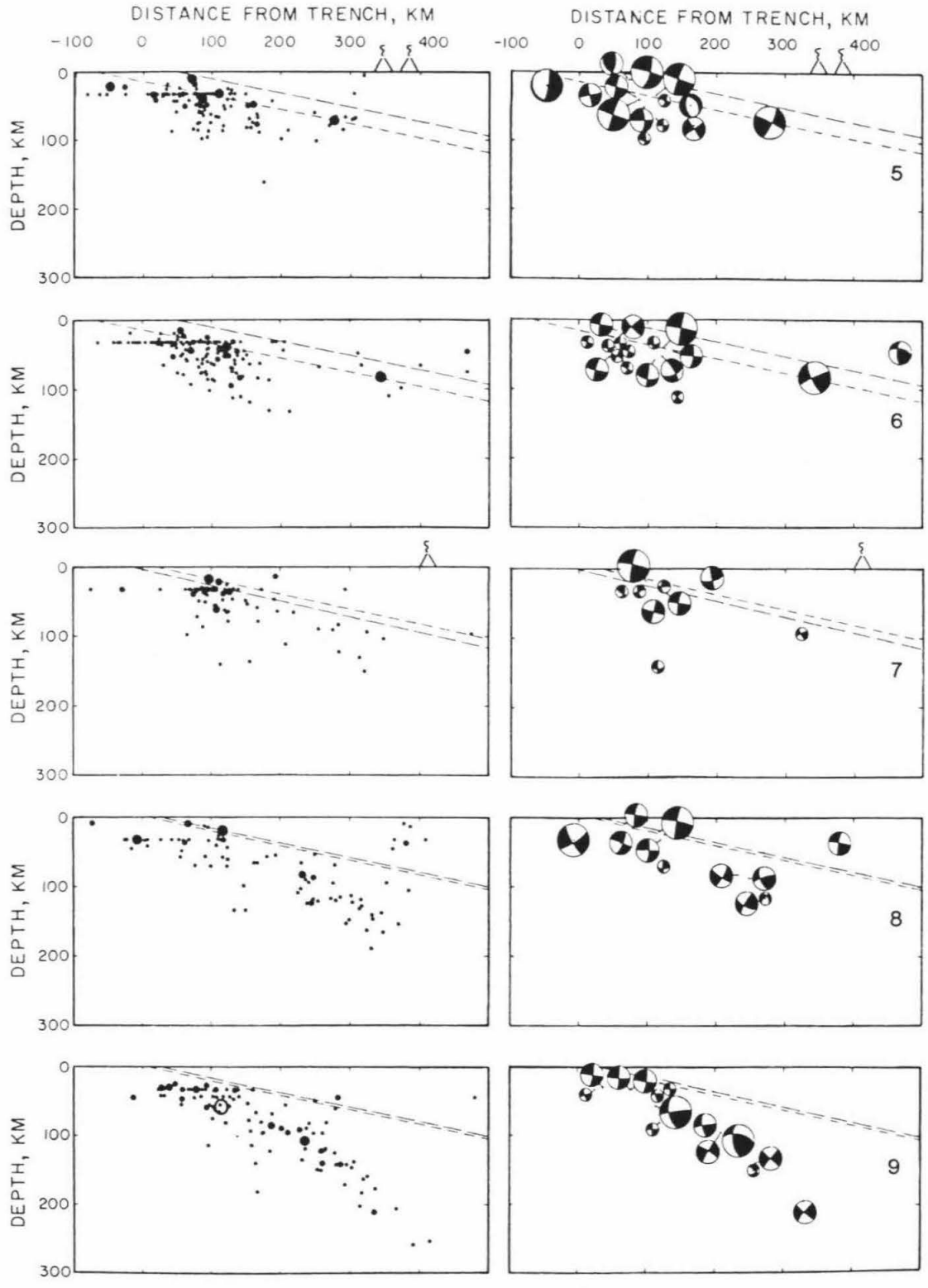

Figure 1.6: Cross sections 5-9. Symbols as in Figure 5. The Tehuantepec area event of January 24, 1983, m_b=6.3, is shown as an open circle in cross section 9.

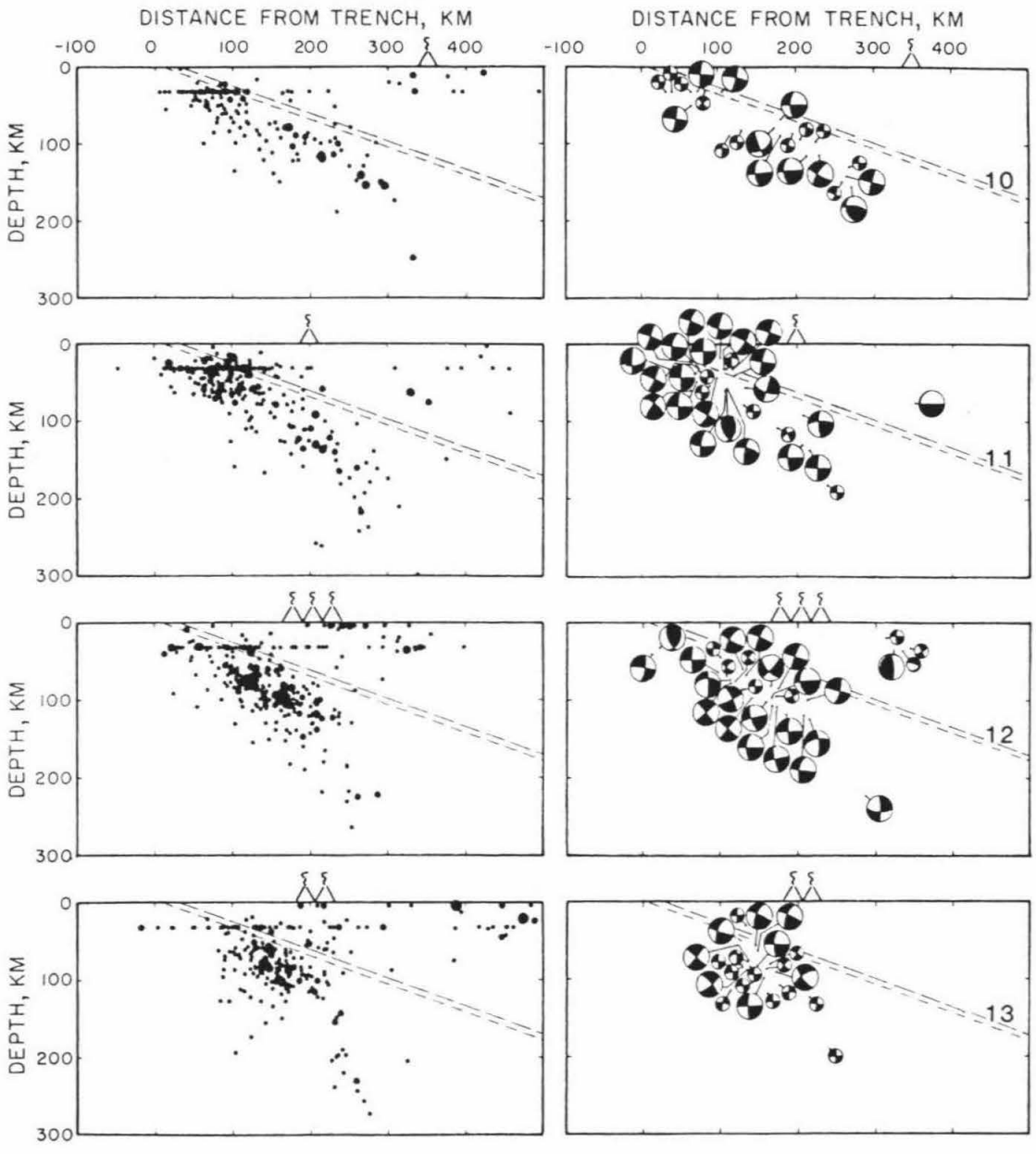

Figure 1.7: Cross sections 10-13. Symbols as in Figure 5.

period January 1962 through May 1981 are shown in the cross sections, and NOAA catalog locations are used for all of the events. There is likely to be some error in the catalog locations, with events systematically mislocated away from the trench (northeastward), and too deep because of the effect of the high velocity slab (Cruz and Wyss, 1983). However, studies by Burbach et al. (1984) and Eissler and McNally (1984) involving relocations of events in this region show that the catalog locations are generally good to within 15 km for well-recorded, large events, and good to within 25 km for events of m_b > 4.5. Although some of the events plotted in the cross sections have been relocated in the course of various studies on this region, original catalog locations are all used here for consistency. The dashed lines on the cross sections are included for reference and indicate the downdip extension of the interplate surface, where it would be located if it were completely planar and undeformed. The interplate orientation is taken from the dip angles and hypocenters of six large interplate events, which were carefully modeled by Chael and Stewart (1982), with the nearest event being used in each cross section. The smaller dashes are drawn through the catalog location of the event, and the larger dashes are drawn through the relocated hypocenter.

There are consistent overall patterns in seismicity and focal mechanisms, with variations from north to south. In seismicity, there are typically two regions of higher activity, one shallow and close to the trench, the other deeper and at over 200 km from the trench. These regions are separated by a zone of lesser activity. This pattern is seen southward through cross section 9, is less pronounced in cross

sections 10 and 11, and is no longer clear in cross sections 12 and 13. The deeper zone of activity moves away from the trench from north to south, beginning at just 200 km from the trench in cross section 1 to 300 km in the middle cross sections. On the seismicity map (Figure 1.2), the deeper zone of activity can be seen as a band of events trending almost east-west, paralleling the trans-Mexican volcanic belt, then moving back toward the shallower seismicity farther south.

Focal mechanism data show that the two regions of activity differ in the types of events that occur. The upper zone has primarily shallowly dipping thrust events, with one nodal plane paralleling the projected planar interface. Events of this type at shallow depths are seen in all of the cross sections. Focal mechanisms of events in the deeper region of activity are predominantly steeply dipping normal events. In these events one nodal plane dips northeastward (away from the trench) more steeply than the Benioff zone.

Looking in more detail at the upper region, shallowly dipping thrust events clearly predominate at shallow depths. Exceptions are a few normal events near the trench (events closest to 0 km in cross sections 8 and 5), which are interpreted as plate-bending events. A few other shallow normal events may be bending events which are slightly mislocated; for example, relocation by Mota (1979) of the shallow normal event at about 75 km in cross section 6 puts this event at the trench. Other exceptions are isolated strike-slip events, such as the large event seaward of the trench in cross section 5. Other strike-slip events are seen in cross sections 1 (175 km), 2 (150 km), 5 (175 km), 11 (100 km), and 12 (25, 300 km). In cross section 1, the strike-slip event may represent some complication from the nearby

triple junction with the Rivera plate. The event in cross section 2 is located at the northern edge of the area affected by the Orozco Fracture Zone, and its sense of movement is such that the Orozco area is advancing relative to the area to the north. The two events in cross section 5 are difficult to interpret but may represent some transverse structure in the plate. The presence in this area of a small fracture zone with almost no offset is suggested by Klitgord and Mammerickx (1982). Some of the strike-slip events in the southern cross sections may represent North American/Caribbean motion. Others are not appropriately located or oriented to relate directly to the plate boundary and probably simply reflect an overall more complex and heterogeneous stress distribution in the southern part of the subduction zone.

Steeply dipping normal events in the lower region of activity are most clearly seen in cross sections 2-9, where essentially all of the mechanisms from this zone are of this type. This can also be seen clearly on the map view (Figure 1.4), where the inland events throughout this region are normal. In the southernmost cross sections, the mechanism patterns are varied, and there are several events inconsistent with the overall pattern. Still, most of the deeper events can be interpreted as very steeply dipping normal events (with motion on the vertical nodal plane).

Cross sections 2 and 3 contain the subducted portion of the Orozco Fracture Zone. The fracture zone is quite broad and runs slightly oblique to the cross sections, so that the subducted portion about roughly 50 km is contained in cross section 2, below that, in cross section 3. The overall level of seismicity is somewhat less here, but

the distribution of hypocenters and mechanisms is not resolvably different from that of adjacent cross sections. One possible difference is the relatively large number of normal events found in cross section 3.

The downdip extension of the Tehuantepec Ridge is in sections 9 and 10, with the portion below about 75 km being in section 10. This is a transition region from the characteristics of the subduction zone in the north to those in the south. On the seismicity cross sections, it can be seen that the dip of the Benioff zone becomes steeper in this region and activity extends to greater depth. The level of activity appears higher, but the increase is actually in the number of small (m_b<5.5) events, not in overall slip or seismic moment release. These changes from the northern to the southern portions of the zone have been noted in other studies and are generally attributed in some way to the Tehuantepec Ridge. However, in the cross sections it appears that the change is gradational and that the behavior actually changes north of the downdip extension of the Tehuantepec Ridge. A similar conclusion was reached by Burbach et al. (1984) in a study of Benioff zone geometry, which used only selected, well-located events. Looking at stress distribution from focal mechanisms along subducted portions of the ridge, there may be some differences from adjacent areas. In cross section 9 there are normal-faulting events in an unusual position at about 100 km from the trench and 50 km in depth. The largest of these is the event of January 24, 1983, which will be discussed later. In cross section 10 there are several events of unusual orientation. A few of the normal-faulting events are rotated from the cross-section direction. In addition, there are more thrust mechanisms at depth in

cross section 10 than in adjacent sections.

Recent Large Events at Ridges

Two large events of considerable interest occurred while this study was being carried out. The first, the Playa Azul earthquake of October 25, 1981, ruptured the center of the Michoacan gap over the Orozco Fracture Zone (Figures 1.2 and 1.8). Results of study of surface and body waves from this event are presented here. On January 24, 1983, an event of $M_s = 6.7$ occurred near the extension of the Tehuantepec Ridge at a depth of about 60 km (Figure 1.2). We have not analyzed this event in detail but will report some general results.

Figure 1.8 shows the location of the Playa Azul mainshock ($m_b = 6.2$, $M_s = 7.3$), two foreshocks ($m_b = 5.4$, $M = 4.1$), and 15 aftershocks ($1.9 \leq M \leq 4.2$). These locations are from Havskov et al. (1983). The aftershock area of the 1973 Colima earthquake is outlined to the north, and to the south the aftershock area of the 1979 Petatlan earthquake is shown. The area between is the Michoacan gap. This area has not had a major thrust event for at least 70 years and possibly much longer, while adjacent areas to the south have been through two or three repeat cycles of thrust activity (McNally and Minster, 1981; Singh et al., 1981). The aftershock pattern of the Playa Azul event is unusual, since there are two distinct clusters of aftershocks on either side of the mainshock. Havskov et al. (1983) point out that this is in contrast to other well-studied large events along the Mexican coast, for which the aftershocks have generally clustered around the mainshock. This could suggest a complex source process for this event.

Using long-period surface wave data from the Seismic Research

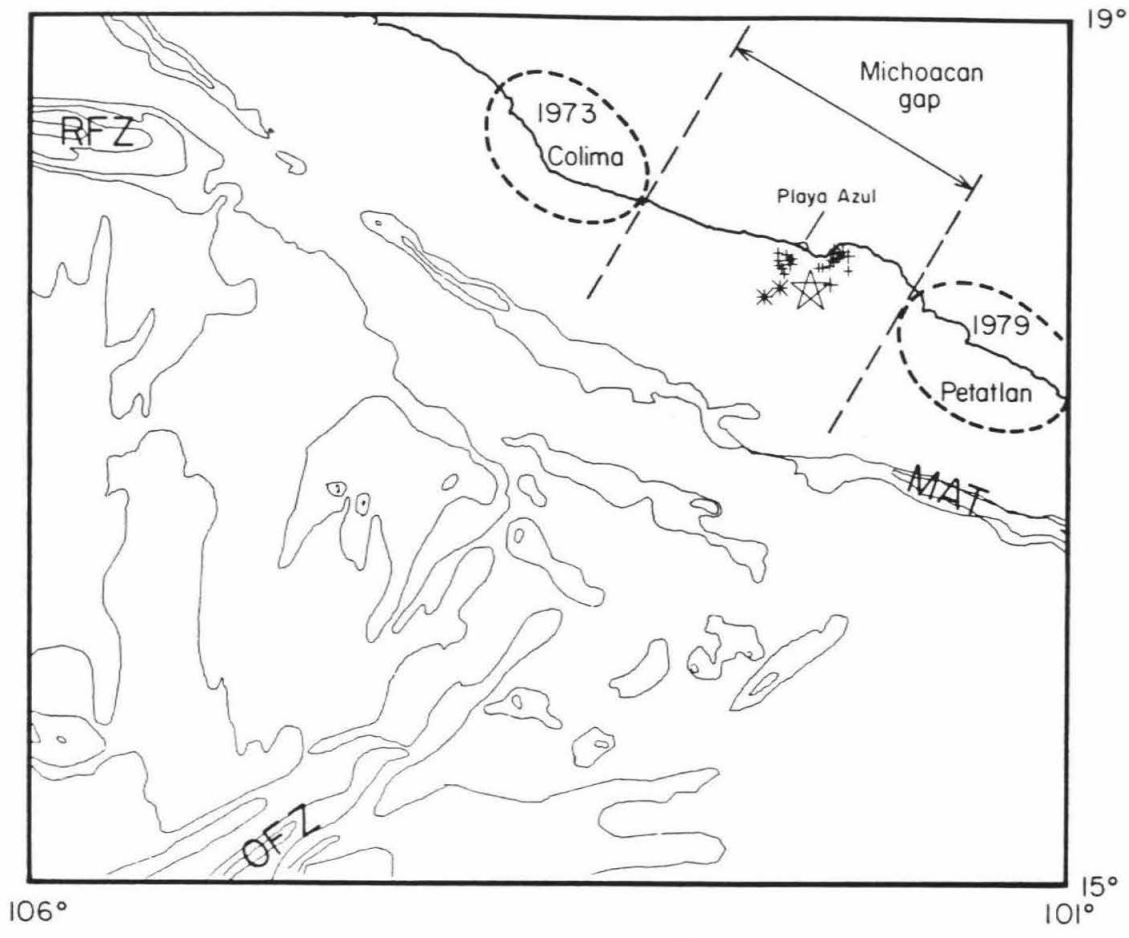

Figure 1.8: The Playa Azul earthquake sequence and its tectonic setting. The Orozco Fracture Zone (OFZ) spreads out into a broad feature as it nears the trench (MAT) in this area. The aftershock areas of the 1973 Colima and 1979 Petatlan events are indicated. The area between them is the Michoacan gap. The Playa Azul mainshock (star) occurred in this area on October 25, 1981. Asterisks indicate two foreshocks, 3 and 4 months before the mainshock. Crosses indicate aftershocks that occurred during 6 days after the mainshock. The aftershocks form two disticnt clusters. Locations are taken from Havskov et al. (1983).

Observatory digital network, we have performed an inversion to determine the source orientation and seismic moment of this event. The procedure followed is described by Kanamori and Given (1981). First-motion data were used to determine a starting model and to constrain the steeply dipping nodal plane at 79^{o} dip. A least-squares inversion was then performed to find the best-fitting double-couple source. Amplitude and phase spectra of Rayleigh waves (R1 and R2 or R2 and R3), and amplitudes of Love waves (G1 and G2 or G2 and G3) at T = 256 s were used in the inversion. Phase data were corrected for source finiteness using a source process time of τ = 30 s, as discussed by Kanamori and Given (1981). Rayleigh wave amplitude and phase data were corrected for effects of path heterogeneities in phase velocity and Q using the method described by Nakanishi and Kanamori (1982). A regionalization for Love waves had not been developed at this time, and Love wave phase data were not used because of the large effect of path heterogeneities. A source depth of 16 km was used. Figure 1.9 shows the amplitude and phase data, together with the predicted values from the results of the inversion.

Figure 1.10 shows the focal mechanism solution from the inversion, together with first-motion data. This mechanism, shallow thrust with a small left-lateral component, is essentially identical to those found for several other large interplate events along the Mexican coast by Chael and Stewart (1982). A moment of $1.34 \pm 0.10 \times 10^{20}$ Nm was obtained from the inversion. This corresponds to a moment magnitude of $M_w = 7.35$. An unusually large M_o/M_s or M_s/m_b ratio could indicate an unusual source process for this event, such as a slowly propagating rupture, which would be plausible in an area that undergoes large

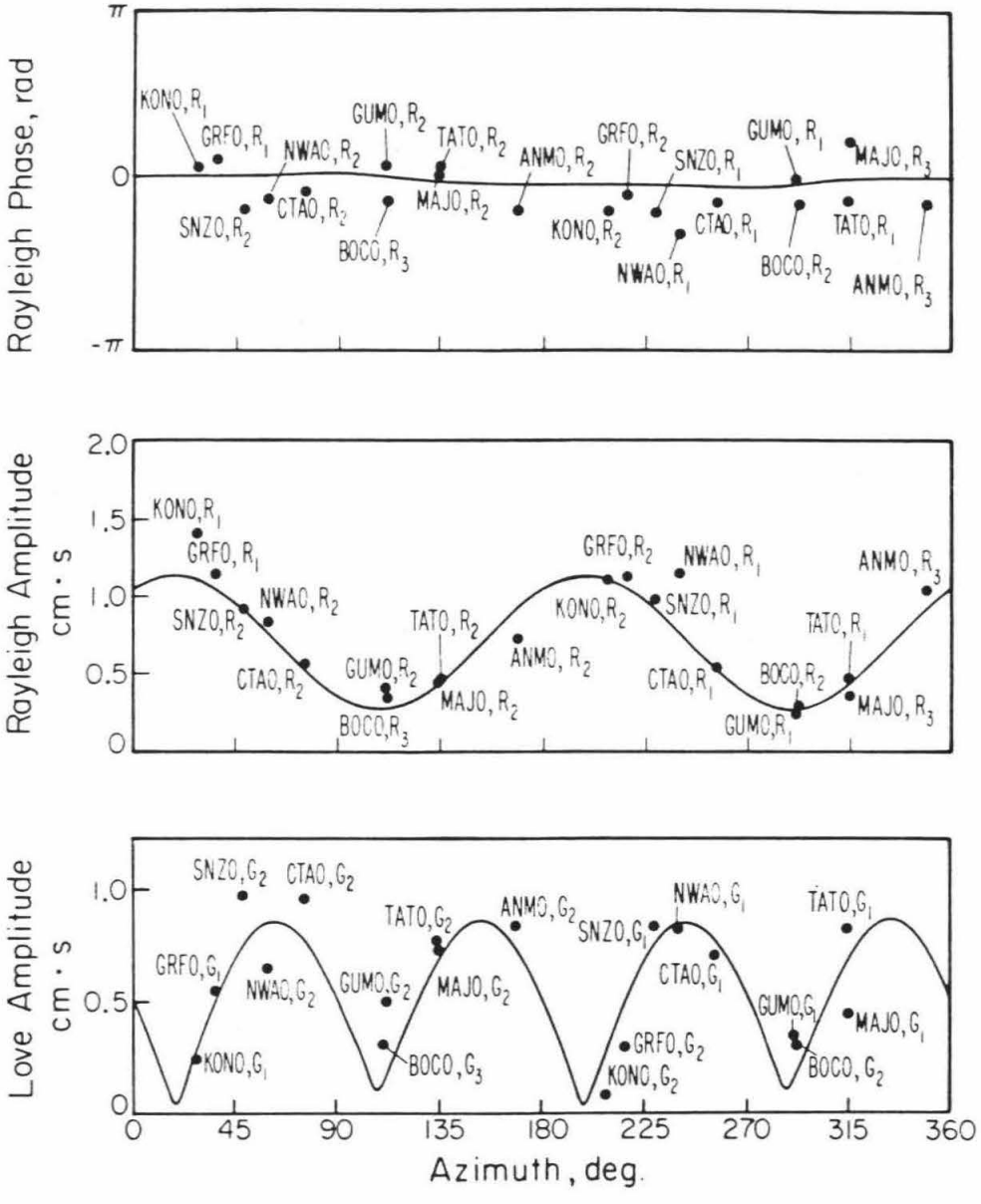

Figure 1.9: Amplitude and phase data at T=256 s, which were used in inversion for double-couple source. The solid lines represent values predicted by the results of the inversion.

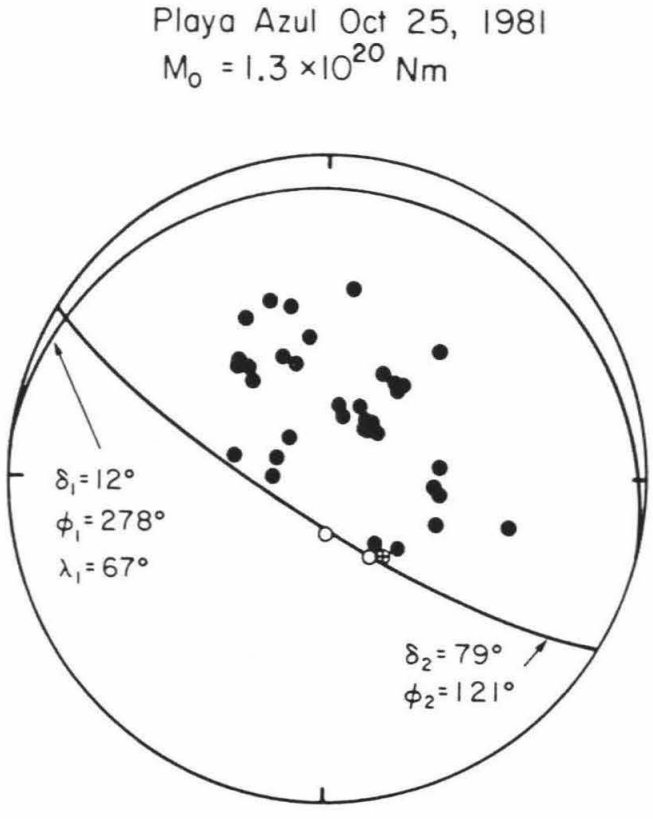

Figure 1.10: The focal mechanism of the Playa Azul earthquake determined from inversion of surface wave data is shown together with P wave first-motion data. A lower hemisphere projection is shown; solid circles indicate compression; open circles, dilatation; crossed circle, nodal character.

aseismic slip. However, m_b, M_s, and M_o scale normally here (using relations from Kanamori and Anderson (1975) and Geller (1976)), providing no evidence for any unusual source process. In addition, body waves from this event are quite simple at all azimuths and show no evidence for source complexity. Waveforms for this event, the Petatlan event of 1979, and the 1968 and 1978 Oaxaca events are virtually identical. An example of this is shown in Figure 1.11. The 1979, 1968, and 1978 events have been modeled as simple, single-source events (Chael and Stewart, 1982). We conclude that the source process of the Playa Azul event was also quite simple. This argues against the suggestion of Havskov et al. (1983), that the two aftershock clusters represent two separate asperities that broke during the event.

Stress drop can be calculated from the moment and aftershock area. This calculation is very much dependent on estimated rupture area and fault width. From Figure 1 of Havskov et al. (1983) we estimate a rupture area of 44 x 23 km from the aftershock area, which gives a rupture area of 1050 km^2 on the dipping fault plane. The stress drop was calculated for thrust fault geometry, using the same procedure as did Chael and Stewart (1982) for other events in this area. This gives a stress drop of about 4.5 MPa, somewhat higher than those found by Chael and Stewart for other large thrust events (1 MPa or less). However, it is not significantly higher than typical interplate events in subduction zones, which scatter around 3 MPa, and is much lower than typical values for intraplate events, which scatter around 10 MPa (Kanamori and Anderson, 1975).

An event of M_s = 6.7 occurred on January 24, 1983, at 16.147^{o}N, 95.232^{o}W, d = 57 km (NOAA location). This event is just north of the

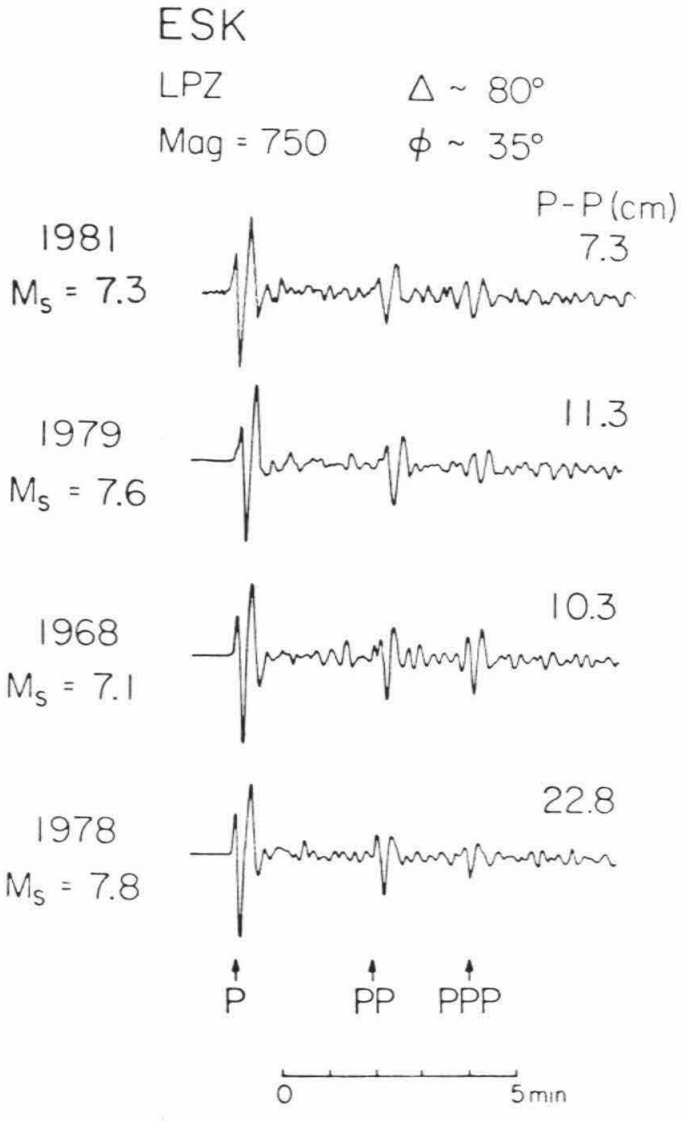

Figure 1.11: Vertical long-period World-Wide Standard Seismograph Network seismograms of P, PP, and PPP waves recorded at Eskdalemuir, Scotland (ESK) from the 1981 Playa Azul, 1979 Petatlan, and 1968 and 1978 Oaxaca events (modified from Stewart et al. (1981)). The waveforms are simple, indicating little or no source complexity, and are virtually identical, indicating that the orientation and rupture process of the Playa Azul event was much like that of other large thrust events in this subduction zone.

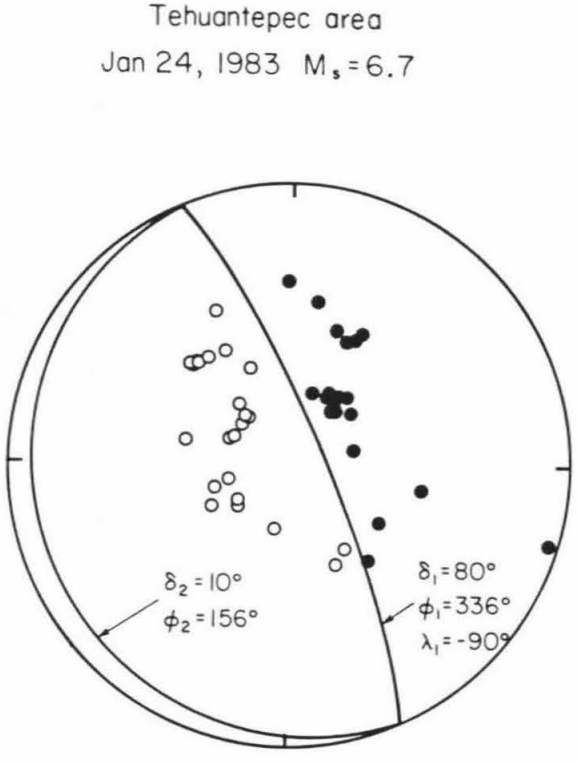

Figure 1.12: First-motion focal mechanism of the Tehuantepec area event of January 24, 1983. Solid circles indicate compression; open circles, dilatation. Lower hemisphere projection.

extension of the Tehuantepec Ridge (Figure 1.2). A first-motion focal mechanism is shown in Figure 1.12. This event is extensional and occurs somewhat closer to the trench than similar events in other cross sections. It is also among the largest normal events in this study.

Discussion

Overall Stress Distribution

North of the Tehuantepec area, the seismicity and stress distribution patterns are quite consistent. Thrust activity occurs at shallow depths, followed downdip by a zone of low seismic activity, which is then followed by a zone of steeply dipping normal events. There is a gradual transition in the Tehuantepec area to a pattern characteristic of the southern part of the zone. In the south there are again thrust events at shallow depths, followed downdip by normal events. However, the zone of low seismic activity is not seen, and the zones of thrust and normal activity overlap.

The consistent pattern in distribution of events can be interpreted in terms of the geometry of the interacting plates (Figure 1.13). The thrust events at shallow depth are largely due to slip on the interplate surface. The thickness of this zone is 50 km in several cross sections. Although many of the deeper events are smaller, and thus probably less well located, it is possible that some of this scatter is real. These deeper thrust events could indicate deformation within the subducting plate. Thrust events in a similar location were found by Malgrange and Madariaga (1983) in the Chilean subduction zone. In their study, events were well located below the interplate boundary. Intraplate compressional events are also found in the upper layer of

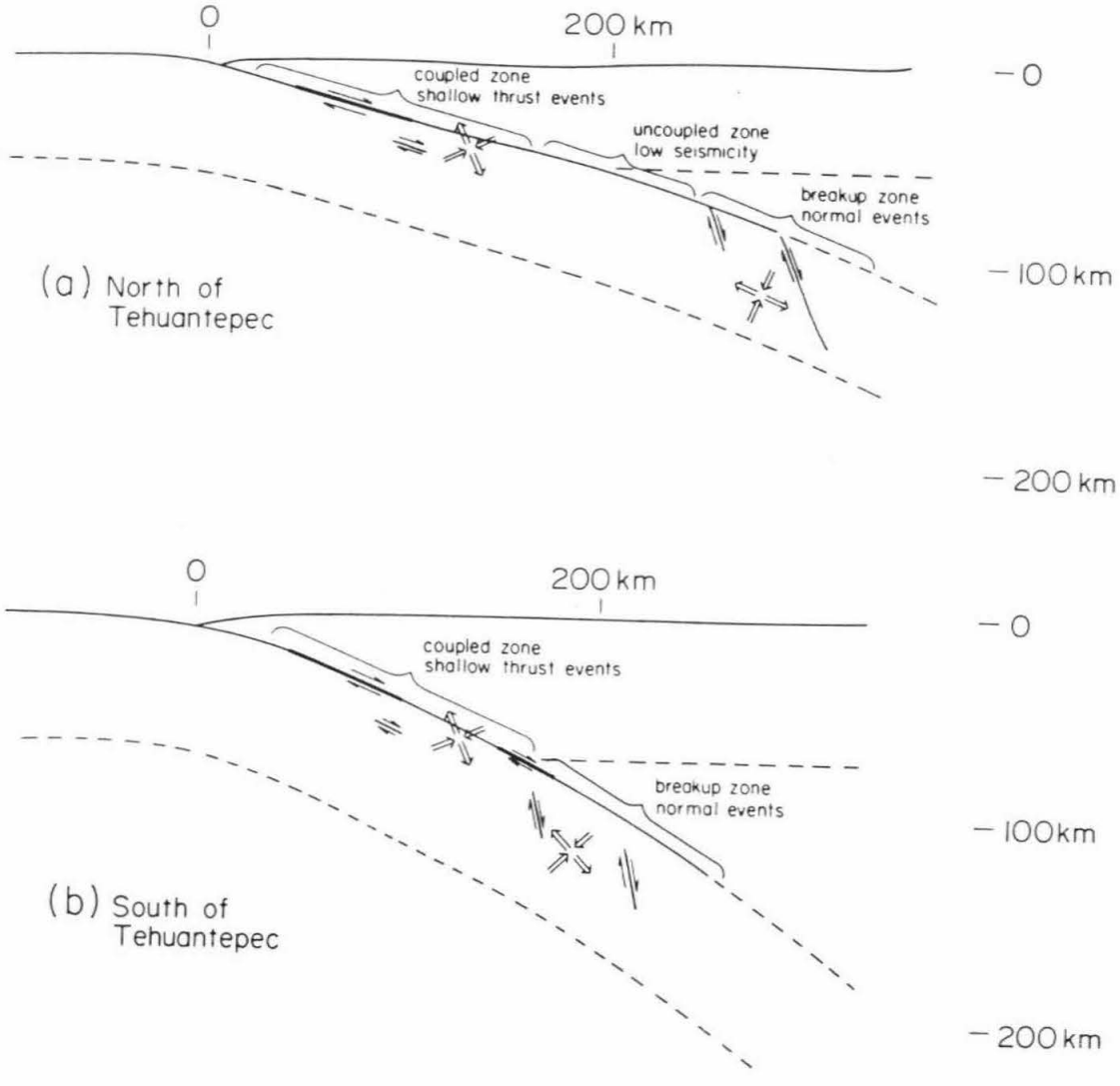

Figure 1.13: Model of plate interaction and stress distribution characteristic of this subduction zone. Double arrows show P and T axis orientations. In the northern part of the study area a zone of low seismicity is seen after the plates have become decoupled, but before the breakup of the plate begins. In the south, this effect is not seen. Normal and thrust events may have the same epicenters, with thrust events occurring on the plate interface and normal events occurring within the plate.

double Benioff zones (Hasegawa et al., 1978; Fujita and Kanamori, 1981). Although we do not discern a double Benioff zone here, the location of these events is similar.

The zone of low seismic activity begins typically at 50 km depth. This quiet zone indicates that there is little interaction between the plates in this area and little stress release within the plate as well. This is the depth at which decoupling of the plates is proposed by Ruff and Kanamori (1983), possibly initiated by phase changes within the subducting plate. This may also represent the base of the brittle lithosphere of the overriding plate. In the south, thrust events occur at increasing depths, and the quiet zone is less pronounced or not seen at all. There are several possible explanations for this change in behavior. The higher dip of the Benioff zone may tend to obscure the quiet zone. The older, colder plate here may undergo phase changes less rapidly and so remain coupled longer, or the base of the lithosphere in the overriding plate may lie at a great depth.

In the zone of normal events, most fault planes dip more steeply than the Benioff zone. This implies that these events are breaking into the subducted lithosphere, and this activity is therefore interpreted as the breaking up of the descending plate. This can be demonstrated in particular by the large events in cross sections 5 and 6. These events occur quite close to the hypothetical extension of the plate interface, and their identification as to upper or lower plate events is crucial to their interpretation. These events have been the subject of detailed study by Gonzalez-Ruis (1986). Body-wave modeling confirms depths just on or below the hypothetical plate interface. Tensional events of this magnitude and depth would be quite unusual

within a continental plate, and would indicate an extensional regime dominating throughout the upper plate, unlikely in this environment. We interpret these events as occurring within the lower plate. The event in cross section 6 is large enough (with typical dimensions of 35-50 km for an event of this size) and oriented such that it could have broken through most of the descending lithosphere. The event in cross section 5 is of similar size. Its northeastward dipping nodal plane almost parallels the Benioff zone and makes its interpretation more ambiguous. However, Gonzalez-Ruis (1986) chooses the nodal plane which is steeply dipping toward the southeast as the fault plane. This event then may also have broken through a substantial portion of the descending plate. Events in other cross sections are smaller but more numerous and form a continuous zone with the two large normal events. These smaller events are interpreted as part of the same process, though each individual event is not large enough to break through the lithosphere.

Normal events such as those found in this study, at similar depths, have been recognized in several other subduction zones (Isacks and Molnar, 1971; Stauder, 1973, 1975; Malgrange and Madariaga, 1983). These events suggest that the pull of the subducted slab is important in these zones, creating a downdip extensional stress regime. Another factor may be the effect of the overriding continental plate, which tends to push down the subducting lithosphere. This could be important here since the plate is subducting at a shallow angle.

The onset of normal activity is at about 175 km from the trench and 60 km in depth but varies along the subduction zone. No definite correlation with factors such as plate age or time since subduction can

be found. North of the Tehuantepec Ridge, the normal events seem to shift slightly inland from north to south. This might suggest some correlation with plate age, which increases from north to south. However, south of the Tehuantepec Ridge the plate is much older, and normal faulting again occurs closer to the trench. It is interesting to note that in the northern area, the zone of normal events seems to parallel the trans-Mexican volcanic belt rather than to parallel the trench.

Seismic activity terminates beyond the zone of normal events, abruptly in the north and more gradually in the south. Beyond this, the broken-up slab must subduct aseismically or become incorporated into the mantle. Nixon (1982) postulates an aseismic extension of the subducting lithosphere east to the trans-Mexican volcanic belt.

Several studies have attempted to characterize subduction zones as downdip compressional, extensional, or mixed at intermediate depths and to correlate this with various other properties of the zone such as age of plate, convergence rate, and depth of Benioff zone (Isacks and Molnar, 1971; Fujita and Kanamori, 1981; Vassiliou, 1983). Figure 1.14 summarizes our data on the overall stress distribution in this subduction zone. Compression and tension axes are plotted from all events (except outer-rise and upper-plate events). This approach eliminates the ambiguity of choosing one of the nodal planes as a fault plane. Regions north and south of the Tehuantepec Ridge are shown separately because of the change in dip of the Benioff zone. Shallow and intermediate events are also shown separately. Above 70 km, shallowly dipping thrust mechanisms, reflecting the interplate geometry, dominate. Below 70 km the stress orientation within the

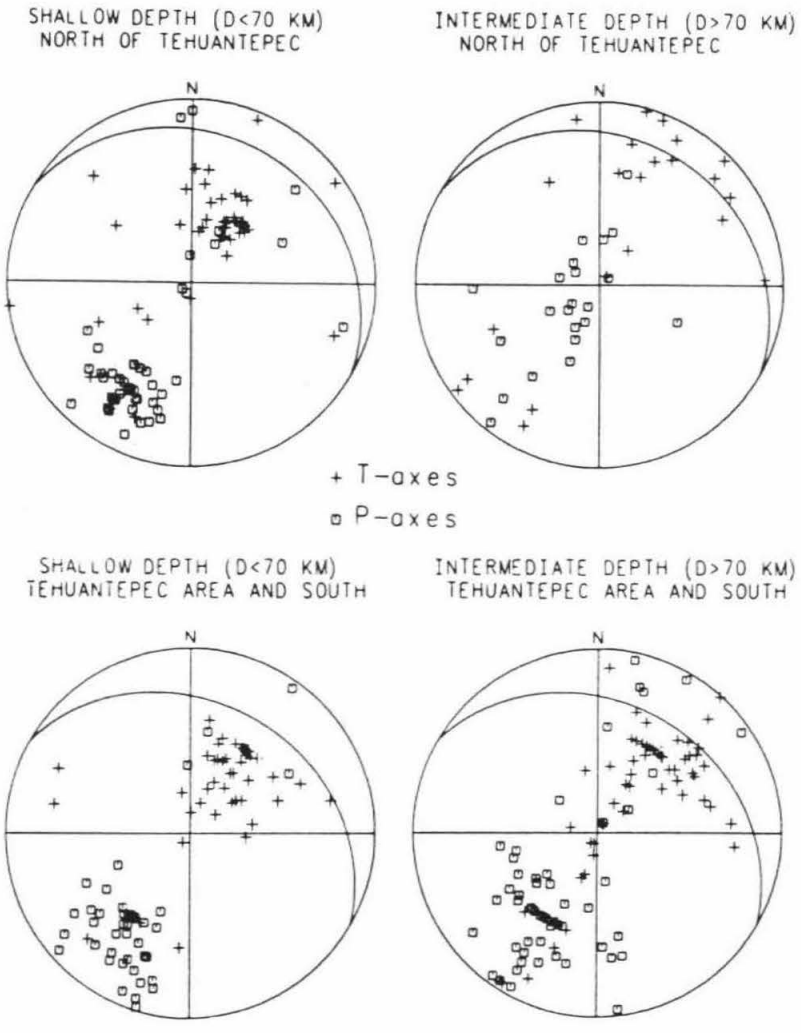

Figure 1.14: P and T axes from all focal mechanisms, excluding presumed outer-rise and upper-plate events. The arcs represent the orientation of the Benioff zone.

subducting slab is shown. Downdip tension predominates both in the north and south, although south of Tehuantepec the tension axes dip slightly more steeply than the Benioff zone does, on the average. In the south the difference in stress axis orientation between shallow and intermediate depths is relatively minor, about 15^{o}, showing that the zones of thrust and normal activity actually represent a rather subtle change in stress-axis orientation. In the north this difference is greater, roughly 35^{o}.

Effects of Ridges on Stress Distribution

The Orozco Fracture zone enters the trench at an area of large deficiency in seismic slip. There are several possibilities for the state of stress on this portion of the interplate surface. If this area is strongly coupled, the stress buildup should be quite high; if aseismic slip is taking place, it could be quite low; if partial aseismic slip is taking place, it could be similar to other parts of the subduction zone. The Playa Azul earthquake gives no evidence for unusual stresses here. The seismicity in this area is not different from that of adjacent areas, and stress distribution from focal mechanisms also shows no difference.

The origin of the Orozco Fracture zone as a major, tectonically complex feature suggests that the crust here could be weaker and more deformable. However, the Playa Azul earthquake shows that stresses leading at least to moderate-sized earthquakes can be built up here. The Orozco Fracture zone is a broad feature, and the area of irregular seafloor actually extends south farther than the Michoacan gap, into the area that experienced the major 1979 Petatlan earthquake (Figure

1.8). This further suggests that the Orozco area could be capable of producing a large interplate event. If this is true, the current state of stress on this portion of the interface is difficult to evaluate. A large stress buildup would be suggested by the seismic-slip deficit. The stress drop of the Playa Azul event was slightly higher than typical for this zone but not a high stress drop compared to events in other subduction zones. Partial aseismic slip in this area is a possibility. In any case, the seismic potential of this area is unknown, but the possibility of a large event cannot be ruled out.

The Tehuantepec Ridge enters the subduction zone in an area of gradational change in the characteristics of the zone. Any effects that are due specifically to the ridge are superimposed on this change. Comparing the Tehuantepec area to adjacent regions, no obvious difference in Benioff zone geometry is seen along the extension of the ridge. Most features of the seismicity and focal mechanism patterns are not changed, although the recent extensional event near the ridge may indicate some difference in stress distribution. This event could show resistance to subduction by the ridge, which would point to a buoyancy effect. Alternatively, this could represent the downdip extension normally found at slightly greater depth, here transmitted to shallower depth. This might be expected if the plate were decoupled in this area, which would, in turn, suggest the possibility of aseismic subduction. Unfortunately, the effect of the ridge in this region is fairly subtle, and it is not obvious which mechanism, if any, is at work. It is interesting to note that the Tehuantepec Fracture Zone may actually lie to the south of the Tehuantepec Ridge and that the seismic gap also extends in this direction, although the gap is probably wider

than the fracture zone. This geometry could be explained if the mechanical properties of the crust of the fracture zone differed in such a way as to allow aseismic slip. However, although the seismic gap here has persisted for probably two centuries, we still cannot show conclusively that aseismic slip is occurring. Since this area appears similar in many ways to adjacent ones that have had large thrust events, such an event here must still be considered a possibility.

Conclusions

1. A consistent pattern of seismicity and stress distribution is seen throughout the subduction zone. A zone of interplate thrusting at shallow depths is separated by a zone of little seismic activity from a zone of normal faulting at intermediate depths. The zone of little seismic activity is interpreted as an area where the plates have become decoupled. The normal activity farther downdip is interpreted as the breaking up of the descending plate.

2. Systematic variations are seen along the subduction zone in depth extent of activity, dip of Benioff zone and overall level of seismic activity. Most changes occur gradationally over about 200 km, beginning just north of the Tehuantepec Ridge.

3. The Playa Azul event of October 25, 1981, $M_o = 1.3 \times 10^{20}$ N m, was a simple, shallowly dipping thrust event typical of this subduction zone. It did not fill the Michoacan gap.

4. The $M_s = 6.7$ Tehuantepec event of January 24, 1983, a normal event,

may show some increased extensional stresses here, indicating resistance to subduction by the ridge. Alternatively, it may reflect the stress field at greater depth, transmitted upward here because of decoupling of the plates.

5. Changes in stress distribution along subducted portions of the ridges are either minor (Tehuantepec) or nonexistent (Orozco). No changes in Benioff zone geometry were found. The only major difference is the lack of large interplate events.

6. Aseismic subduction may be occurring in these areas. However, the possibility of large interplate thrust events in the future cannot be ruled out.

Acknowledgements

We thank Hiroo Kanamori, Jason Saleeby, Eli Silver, Jim Gill, and Mark Reagan for helpful discussions. Jens Havskov, G. V. Burbach, and Jaime Gonzalez-Ruis provided results of their work prior to publication. Luciana Astiz supplied the first-motion data for the event of January 24, 1983. Helpful reviews were provided by Holly Eissler, Luciana Astiz, Hiroo Kanamori, and anonymous reviewers. This research was supported by U.S. Geological Survey contracts 14-08-0001-21223 and 14-08-0001-21225, and by a National Science Foundation Graduate Fellowship.

References

Astiz, L., Source analysis of large earthquakes in Mexico, part I, Ph.D. thesis, Calif. Inst. of Technol., Pasadena, 1987.

Aubouin, J., J. F. Stephan, J. Roump, and V. Renard, The Middle America Trench as an example of a subduction zone, Tectonophysics, 86, 113-132, 1982.

Bonatti, E., Serpentinite protrusions in the oceanic crust, Earth Planet. Sci. Lett., 32, 107-113, 1976.

Burbach, G. V., C. Frohlick, W. D. Pennington, and T. Matumoto, Seismicity and tectonics of the subducted Cocos plate, J. Geophys. Res., 89, 7719-7735, 1984.

Carr, M. J., W. I. Rose, Jr., and R. E. Stoiber, Regional distribution and character of active andesitic volcanism: Central America, in Andesites: Orogenic Andesites and Related rocks, edited by R. S. Thorpe, John Wiley, New York, 1982, pp. 149-166.

Chael, E. P., and G. S. Stewart, Recent large earthquakes along the Middle America Trench and their implications for the subduction process, J. Geophys. Res., 87, 329-338, 1982.

Chase, T. F., H. W. Menard, and J. Mammerickx, Bathymetry of the North Pacific, Mercator projection, Tech. Rep. Ser. TR-1-TR15, Scripps Inst. of Oceanogr. and Inst. of Mar. Resour., La Jolla, Calif., 1970.

Chung, W. Y., A seismological investigation of the subduction mechanism of aseismic ridges, part II, Ph.D. thesis, Calif. Inst. of Technol., Pasadena, 1979.

Chung, W. Y., and H. Kanamori, Subduction process of a fracture zone and aseismic ridges -- The focal mechanism and source characteristics of the New Hebrides earthquake of 1969 January 19 and some related events, Geophys. J. R. Astron. Soc., 54, 221-240, 1978a.

Chung, W. Y., and H. Kanamori, A mechanical model for plate deformation associated with aseismic ridge subduction in the New Hebrides arc, Tectonophysics, 50, 29-40, 1978b.

Cochran, J., Gravity and magnetic investigations of the Guiana basin, western equatorial Atlantic, Geol. Soc. Am. Bull., 84, 3249-3268, 1973.

Couch, R., and S. Woodcock, Gravity and structure of the continental margins of southwestern Mexico and northwestern Guatemala, J. Geophys. Res., 86, 1829-1840, 1981.

Cruz, G., and M. Wyss, Large earthquakes, mean sea level, and tsunamis along the Pacific coast of Mexico and Central America, Bull. Seismol. Soc. Am., 73, 553-570, 1983.

Dean, B. W., Focal mechanism solutions and tectonics of the Middle America arc, M.A. thesis, Dartmouth Coll., Hanover, N.H., 1976.

Dean, B. W., and C. L. Drake, Focal mechanism solutions and tectonics of the Middle America arc, J. Geol., 86, 111-128, 1978.

Detrick, R., and G. Purdy, The crustal structure of the Kane fracture zone from seismic refraction studies, J. Geophys. Res., 85, 3759-3777, 1980.

Detrick, R. S., and A. B. Watts, An analysis of isostacy in the world's oceans, 3, Aseismic ridges, J. Geophys. Res., 84, 3673-3653, 1979.

Eissler, H., and K. McNally, Seismicity and tectonics of the Rivera Plate and implications for the 1932 Jalisco, Mexico earthquake, J. Geophys. Res., 89, 4520-4530, 1984.

Engel, C. G., and R. L. Fisher, Granitic to ultramafic rock complexes of the Indian Ocean ridge system, western Indian Ocean, Geol. Soc. Amer. Bull., 86, 1553-1578, 1975.

Fujita, K., and H. Kanamori, Double seismic zones and stresses of intermediate depth earthquakes, Geophys. J. R. Astron. Soc., 66, 131-156, 1981.

Geller, R. J., Scaling relations for earthquake source parameters and magnitudes, Bull. Seismol. Soc. Am., 46, 1501-1523, 1976.

Gonzalez-Ruis, J. R., Earthquake source mechanics and tectonophysics of the Middle America subduction zone in Mexico, Ph.D. thesis, U. of Calif., Santa Cruz, 1986.

Handschumacher, D. W., Post-Eocene plate tectonics of the eastern Pacific, in The Geophysics of the Pacific Ocean Basin and Its Margin, Geophys. Monogr. Ser., vol. 19, edited by G. H. Sutton, AGU, Washington, D. C., 1976, pp. 177-202.

Hasegawa, A., N. Umino, and A. Takagi, Double-planed deep seismic zone and upper-mantle structure in the northeastern Japan arc, Geophys. J. R. Astron. Soc., 54, 281-296, 1978.

Havskov, J., S. Singh, E. Nava, T. Dominguez, and M. Rodriguez, Playa Azul, Michoacan, Mexico earthquake of 25 October 1981 (M_s = 7.3), Bull. Seismol. Soc. Am., 73, 449-457, 1983.

Isacks, B., and P. Molnar, Distribution of stresses in the descending lithosphere from a global survey of focal mechanism solutions of mantle earthquakes, Rev. Geophys. Space Phys., 9, 103-174, 1971.

Kanamori, H., Seismic and aseismic slip along subduction zones and their tectonic implications, in Island Arcs, Deep Sea Trenches and Back-Arc Basins, Maurice Ewing Ser., vol. 1, edited by M. Talwani and W. C. Pitman III, AGU, Washington, D.C., 1977, pp. 162-174.

Kanamori, H., and D. L. Anderson, Theoretical basis of some empirical relations in seismology, Bull. Seismol. Soc. Am., 65, 1073-1095, 1975.

Kanamaori, H., and J. W. Given, Use of long-period surface waves for rapid determination of earthquake-source parameters, Phys. Earth Planet. Inter., 27, 8-31, 1981.

Karig, D. E., r. K. Cardwell, G. F. Moore, and D. G. Moore, Late Cenozoic subduction and continental-margin truncation along the northern Middle America Trench, Geol. Soc. Am. Bull, 89, 265-276, 1978.

Kelleher, J., and W. McCann, Buoyant zones, great earthquakes, and unstable boundaries of subduction, J. Geophys. Res., 81, 4885-4896, 1976.

Kelleher, J., L. Sykes, and J. Oliver, Possible criteria for predicting earthquake locations and their application to major plate boundaries of the Pacific and the Caribbean, J. Geophys. Res., 78, 2547-2585, 1973.

Klitgord, K. D. and J. Mammerickx, Northern East Pacific Rise: magnetic anomaly and bathymetric framework, J. Geophys. Res., 87, 6725-6750, 1982.

Lay, T., and H. Kanamori, An asperity model of large earthquake sequences, in Earthquake Prediction, An International Review, Maurice Ewing Ser., vol. 4, edited by D. W. Simpson and G. Richards, AGU, Washington, D. C., 1981, pp. 579-592.

Lynn, W. S., and B. T. R. Lewis, Tectonic evolution of the northern Cocos plate, Geology, 4, 718-722, 1976.

Macdonald, K., K. Kastens, F. N. Spiess, and S. P. Miller, Deep tow studies of the Tamayo transform fault, Mar. Geophys. Res., 4, 37-70, 1979.

Malgrange, M., and R. Madariaga, Complex distribution of large thrust and normal earthquakes in the Chilean subduction zone, Geophys. J. R. Astron. Soc., 73, 489-505, 1983.

Mammerickx, J., and K. D. Klitgord, Northern East Pacific Rise: Evolution from 25 m.y. B.P. to the present, J. Geophys. Res., 87, 6751-6759, 1982.

McNally, K. C., and J. B. Minster, Nonuniform seismic slip rates along the Middle America Trench, J. Geophys. Res., 86, 4949-4959, 1981.

Minster, J. B., and T. H. Jordan, Present-day plate motions, J. Geophys. Res., 83, 5331-5334, 1978.

Molnar, P., and L. R. Sykes, Tectonics of the Caribbean and Middle America regions from focal mechanisms and seismicity, Geol. Soc. Am. Bull., 80, 1639-1684, 1969.

Moore, J. C., J. S. Watkins, T. H. Shipley, S. B. Bachman, F. W. Beghtel, et al., Progressive accretion in the Middle America Trench, southern Mexico, Nature, 281, 638-642, 1979.

Mota, R., Contribution a l'étude sismo-tectonique du Mexique meridional, thesis, Univ. Paris VII, Paris, 1979.

Nakanishi, I., and H. Kanamori, Effects of lateral heterogeneity and source process time on the linear moment tensor inversion of long period Rayleigh waves, Bull. Seismol. Soc. Am., 72, 2063-2080, 1982.

Nixon, G. T., The relationship between Quaternary volcanism in central Mexico and the seismicity and structure of subducted ocean lithosphere, Geol. Soc. Am. Bull., 93, 514-523, 1982.

Pilger, R. H., Plate reconstructions, aseismic ridges and low angle subduction beneath the Andes, Geol. Soc. Am. Bull., 92, 448-456, 1981.

Richter, F., Focal mechanisms and seismic energy release of deep and intermediate earthquakes in the Tonga-Kermadec region and their bearing on the depth extent of mantle flow, J. Geophys. Res., 84, 6783-6795, 1979.

Robb, J. M., and M. F. Kane, Structure of the Vema fracture zone from gravity and magnetic intensity profiles, J. Geophys. Res., 80, 4441-4445, 1975.

Robin, C., regional distribution and character of active andesitic volcanism: Mexico, in Andesites: Orogenic Andesites and Related Rocks, edited by R. S. Thorpe, John Wiley, New York, 1982, pp. 137-148.

Ross, D. A., and G. G. Shor, Reflection profiles across the Middle America Trench, Geol. Soc. Am. Bull., 75, 5551-5572, 1965.

Ruff, L., and H. Kanamori, Seismicity and the subduction process, Phys. Earth Planet. Inter., 23, 240-252, 1980.

Ruff, L., and H. Kanamori, Seismic coupling and uncoupling at subduction zones, Tectonophysics, 99, 99-117, 1983.

Schilt, F. S., D. E. Karig, and M. Truchan, Kinematic evolution of the northern Cocos plate, J. Geophys. Res., 87, 2958-2968, 1982.

Sclater, J. G., R. N. Anderson, and M. L.Bell, Elevation of ridges and evolution of the central eastern Pacific, J. Geophys. Res., 76, 7888-7915, 1971.

Sclater, J. G., H. Dick, I. O. Norton, and D. Woodroffe, Tectonic structure and petrology of the Antarctic plate boundary near the Bouvet triple junction, Earth Planet. Sci. Lett., 37, 393-400, 1978.

Shor, G. G., and R. L. Fisher, Middle America Trench: Seismic refractions studies, Geol. Soc. Am. Bull., 72, 721-730, 1961.

Singh, S. K., L. Astiz, and J. Havskov, Seismic gaps and recurrence periods of large earthquakes along the Mexican subduction zone: A reexamination, Bull. Seismol. Soc. Am., 71, 827-843, 1981.

Stauder, W., Mechanism and spatial distribution of Chilean earthquakes with relation to subduction of the oceanic plate, J. Geophys. Res., 78, 5033-5061, 1973.

Stauder, W. Subduction of the Nazca plate under Peru as evidence by focal mechanisms and by seismicity, J. Geophys. Res., 80, 1053-1064, 1975.

Stein, S., J. F. Engeln, and D. W. Wiens, Subduction seismicity and tectonics in the Lesser Antilles arc, J. Geophys. Res., 87, 8642-8664, 1982.

Stewart, G. S., E. P. Chael, and K. C. McNally, The November 29, 1978, Oaxaca, Mexico, earthquake: A large simple event, J. Geophys. Res., 86, 5053-5060, 1981.

Sykes, L. R., W. R. McCann, and A. L. Kafka, Motion of the Caribbean plate during the last 7 million years and implications for earlier Cenozoic movements, J. Geophys. Res., 87, 10656-10676, 1982.

Uyeda, S., Subduction zones: An introduction to comparative subductology, Tectonophysics, 81, 133-159, 1982.

Vassiliou, M. S., The energy release in earthquakes, and subduction zone seismicity and stress in slabs, Ph.d. thesis, Calif. Inst. of Technol., Pasadena, 1983.

Vogt, P.R., A. Lowrie, D. Bracey, and R. Hey, Subduction of aseismic oceanic ridges: Effects on shape, seismicity, and other characteristics of consuming plate boundaries, Geol. Soc. Am. Spec. Pap., 172, 1976.

von Huene, R., J. Aubouin, J. Azema, G. Blackinton, J. A. Carter, et al., Leg 67: DSDP Mid-America Trench transect off Guatemala, Geol. Soc. Am. Bull., 91, 421-432, 1980.

Appendix

These tables list all focal mechanism parameters for events used in this study. These events are shown in map view in Figure 1.4, and projected on cross sections in Figures 1.5, 1.6, and 1.7. P and T axes are shown in Figure 1.14. The first part of the event number refers to the cross section containing that event. Catalog locations and depths are given here, although some of these events have been relocated in other studies. Dip direction of nodal plane is always clockwise from azimuth. Type of motion: T = thrust, N = normal, SS = strike-slip. (T) and (N) indicate events for which the focal mechanism can be interpreted either as movement on a 0^{o} or 90^{o} dipping plane. References: MS = Molnar and Sykes (1969), M = Mota (1979), CS = Chael and Stewart (1982), G1 or G2 = Gonzales-Ruis (1986), * = this study. Numbers given with references refer to that author's numbering system.

NUM-BER	DATE	LAT N	LONG W	d	m_b	M_s	NODAL PLANE 1 str	dip	NODAL PLANE 2 str	dip	P AXIS az	pl	T AXIS az	pl	TYPE OF MO-TION	REF
1A	30 JAN 73	18.481	102.996	43	6.2	7.5	266	17	122	76	204	31	46	57	T	CS
1B	10 FEB 73	18.886	103.545	33	5.4	5.6	246	16	118	80	197	32	40	54	T	D2
1C	26 APR 68	18.700	103.300	65	5.5		297	21	119	70	204	25	42	64	T	D3
1D	14 AUG 68	18.538	102.824	72	5.4		54	50	318	84	268	32	13	22	SS	D55
1E	27 FEB 66	18.900	102.600	93	5.8		6	57	165	35	310	75	88	11	N	*
1F	29 JUL 73	19.577	103.519	130	5.1		310	25	130	65	220	20	40	70	T	*
2A	25 OCT 81	18.048	102.084	33	6.2	7.3	278	12	121	79	207	34	37	56	T	*
2B	15 NOV 75	18.225	102.185	33	5.9	5.9	247	69	156	85	203	11	110	18	SS	*
2C	11 APR 66	18.300	102.300	56	5.5		294	26	129	63	213	19	53	70	T	MS129
2D	29 SEP 78	18.615	102.262	96	5.5		323	40	143	50	53	85	233	5	N	*
2E	5 SEP 76	18.742	101.118	86	5.3		300	67	120	23	210	68	30	22	N	*
2F	3 JUL 73	19.104	101.833	125	5.6		291	82	111	8	201	53	21	37	N	*
3A	14 MAR 79	17.813	101.276	49	6.5	7.6	293	14	116	76	205	31	28	59	T	CS
3B	19 SEP 76	18.221	100.469	55	5.6		292	50	112	40	202	85	22	5	N	*
3C	25 SEP 66	18.300	100.800	79	5.5		275	56	64	38	231	72	352	10	N	MS146
3D	6 JUL 64	18.300	100.400	100	6.3		302	50	87	46	280	72	15	2	N	MS147
3E	27 OCT 71	18.348	100.305	72	5.1		326	60	146	30	236	75	56	15	N	M66
3F	7 JUL 71	18.392	100.249	88	4.2		294	72	114	18	204	63	24	27	N	M50
4A	14 SEP 72	16.804	100.219	54	4.6		304	0	124	90	214	45	34	45	(T)	M118
4B	11 APR 73	16.912	100.262	33	4.9		300	0	120	90	210	45	30	45	(T)	M130
4C	16 JUL 73	17.323	100.679	44	5.6	5.7	303	10	123	80	213	35	33	55	T	*
4D	9 DEC 65	17.300	100.000	54	6.0		314	14	134	76	224	31	44	59	T	MS130
4E	14 APR 67	17.565	100.235	60	5.1		4	45	160	48	358	78	262	1	N	*
4F	2 JUL 68	17.638	100.273	41	5.9		328	21	130	71	28	64	226	26	N	D29
4G	5 JUL 78	18.487	100.007	62	5.6		325	50	145	40	235	85	55	5	N	*
4H	1 FEB 76	17.172	100.189	52	5.7	5.6	270	52	90	38	0	7	180	83	T	G2

NUM-BER	DATE	LAT N	LONG W	d	m_b	M_s	NODAL PLANE 1 str	dip	NODAL PLANE 2 str	dip	P AXIS az	pl	T AXIS az	pl	TYPE OF MO-TION	REF
4G	5 JUL 78	18.487	100.007	62	5.6		325	50	145	40	235	85	55	5	N	*
5A	4 FEB 70	15.532	99.484	21	6.0	6.5	21	80	113	80	337	14	67	0	SS	D57
5B	9 DEC 70	16.150	99.410	34	5.5	5.4	304	78	124	12	214	57	34	33	N	D30
5C	3 FEB 68	16.700	99.400	9	5.7		358	68	92	80	224	8	317	23	SS	D52
5D	11 MAY 62	17.000	99.600	40			303	20	123	70	213	25	33	65	T	MS131
5E	5 SEP 71	17.087	99.811	50	5.2	5.0	278	0	98	90	188	45	8	45	(T)	M55
5F	21 MAY 73	16.895	99.292	96	4.8		11	30	101	90	216	38	334	38	T-SS	M132
5G	10 OCT 71	17.088	99.317	67	4.9		296	0	116	90	206	45	26	45	(T)	M61
5H	19 MAY 62	17.200	99.500	33			303	20	126	70	213	25	36	65	T	MS132
5I	21 SEP 71	16.811	98.609	41	4.7		282	20	102	70	192	25	12	65	T	M58
5J	18 JUL 74	17.064	98.351	48	5.6	5.2	243	64	336	85	106	15	202	22	SS	*
5K	3 MAR 71	17.656	99.289	77	5.1		298	56	118	34	208	79	28	11	N	M32
5L	24 OCT 80	18.211	98.240	72	6.4	7.0	310	22	114	69	14	66	208	24	N	G 1
5M	23 APR 75	16.447	98.91	11	6.0	6.2	284	16	104	74	194	29	14	61	T	G 2
5N	19 MAR 78	17.026	99.735	36	5.8	6.4	302	16	122	74	212	29	32	61	T	G 2
6A	1 JUL 72	15.868	98.387	33	4.9		302	20	122	70	212	25	32	65	T	M107
6B	1 DEC 71	15.923	98.001	38	4.7		28	30	118	90	234	38	2	38	T-SS	M71
6C	2 JAN 72	16.153	98.362	54	5.4		328	15	128	75	222	30	30	58	T	M74
6D	3 APR 65	16.000	97.900	16	5.5		310	10	130	80	220	35	40	55	T	MS133
6E	3 JAN 72	16.232	98.216	24	5.0		313	45	133	45	223	90	43	0	N	M76
6F	2 JUL 72	16.362	98.523	53	4.9		302	25	122	65	32	70	212	20	N	M108
6G	28 MAR 71	16.342	98.361	44	4.7		304	0	124	90	214	45	34	45	(T)	M35
6H	1 JUL 72	16.512	98.463	46	4.6		304	20	124	70	214	25	34	65	T	M106
6I	3 JAN 72	16.213	98.121	58	4.4		328	30	109	66	212	18	349	64	T	M75
6J	13 NOV 72	16.604	97.980	33	4.7		38	30	128	90	244	38	9	38	T-SS	M123
6K	4 MAR 72	16.482	97.753	58	5.0		9	30	117	80	229	28	357	48	T-SS	M85

NUM-BER	DATE	LAT N	LONG W	d	m_b	M_s	NODAL PLANE 1 str	dip	NODAL PLANE 2 str	dip	P AXIS az	pl	T AXIS az	pl	TYPE OF MO-TION	REF
6L	2 APR 66	16.400	97.400	53	5.3		285	60	61	40	356	11	243	64	T	MS145
6M	2 AUG 68	16.588	97.696	40	6.3	7.1	287	12	122	78	209	34	35	56	T	CS
6N	16 AUG 68	16.749	97.691	46	5.4	5.0	284	8	104	82	194	37	14	53	T	D4
6O	22 JAN 72	16.807	97.696	112	4.4		308	40	128	50	218	5	38	85	T	M79
6P	28 AUG 73	18.267	96.598	84	6.8	6.8	326	50	123	42	297	78	45	4	N	G1
6Q	11 MAR 67	19.120	95.822	47	5.3		243	38	153	90	211	34	94	34	T-SS	MS137
7A	8 MAY 71	15.659	96.609	33	4.7		332	40	82	75	199	20	307	48	T-SS	M41
7B	3 AUG 72	15.807	96.404	33	4.6		318	70	138	20	48	25	228	65	T	M111
7C	29 NOV 78	16.010	96.591	18	6.4	7.7	270	14	127	79	210	34	47	55	T	CS
7D	8 JUL 72	16.295	96.891	62	5.6		120	75	300	15	30	60	210	30	N	M110
7E	13 FEB 72	16.200	96.445	26	4.7		156	90	336	0	66	45	246	45	(N)	M83
7F	24 AUG 65	16.100	96.200	36	5.5		293	10	129	80	216	35	43	55	T	MS136
7G	9 JUN 72	16.372	96.917	141	4.5		37	30	126	90	240	38	10	38	T-SS	M100
7H	16 JUL 71	16.721	96.080	14	5.2		304	78	64	24	18	30	236	54	T	M51
7I	5 MAY 70	17.863	95.689	94	4.6		312	61	146	30	202	72	47	15	N	M14
8A	16 SEP 72	15.244	96.229	33	6.0	5.7	311	60	100	34	257	70	29	12	N	D31
8B	10 NOV 72	15.692	95.762	37	5.4	5.6	291	22	104	68	196	22	9	67	T	D6
8C	24 AUG 65	16.000	96.200	10	5.5		293	10	129	80	216	35	43	55	T	MS135
8D	23 AUG 65	16.300	95.800	20	6.9		268	14	124	79	207	34	44	55	T	CS
8E	4 AUG 80	16.258	95.706	33	5.1	4.9	290	5	110	85	200	40	20	50	T	*
8F	24 MAY 71	16.211	95.535	71	4.3		40	30	130	90	14	38	247	38	N-SS	M45
8G	19 MAR 71	17.104	95.130	83	5.5		318	34	106	60	339	69	208	14	N	M33
8H	20 OCT 69	17.304	95.188	87	5.4		332	70	152	20	242	65	62	25	N	D35
8I	9 AUG 72	17.075	94.841	124	5.0		342	34	133	60	5	70	234	13	N	M114

NUM-BER	DATE	LAT N	LONG W	d	m_b	M_s	NODAL PLANE 1 str	dip	NODAL PLANE 2 str	dip	P AXIS az	pl	T AXIS az	pl	TYPE OF MO-TION	REF
8J	25 DEC 70	17.488	95.062	117	4.7		260	60	144	54	116	51	21	4	N-SS	M23
8K	3 OCT 71	18.086	94.142	38	5.0		273	12	127	80	211	34	44	54	T	M60
9A	27 AUG 70	15.409	95.600	31	5.5	5.7	316	71	136	19	226	64	46	26	N	D32
9B	25 JUN 74	15.444	95.468	30	5.6	5.0	304	10	113	80	205	35	21	55	T	D7
9C	13 NOV 72	15.575	94.984	33	5.5	6.5	0	8	117	86	214	40	18	48	T	D8
9D	28 NOV 68	15.370	94.590	33	5.2	6.4	322	9	109	82	212	36	26	53	T	D9
9E	23 JAN 66	16.000	95.000	43	4.6		325	73	207	33	200	53	77	23	N-SS	*
9F	24 JAN 83	16.147	95.232	57	6.3	6.7	336	80	156	10	246	55	66	35	N	*
9G	29 JAN 72	16.215	94.974	33	4.5		297	0	117	90	207	45	27	45	(T)	M82
9H	4 JUN 72	15.725	94.452	81	4.6		304	0	124	90	214	45	34	45	(T)	M97
9I	19 AUG 75	16.224	94.129	85	5.8		320	80	140	10	230	55	50	35	N	*
9J	11 DEC 71	16.446	94.091	95	5.0		284	31	122	60	54	73	205	14	N	M72
9K	22 JUN 79	17.000	94.609	107	6.3		329	82	227	35	206	43	86	28	N-SS	*
9L	2 FEB 65	17.200	94.500	140	5.3		302	40	122	50	32	85	212	5	N	*
9M	20 DEC 72	16.826	93.887	150	4.6		276	42	73	50	173	4	282	78	T	M127
9N	10 DEC 72	17.463	93.609	211	5.2		307	40	127	50	37	85	213	5	N	*
10A	8 MAR 72	14.440	93.980	33	4.9		289	0	109	90	199	45	19	45	(T)	M89
10B	8 MAR 72	14.557	93.914	33	4.9		303	0	123	90	213	45	33	45	(T)	M90
10C	8 MAR 72	14.600	93.651	33	4.5		305	0	125	90	215	45	35	45	(T)	M88
10D	2 MAY 70	14.719	93.706	32	5.4	5.5	306	6	126	84	216	39	36	51	T	M12
10E	4 SEP 73	14.984	94.301	51	5.2		295	10	115	80	205	35	25	55	T	D10
10F	7 MAR 72	14.631	93.803	33	4.8	5.0	305	50	125	40	35	5	215	85	T	M87
10G	22 SEP 71	15.055	93.700	33	5.2	5.6	269	16	115	76	199	30	34	58	T	D11
10H	31 OCT 71	15.265	93.904	90	4.7		204	30	114	90	177	38	50	38	T-SS	M67

NUM-BER	DATE	LAT N	LONG W	d	m_b	M_s	NODAL PLANE 1 str	dip	NODAL PLANE 2 str	dip	P AXIS az	pl	T AXIS az	pl	TYPE OF MO-TION	REF
10I	7 MAY 71	15.683	94.342	83	4.6		290	0	110	90	200	45	20	45	(T)	M40
10J	22 APR 62	15.500	93.100	69			326	90	146	0	236	45	56	45	(N)	MS138
10K	4 JUN 79	15.684	93.596	80	5.7		305	68	56	50	262	46	4	11	N-SS	*
10L	23 DEC 70	15.900	93.817	90	5.3		330	84	122	6	242	50	58	39	N	M21
10M	23 JAN 72	15.813	93.381	87	4.6		301	20	121	70	211	25	31	65	T	M81
10N	14 MAY 71	16.249	93.977	95	4.8		234	30	126	80	193	28	66	48	T-SS	M42
10O	24 DEC 70	16.102	93.564	116	5.6		343	84	163	6	253	51	73	39	N	D37
10P	11 AUG 72	16.180	93.491	98	4.5		293	90	113	0	203	45	23	45	(N)	M115
10Q	4 MAY 72	15.990	93.083	115	5.1		321	30	141	60	231	15	51	75	T	M95
10R	23 MAY 71	16.264	92.861	130	4.7		131	0	311	90	221	45	41	45	(N)	M44
10S	3 FEB 68	16.600	93.500	142	5.5		302	15	122	75	210	20	30	60	T	D36
10T	3 MAY 71	16.536	93.495	149	4.3		322	25	103	70	204	24	349	62	T	M39
10U	14 MAR 75	16.598	93.385	155	5.5		350	74	224	26	233	56	96	26	N-SS	*
11A	30 JUN 72	14.048	93.285	33	5.0	3.7	306	90	36	30	244	38	10	38	T-SS	M104
11B	30 APR 70	14.476	93.498	22	5.4	5.6	318	10	138	80	228	35	48	55	T	M8
11C	30 APR 70	14.447	93.430	24	5.3	5.6	287	20	120	70	207	22	38	65	T	D13
11D	1 MAY 70	14.611	93.554	35	5.1		292	24	112	66	202	21	22	69	T	M9
11E	15 DEC 70	14.347	93.133	33	5.2		284	22	131	70	213	24	58	63	T	M19
11F	15 DEC 70	14.456	93.075	33	4.8		20	10	110	90	10	44	209	44	N	M20
11G	29 APR 70	14.671	93.499	29	5.2		302	0	122	90	212	45	32	45	(T)	M3
11H	1 MAY 70	14.621	93.612	38	5.0	5.4	306	2	126	88	216	43	36	47	(T)	M11
11I	1 MAY 70	14.614	93.586	49	5.0		309	2	129	88	219	43	39	47	(T)	M10
11J	6 SEP 71	13.921	92.540	60	5.1		264	43	130	57	198	7	94	65	T	D21
11K	7 JUN 72	14.490	93.078	54	4.6		312	0	132	90	222	45	42	45	(T)	M99

NUMBER	DATE	LAT N	LONG W	d	m_b	M_s	NODAL PLANE 1 str	NODAL PLANE 1 dip	NODAL PLANE 2 str	NODAL PLANE 2 dip	P AXIS az	P AXIS pl	T AXIS az	T AXIS pl	TYPE OF MOTION	REF
11L	1 MAY 70	14.635	93.158	44	5.4		302	30	102	62	198	16	349	72	T	D15
11M	30 APR 70	14.698	93.192	19	5.6	6.4	354	22	123	76	227	30	13	55	T	D14
11N	15 MAY 70	14.512	92.811	33	5.4	5.5	282	30	105	60	193	15	20	76	T	D16
11O	30 JUN 72	14.542	92.903	33	4.9	4.1	212	30	122	90	59	38	185	38	N-SS	M105
11P	29 APR 70	14.518	92.603	33	5.8	7.3	296	20	116	70	206	25	26	65	T	CS
11Q	29 APR 70	14.618	92.690	41	5.6	6.3	306	12	126	78	216	33	36	57	T	M1
11R	13 MAY 63	14.600	92.900	61	5.6		3	18	131	80	232	33	24	54	T	MS139
11S	22 JAN 70	14.341	92.406	58	5.5		241	28	132	80	200	30	70	48	T-SS	D20
11T	21 NOV 73	14.504	92.728	59	5.3		338	68	71	82	203	8	296	22	SS	D58
11U	26 JAN 67	14.906	92.965	57	5.4		348	28	118	68	358	60	224	22	N	MS148
11V	18 FEB 71	14.488	92.181	79	4.9		302	0	122	90	212	45	32	45	(T)	M28
11W	23 MAY 70	14.912	92.227	109	4.9		300	62	157	33	170	68	44	15	N	M16
11X	1 MAR 65	15.400	92.500	93	5.9		313	86	211	20	204	46	60	39	N	MS141
11Y	24 JUL 62	15.400	92.500	131			321	90	141	0	231	45	51	45	(N)	MS140
11Z	25 SEP 68	15.571	92.638	138	5.7		302	4	122	86	212	31	32	49	T	D38
11AA	24 DEC 71	15.514	92.123	182	4.4		304	90	124	0	214	45	34	45	(N)	M73
11BB	21 JAN 68	16.800	92.300	77	5.4		18	90	198	0	288	45	108	45	(T)	D67
12A	9 APR 70	13.212	92.259	41	5.3	5.0	272	10	107	80	194	19	19	56	T	D22
12B	20 AUG 71	13.376	92.372	33	5.8	5.6	66	75	330	70	197	2	288	26	SS	D60
12C	25 MAY 71	14.063	92.127	45	4.9		123	90	303	0	33	45	213	45	(T)	M46
12D	24 MAR 71	14.125	92.279	64	5.0		306	0	126	90	216	45	36	45	(T)	M34
12E	22 AUG 71	13.759	91.404	69	4.8		334	40	140	51	228	6	4	81	T	M54
12F	27 JUN 72	13.981	91.754	74	5.1		206	40	116	90	173	32	58	32	SS	M103
12G	7 JUN 73	14.277	92.008	78	5.5		300	50	120	40	30	5	210	85	T	M135

NUM-BER	DATE	LAT N	LONG W	d	m_b	M_s	NODAL PLANE 1 str	dip	NODAL PLANE 2 str	dip	P AXIS az	pl	T AXIS az	pl	TYPE OF MO-TION	REF
12H	9 JUN 73	14.070	91.852	76	4.7		303	40	123	50	213	5	33	85	T	M137
12I	10 DEC 66	14.300	92.000	60	5.6		319	32	143	60	231	14	55	76	T	MS142
12J	19 FEB 71	14.151	91.672	68	5.0		288	25	129	66	212	20	55	67	T	M29
12K	7 NOV 71	14.216	91.857	86	5.0		286	64	106	26	16	19	196	71	T	M68
12L	19 MAY 71	14.311	91.982	86	4.7		308	0	128	90	218	45	38	45	(T)	M43
12M	7 JUN 73	14.386	91.951	97	5.1		303	40	123	50	213	5	33	85	T	M136
12N	21 APR 69	14.098	91.015	82	5.5		332	50	112	48	310	68	42	1	N	D33
12O	22 JAN 72	14.029	91.014	102	5.5		320	74	140	16	230	61	50	29	N	D41
12P	28 JUN 71	14.445	91.611	97	5.0		346	82	166	8	257	53	77	37	N	M49
12Q	18 AUG 66	14.600	91.700	85	5.6		305	20	125	70	215	25	35	65	T	MS143
12R	3 FEB 71	14.382	91.388	95	4.9		288	66	108	24	18	21	198	69	T	M24
12S	22 FEB 73	14.478	91.637	107	5.2		327	2	147	88	237	43	57	47	T	M129
12T	10 APR 74	14.533	91.627	108	5.4		313	76	137	14	222	59	45	31	N	D40
12U	15 DEC 64	14.700	91.700	118	5.4		130	90	310	0	220	45	40	45	(N)	MS169
12V	24 MAY 73	14.710	91.234	100	5.2		297	15	106	75	198	30	11	60	T	M133
12W	24 FEB 63	14.700	91.300	119	5.6		326	10	146	80	236	35	56	55	T	MS144
12X	28 MAY 71	14.834	91.405	124	5.4		188	30	286	86	168	42	41	34	T-SS	M48
12Y	17 NOV 72	15.614	91.462	222	5.2		114	90	24	20	5	42	222	42	N-SS	M124
12Z	22 OCT 71	15.780	91.239	20	4.5	3.6	224	13	314	90	209	43	57	43	T	M65
12AA	12 OCT 71	15.844	91.172	36	5.7	5.7	192	80	284	86	58	5	148	10	SS	D59
12BB	18 OCT 71	15.941	91.138	36	4.7		274	20	52	75	152	28	304	58	T	M64
12CC	15 JAN 72	15.958	90.988	33	4.7		296	62	95	30	19	16	232	72	T	M77
13A	5 JUN 72	13.356	90.278	33	4.7		304	0	124	90	214	45	34	45	(T)	M98
13B	11 JUN 72	13.463	90.584	52	5.1		325	20	145	70	235	25	55	65	T	M101

NUM-BER	DATE	LAT N	LONG W	d	m_b	M_s	NODAL PLANE 1 str	dip	NODAL PLANE 2 str	dip	P AXIS az	pl	T AXIS az	pl	TYPE OF MO-TION	REF
13C	27 OCT 79	13.833	90.881	58	5.7	6.8	281	28	144	69	220	22	82	62	T	*
13D	27 OCT 79	13.778	90.730	65	5.6	6.6	281	28	144	69	220	22	82	62	T	*
13E	30 JUN 73	13.763	90.935	78	5.1		299	40	119	50	209	5	29	85	T	M138
13F	11 JUN 72	13.511	90.521	79	4.4		200	40	110	90	168	32	52	32	SS	M102
13G	6 AUG 72	13.478	90.590	83	4.6		300	0	120	90	210	45	30	45	(T)	M112
13H	28 MAY 71	13.049	89.963	86	4.3		284	78	128	13	186	56	18	32	N	M47
13I	9 APR 72	13.528	90.464	85	4.8		308	0	128	90	218	45	38	45	(T)	M92
13J	11 MAR 72	13.368	90.042	85	5.1		318	2	138	88	229	43	49	47	T	D43
13K	5 OCT 72	13.839	91.073	89	5.4		282	50	102	40	12	5	192	85	T	M120
13L	16 NOV 71	13.412	90.729	115	4.6		252	15	120	80	43	54	200	34	N	M69
13M	22 JAN 72	13.896	91.073	106	4.5		294	80	114	10	204	55	24	35	N	M80
13N	18 SEP 71	13.526	90.026	82	4.8		300	30	120	60	210	15	30	75	T	M57
13O	20 APR 73	13.482	90.028	88	4.8		306	40	126	50	216	5	38	85	T	M131
13P	31 MAY 73	13.941	90.877	99	5.4		310	0	130	90	220	45	40	45	(T)	M134
13Q	19 APR 71	13.907	90.540	92	5.0		319	53	154	38	55	6	187	80	T	M37
13R	21 AUG 72	13.957	90.816	119	4.8		300	0	120	90	210	45	30	45	(T)	M116
13S	5 JUL 72	13.951	90.526	109	4.8		207	10	117	90	37	44	197	44	N-SS	M109
13T	14 APR 71	14.125	90.133	124	4.8		298	10	119	80	207	34	27	54	T	M36
13U	23 NOV 71	14.412	90.171	190	4.6		297	90	117	0	207	45	27	45	(N)	M70

Part II:

Lithosphere and Upper Mantle Structure of the Canadian Shield and Eastern North America

Abstract

In Chapter 2, waveform modeling of the phases P_{nl}, P, and PP is used to determine the P-wave upper-mantle structure beneath the Canadian shield. Long-period recordings at WWSSN, LRSM, and Canadian network stations in North America are used, with earthquakes within and just outside the shield as sources. The P dataset is incomplete because of the scarcity of large events within the shield, and the inclusion of PP provides much more data. Using the WKBJ approach to calculate the mantle response, the PP waveforms can be modeled almost as well as the P. The phase P_{nl} persists to large distances in shield regions, and the interference of P_{nl} with triplication-range P helps constrain the structure in the upper 400 km. Important features of our model, which is designated S25, are: 1) a thick, high-Q, high-velocity lid to 165 km; 2) a deep low-velocity zone; and 3) discontinuities of 5% at 405 km and 4% at 660 km. The lid and low-velocity zone create an unusual B-branch arrival, not seen in other regions, which persists well beyond 30°. Only slight lateral variation is noted within the shield region. The major features of the model are similar to those of Grand and Helmberger's (1984) S wave model for the Canadian shield.

Chapter 3 looks in more detail at recordings of P_{nl} in eastern North America. P_{nl} recordings of earthquakes in the magnitude range $5.0 \leq m_b \leq 6.0$ are particularly important. These earthquakes often do not produce good teleseismic recordings; however, they are tectonically important events, especially in eastern North America, where they are

often the largest instrumentally recorded earthquake in a given region. Seismic moments are determined for four North American intraplate events by modeling of P_{nl}, and compared with moments determined by other methods. The earthquakes discussed are: 1) the Baffin Bay earthquake of 4 September 1963, m_b=5.9, for which P_{nl} modeling gives M_o=2.2x10^{25} dyne-cm, and teleseismic body wave modeling gives 1.7x10^{25} dyne-cm; 2) the New Brunswick mainshock of 9 January 1982, m_b=5.7, for which P_{nl} modeling gives 1.3x10^{24} dyne-cm, and teleseismic body-wave modeling gives 1.6x10^{24} dyne-cm; 3) the Illinois earthquake of 9 November 1968, m_b=5.3, for which P_{nl} modeling gives M_o=1.4x10^{24} dyne-cm and surface wave spectral amplitudes give 9x10^{23}; and 4) the Sharpsburg, Kentucky earthquake of 27 July 1980, m_b=5.2, for which P_{nl} modeling gives 7.5x10^{23} dyne-cm, and surface wave spectral amplitudes give 4.1x10^{23}. This modeling of P_{nl} is done using a simple layer-over-a-halfspace model for the crust and Moho.

The effects of lid structure on P_{nl} are then investigated. For a velocity model such as S25, which has a thick lid with a positive velocity gradient, the P_{nl} waveforms may not be accurately modeled by a layer-over-a-halfspace structure, at distances as little as 800 or 900 km. P_{nl} responses are presented for four different lid structure models, two with a positive velocity gradient and two with a negative gradient. P_{nl} synthetics for the previously discussed earthquakes are recalculated using these responses. Some variation in lid structure is indicated, but the dataset is quite sparse.

Chapter 2

Upper Mantle P Velocity Structure of the Canadian Shield

Introduction

There has been much interest recently in the mapping of upper mantle velocity and its lateral variations. Many much-debated issues about mantle composition and processes may be resolved only when detailed information on velocities allows testing of various hypotheses. For example, a determination of both P and S wave structure for the same area allows calculation of properties such as Poisson's ratio, seismic parameter, and V_p/V_s ratio, which provide much information on mineralogy (Anderson and Bass, 1984). Mapping of the topography of mantle discontinuities will provide important constraints on depths of mantle convection (Hager, 1984). A related question is the depth to which continents act as coherent plate-tectonic units (Jordan, 1981; Anderson, 1979; Lerner-Lam and Jordan, 1987). This could be answered by a determination of the depth extent of velocity differences between stable shield and tectonically active regions.

The recent work on global, three-dimensional modeling of velocities within the earth provides excellent illustration of lateral variations. However, because of the limited vertical resolution of these studies, some of the above questions are not addresssed. For investigation of the upper mantle, surface wave tomography provides the best resolution, but still shows only long-wavelength features of the S wave structure. Body-wave tomography does not resolve structure well in the upper mantle, since rays are travelling vertically through this

region. In fact, much information about the uppermost mantle is removed from the inversion in the form of station and event statics. The tomographic inversion approach can be used for upper mantle structure if multiple arrivals are used (Grand, 1987), but this requires an understanding of the raypaths for these arrivals, so some previous modeling of the wave propagation in the area is necessary. For detailed information on the vertical features of the velocity structure, the best approach is a careful study of a limited, uniform area.

In this study, the P wave upper mantle structure of the Canadian shield is determined by forward waveform modeling of the phases P_{nl}, P, and PP. Propagation paths are almost entirely within the shield, and lateral heterogeneity is not considered in the modeling process. As the largest of the Precambrian shields, the Canadian shield is a good candidate for a large area of relatively homogeneous structure. It is also a particularly important area for determining the nature of continental roots. Results from global studies are ambiguous for the Canadian shield. Woodhouse and Dziewonski's (1984) surface wave inversion study shows high shear wave velocities throughout the shield, and a pronounced continental root to at least 350 km. Similar results are obtained by Grand (1987). However, studies of surface wave phase velocities by Nakanishi and Anderson (1984) and Tanimoto (1985) do not show such a consistent structure. They show high phase velocities for Love waves, but slow Rayleigh wave velocities. Regional studies of surface wave dispersion show a thick, high-velocity lithosphere beneath the shield (Brune and Dorman, 1963; Wickens, 1971). These studies look at shorter-period surface waves than do the global studies, and so are

resolving only the upper few hundred kilometers. Numerous studies of P wave structure have been done, most using refraction data (reviewed by Berry (1973) and Berry and Mair (1977)). These studies, which again resolve only crustal and uppermost mantle structure, show a thick crust underlain by high P_n velocities in the upper mantle. Patterns of P and S wave residuals in Canada have also been interpreted as indicating a thick lithosphere underlying the Canadian shield (Poupinet, 1979; Wickens and Buchbinder, 1980).

More recently, Grand and Helmberger (1984) determined S wave structure to a depth of 1000 km for the Canadian shield. They show a thick lithosphere underlain by a deep low-velocity zone, and jumps in velocity at 405 and 660 km. Their work is particularly relevant to this study, since the area covered is the same, and similar modeling techniques are used. Our starting model was created by mimicking their S wave structure for P waves, and this model was then altered as necessary.

Modeling Techniques

Forward waveform modeling is now a fairly standard technique for determining upper mantle structure from body waves (Wiggins and Helmberger, 1973; Dey-Sarkar and Wiggins, 1976; Burdick and Helmberger, 1978; Given and Helmberger, 1980; Burdick, 1981; Grand and Helmberger, 1984). Waveform modeling allows the identification of various arrivals in the seismograms with features at various depths in the velocity structure. A velocity model is then developed through trial-and-error modeling. As an understanding is gained of the effects on the seismogram of changes in the velocity model, the constraints on the

model can be determined. For this study, the phases P_{nl}, P, and PP are used. All of the synthetics are constructed using the same basic principle, which is that of convolving several linear operators to construct a seismogram. The seismogram can be expressed as

$$Y(t)=S(t)*I(t)*A(t)*M(t), \qquad (1)$$

where Y(t) is the complete seismogram, S(t) is the source, I(t) is the instrument response, A(t) is attenuation, and M(t) is the Green's function for the wave propagation. The source function S(t) depends on the depth and orientation of the earthquake and the time history of the rupture. As much as possible, we try to use events with a simple time function, so that complications in the seismogram that are due to structure are more clear. The source function is determined by modeling of teleseismic records, for which the propagation operator is just a delta function. The propagation operator M(t) is constructed differently for each phase, and each will be discussed separately. A Futterman attenuation operator is used for the attenuation (Futterman, 1962; Carpenter, 1966). The attenuation used also varies with the phase being modeled.

P_{nl} refers to the entire seismogram before the S wave time, for recordings at up to about 15^{o}. Seismograms in this distance range are complex, with a wave train made up of arrivals that have undergone multiple reflections within the crust, including mode conversions at the free surface and Moho. The initial part of the record is dominated by P headwaves (P_n), and the later part of the record includes the longer-period PL, which has more SV energy. At shorter distances the Moho velocity and depth are the primary influences on the Green's functions. At greater distances the gradient within the lid may have an effect.

The method of constructing the Green's functions is discussed in detail in Helmberger and Engen (1980) and Wallace et al. (1981). A simple layer over a half-space model is used to represent the crust and Moho. Generalized rays are summed for up to six bounces in the crust, with the multiples being added until the waveform does not change significantly with additional rays. The seismogram is then computed by convolving with the instrument response and the source-time function. Attenuation is not included in these seismograms, since its effect is small in the high-Q crust and lithosphere.

The phase P goes through triplications from the upper mantle discontinuities at distances of about 15-30^{o}. In modeling records at these distances, arrivals bottoming at a wide range of depths within the upper mantle must be included. Several techniques are available for the construction of the Green's functions. We have used both the Caignard-de Hoop method (Helmberger, 1973a) and the WKBJ approach of Chapman (1976, 1978) and Wiggins (1976). The WKBJ approach has the advantage of being faster to run and providing for easier modification of velocity structure. Most of the preliminary modeling was done using this technique. However, for certain types of arrivals, the WKBJ synthetics may not be as accurate as those computed using Caignard. For example, the amplitudes of arrivals beyond the ends of triplications may be overestimated by WKBJ. Also, since WKBJ does not model tunneled energy, arrivals that have interacted strongly with the lid and shadow zone will not be accurately predicted. These problems have been discussed thoroughly by Grand and Helmberger (1984) for SH-wave modeling, and the same problems arise for P waves. In general, the timing of various arrivals will be correct, but their relative

amplitudes may not be. For this reason, the final modeling of P is done using Caignard-de Hoop.

In the Canadian shield, a particularly interesting group of seismograms is recorded at distances of 16-20°. The seismogram is still dominated by $P_{n\underline{l}}$, but arrivals from within the mantle also appear. The relative timing of these arrivals provides a great deal of information on velocity in the upper 400 km. In modeling these records, the Caignard technique is used, and both multiple reflections within the crust and arrivals from the upper mantle are included.

All of the triplication branches cross and interfere in the distance range 20-26°. However, because of the scarcity of sources within the shield, we have almost no recordings at these distances. Far more data are made available by using the phase PP. For these records, either the source or the receiver is generally just outside the shield area. However, the size of the Canadian shield and the source-receiver geometries used allows the portion of the travel path outside the shield to be kept to a small portion of the total path, so that rays are bottoming within the shield, and any heterogeneity is having only a small effect. PP undergoes triplications at twice the distance of P, roughly 30-60°, with twice the time separation between the arrivals. In addition to the information contained in the PP waveforms, the relative timing of P and PP provides an additional constraint on the overall travel time through the model. The use of relative timing lessens errors introduced by near-source and near-receiver heterogeneity, since both P and PP have similar paths there, and the local effect will be cancelled out.

For the modeling of PP, the WKBJ technique is used. Since the

WKBJ technique requires smooth gradients, the discontinuities were treated as regions of high gradient spread over 10 km. The synthetic is constructed by computing P at half the distance, then doubling the time at each point. The phase shift of PP is accounted for by applying a Hilbert transform to the waveform (Choy and Richards, 1975). This approach has been shown to work well for waveform modeling of SS (Butler, 1979; Grand and Helmberger, 1984). The Caignard approach is not practical for the computation of PP, because of the large number of rays needed. Keeping in mind that some caution is needed in interpreting certain arrivals in the WKBJ synthetics, they are used rather than Caignard because of their ease of computation. A t* of 0.7 was used for P, and a t* of 1.4 for PP. The t* must be higher for PP, since these waves have remained in the upper mantle for their entire travel path.

The S25 Canadian Shield Velocity Model

Seven events are used in this study. Locations and source parameters are listed in Table 2.1. Sources and receivers are shown in Figure 2.1 for four events in eastern North America, and in Figure 2.2 for three events in western North America. The most data was provided by the Baffin Bay event, an unusual large event located within the shield region. The source process of this event was somewhat complex, which is not ideal for use in modeling structure. However, the location and size of this event make it extremely valuable. Extensive source modeling was done using the teleseismic records, and it was found that by using three subevents, the data are modeled quite well. The other events are all modeled using a very simple source function.

Table 2.1: Event Locations and Source Parameters

Event	Date	Location		Origin time	m_b	Source orientation* strike	dip	rake	Depth km	Source-time fcn* δt_1, δt_2, δt_3	Reference
A1	Nov 23, 1967	80.2 N	1.0 W	13 42 1.6	5.8	128°	74°	174°	10	2.0, 2.0, 2.0	Horsfield & Maton, 1970
A2	Oct 18, 1967	79.8 N	2.4 E	1 11 44.8	5.7	136°	71°	201°	10	2.0, 2.0, 4.0	this study
BAF	Sept 4, 1963	71.25 N	72.94 W	13 32 8.0	5.9	88°	77°	-103°	7	multiple source	this study
NB	Jan 9, 1982	46.98 N	66.66 W	12 53 51.7	5.7	175°	54°	85°	18	0.8, 0.8, 0.8	Nabalek, 1984
7-73	July 3, 1973	57.98 N	138.021 W	16 59 35.1	6.0	289°	17°	81°	6	2.0,.0.5, 1.5	Chandra, 1974
POC	Mar 28, 1975	42.061 N	112.548 W	2 31 5.7	6.1	7°	61°	245°	7	1.0, 0.0, 2.0	Burdick, 1981
N	Oct 5, 1985	62.237 N	124.266 W	15 24 2.3	6.5				10		

*For definitions see Langston and Helmberger (1975)

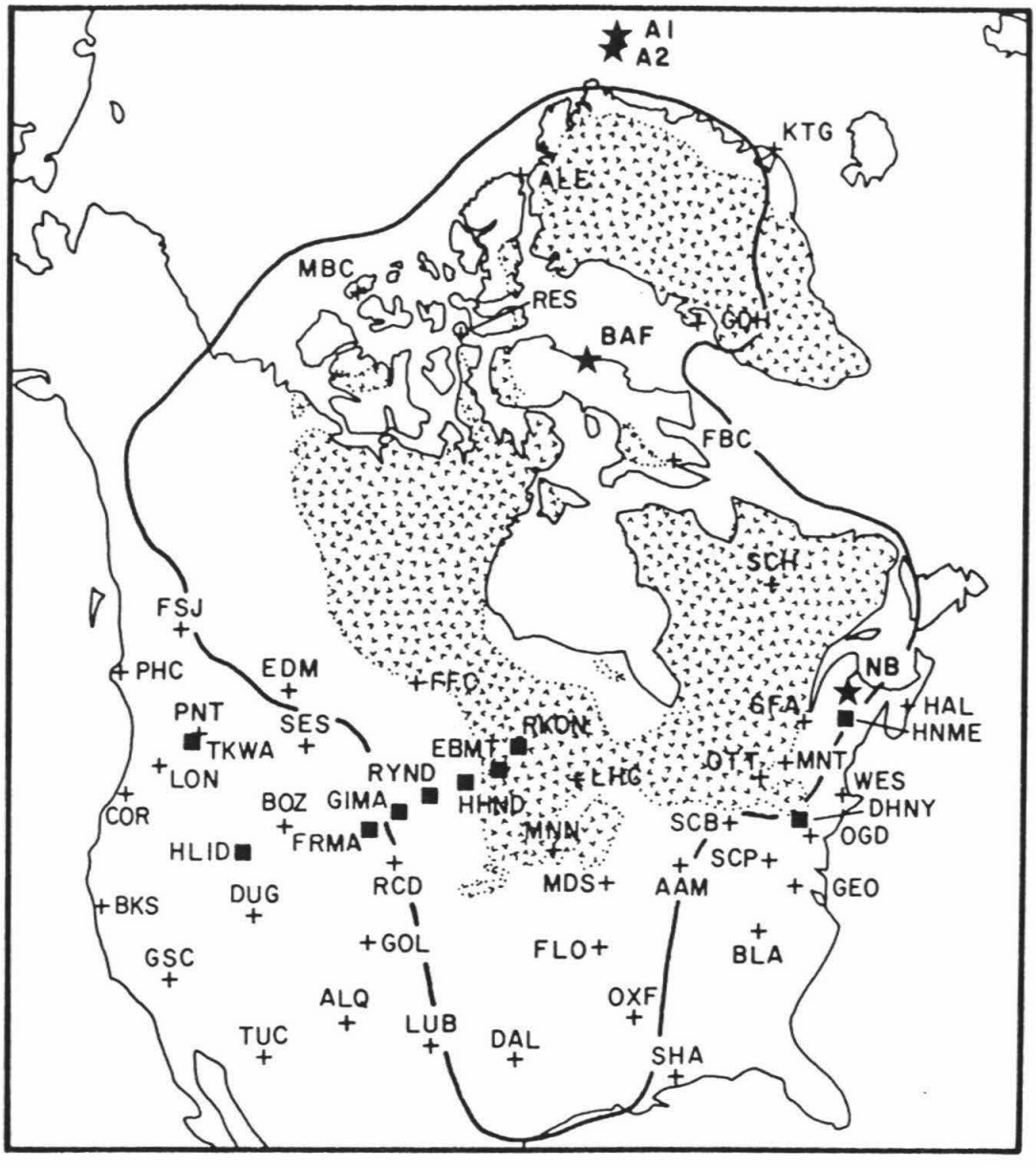

Figure 2.1: Events in eastern North America and stations. For the Baffin Bay event (BAF), both WWSSN (crosses) and LRSM (squares) stations are used. Only the WWSSN stations are used for the other events. Great circle paths are straight lines from the Arctic events. The outcrop area of the Canadian shield is shaded. The larger region enclosed by the heavy line is the area that was found by Grand (1987) to be fast for S-waves to a depth of at least 320 km.

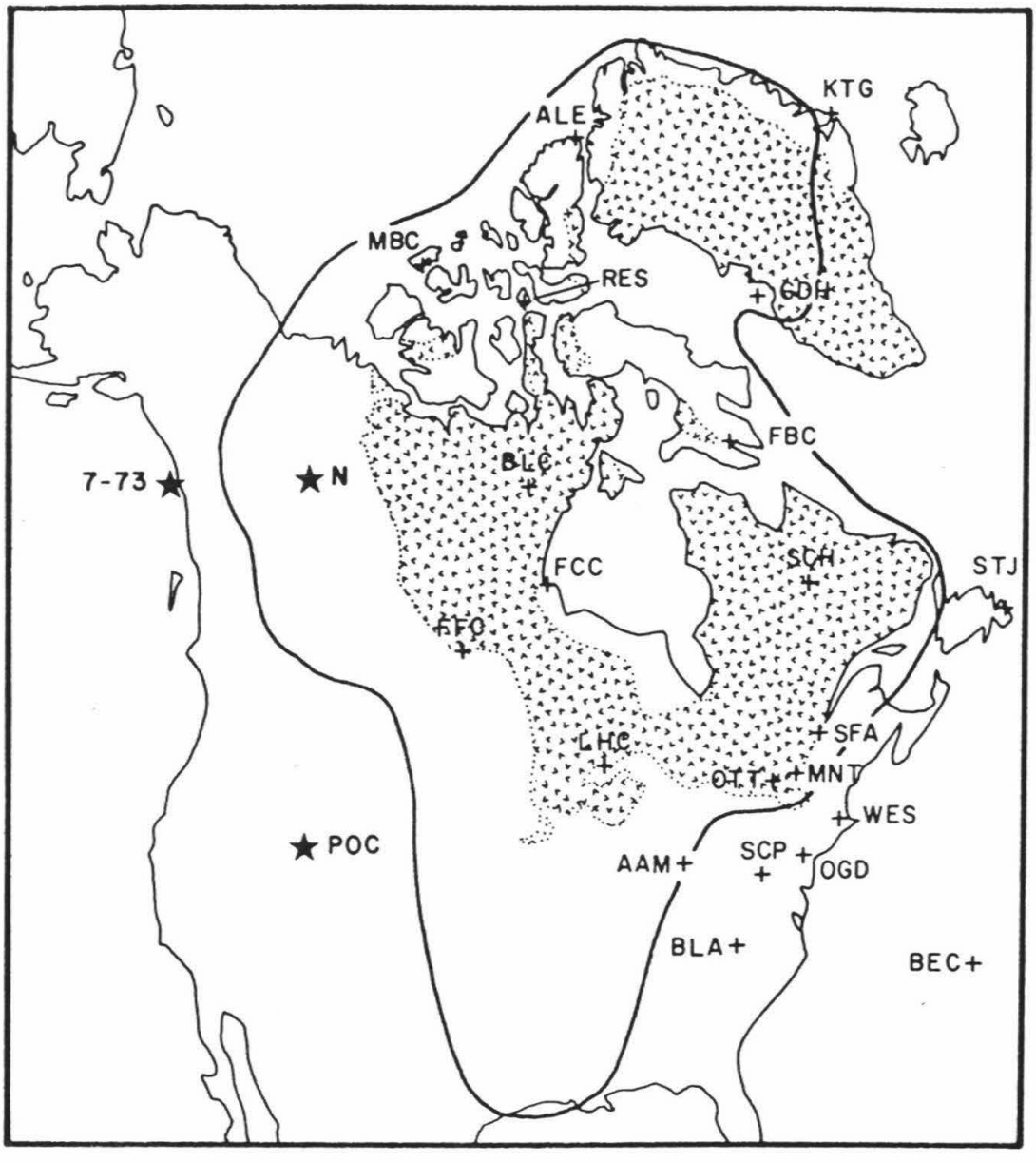

Figure 2.2: Events in western North America and stations. Great circle paths are straight lines from the 7-73 event.

The New Brunswick event occurred just outside the shield, and paths to the receivers used are almost entirely within the shield. The Arctic events designated A1 and A2 are located just outside the shield, northeast of Greenland. The source-receiver geometry for these events allows for very long paths within the shield and stable continent. To the west, the Pocatello, Idaho event is located just west of the stable continental region. This event was used by Burdick (1981) in developing his stable continent model S8, using P waves recorded at stations to the east. We use this event for PP, with the longer paths crossing a large portion of the shield. Also used is an event in July 1973 just off Juneau, Alaska. This event is valuable because of its thrust mechanism, unusual in this area, which produces strong P waves at upper mantle distances. The paths for this event cross a relatively narrow band of tectonically active region. The Nahanni event occurred after the bulk of this study was completed, and was used for travel-time information only. The Canadian shield is shaded in Figures 1 and 2, and it can be seen that we have paths crossing most of the shield. The larger region shown outlined is the region identified in Grand's (1987) S wave tomographic study as fast to at least 320 km.

Our velocity model for the Canadian shield, which is designated S25, is presented in Table 2.2, and is shown in Figure 2.3. Important features to note are a thick, high-velocity lid; a deep low-velocity zone, which is followed by a positive velocity gradient to the discontinuity at 405 km; and the discontinuity at 660 km. Also shown in Figure 2.3 are raypaths through the structure, illustrating several arrivals which will be discussed. A triplication curve is shown in Figure 2.4.

Table 2.2: Velocity Model S25

Depth, km	Velocity, km/s
0.0	6.400
39.9	6.400
40.0	8.323
70.0	8.365
100.0	8.408
130.0	8.450
165.0	8.500
190.0	8.420
215.0	8.330
250.0	8.403
300.0	8.508
350.0	8.612
404.9	8.778
405.0	9.208
450.0	9.393
500.0	9.599
550.0	9.804
600.0	10.010
659.9	10.257
660.0	10.673
700.0	10.822
750.0	11.008
800.0	11.090
850.0	11.173
900.0	11.255
950.0	11.338
1000.0	11.420

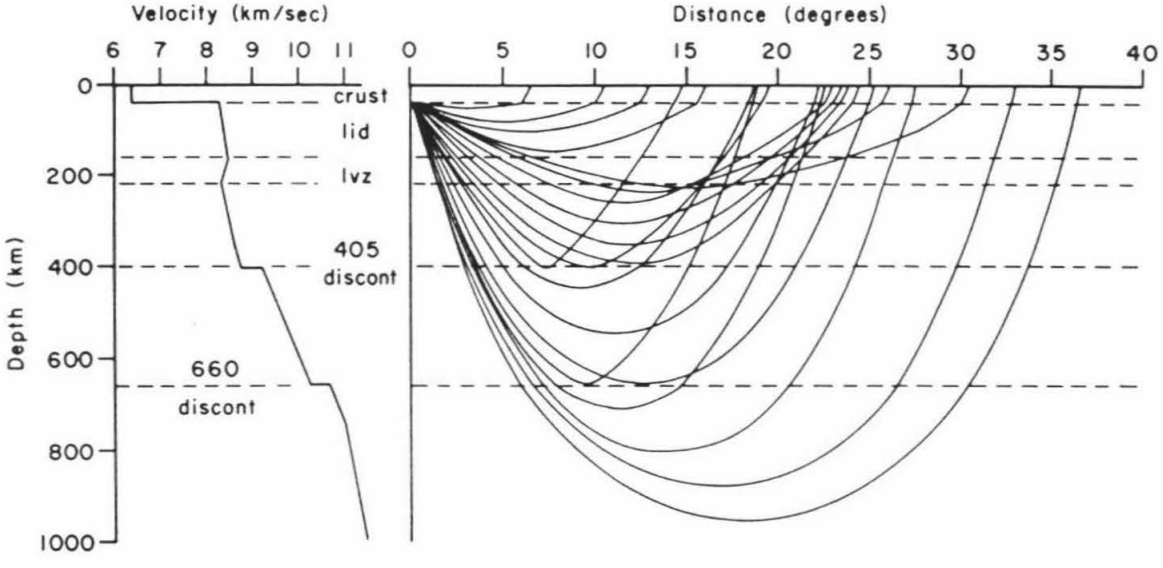

Figure 2.3: Velocity model S25 for the Canadian shield is shown on the left. Velocities are not earth-flattened. On the right, raypaths through the model are shown, illustrating the arrivals from the discontinuities and the persistent shallow arrivals from the lid and low-velocity zone.

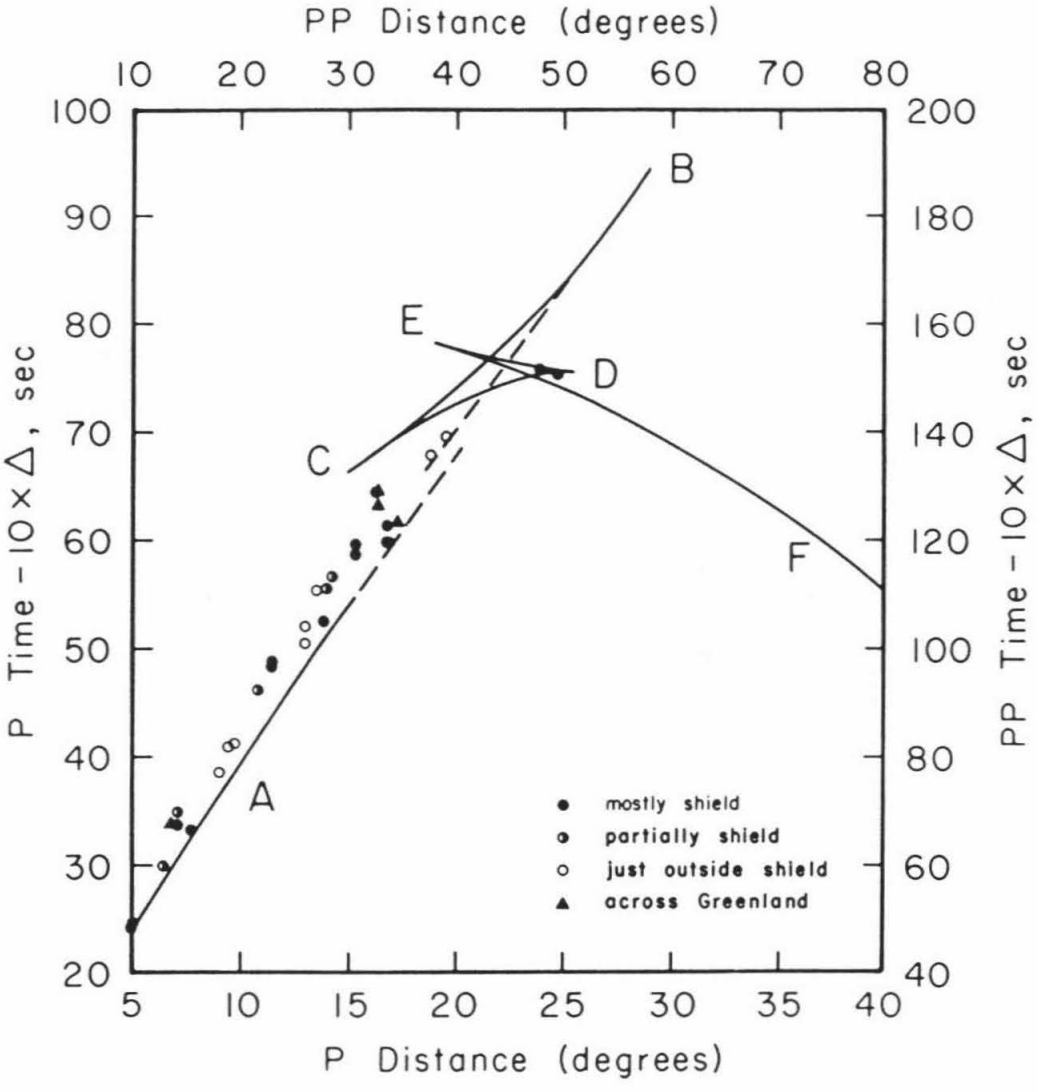

Figure 2.4: A triplication curve for model S25 with first arrival data collected from the events used in this study. Triplication branches are labeled.

In previous studies using waveform modeling to determine upper mantle structure, a rather simple progression could be followed in modeling P, with seismograms recorded at up to about 16^{o} revealing lid structure, seismograms at about 15^{o} to 23^{o} showing a triplication indicating the discontinuity at around 400 km, and records from about 20^{o} to 28^{o} revealing the deeper structure, including the discontinuity at around 670 km. In shield regions this progression of records with distance is not as simple, because of the effect of the thick lid and low-velocity zone. Arrivals from the uppermost 300 km actually persist far beyond the arrivals from the deeper discontinuities, as can be seen in the raypaths in Figure 2.3. These arrivals have been diffracted shallowly in the low-velocity zone. The triplication curve for our model shows the B branch extending to 30^{o}, a much greater distance than that for most other models. Beyond about 24^{o}, the B branch arrivals are not bottoming near the 400 km discontinuity as would be the case in most models, but are the shallow diffracted arrivals. These late arrivals are very sensitive to details of the shape of the lid and low-velocity zone. The effects of the lid and low-velocity zone make the modeling process somewhat more complex, as records from a wide range of distances must be used in determining the shallow structure. Records beyond 30^{o}, which in non-shield regions would not be influenced by lid structure, must be considered here in determining the structure above 400 km.

Travel-time and P_{nl} Data

Several types of data are useful in resolving the most shallow mantle structure. Most simply, direct measurement of arrival times at

distances of up to 1500 km provides a P_n velocity. Numerous studies of this type have been done in the Canadian shield. Refraction studies include the 1966 Early Rise experiment centered in Lake Superior, the 1965 Hudson Bay experiment, the 1968 Grenville experiment, and the 1966 Yellowknife experiment. These studies are reviewed by Berry (1973) and Berry and Mair (1977), and a few more recent results are summarized by Soller et al. (1982). In general, high P_n velocities are reported throughout the shield and the surrounding area, with considerable variations between studies. Some particular values will be discussed here.

Many velocity models have been determined using data from the 1966 Early Rise experiment. Masse (1973) combines many Early Rise record sections to obtain an average structure for much of central and eastern North America, including the shield, with a P_n velocity of 8.06 km/s, increasing to 8.37 at 78 km. Mereu and Hunter (1969) analyze sections from the Canadian shield and obtain similar values of P_n=8.05, increasing to 8.43 at 85 km. Gurbuz (1970) interprets a section in Ontario and Manitoba as showing a transitonal Moho, with a velocity of 7.9 at 35 km and 8.5 by 50 km, using converted phases and reflections. Data from the 1968 Grenville experiment in the northeastern shield are analyzed by Berry and Fuchs (1973), using synthetic sections as well as travel times. Average P_n velocity is reported as 8.06, with anisotropy of up to 0.17. Considerable regional variation is noted, with P_n values of up to 8.6 km/s reported for some profiles. From the 1965 Hudson Bay experiment, Hobson et al. (1967), Hunter and Mereu (1967), and Ruffman and Keen (1967) all report P_n velocities of approximately 8.25, although there are considerable differences in their

interpretations of local variations and crustal structure. Using recordings from the Canadian Seismic Network to supplement the Hudson Bay experiment data, Barr (1969) finds P_n velocities of 8.4 to 8.5 in the northern Hudson Bay, dropping to around 8.2 in the center. Moving to the western part of the shield, the Yellowknife refraction study of 1966 is described by Barr (1971). A P_n velocity of 8.1 is found in the shield east of station YKC, while to the west outside the shield it increases to 8.23. For the Greenland portion of the shield, very little data are available. A single study by Gregersen (1970) uses surface wave dispersion to estimate a P_n velocity of 8.05. A wide variety of crustal structures are reported in these studies, some with and some without a midcrustal discontinuity. However, throughout the shield and stable continent, the presence of an unusually thick crust is agreed upon.

Data from just outside the shield are also interesting and useful to us, since we are considering a somewhat broader area in this study. Although many studies report typical P_n values of 7.9 to 8.2, there are also many reports of very high P_n velocities outside the shield. For example, early refraction results by Cumming et al. (1962) in Alberta and Saskatchewan show P_n increasing outside the shield, with values of up to 8.3 in the Alberta plain. More recently, Greenhalgh (1981), using locally recorded mine blasts, finds upper mantle velocites of 8.3 to 8.8 in east-central Minnesota, although only a limited number of observations support the highest values. Zandt and Randall (1986) find a P velocity of 8.5 km/sec at 70-80 km beneath RSCP and RSON, using SV-P conversions. In the Appalachians east of the Canadian shield, some of the highest P_n values are reported. Studies of this region are

reviewed by Dainty et al. (1966). P_n velocities as high as 8.5 to 8.7 km/sec are reported in the central Appalachians, with velocities decreasing to about 8.0 km/sec on the flanks of the system.

This dataset shows considerable variation in P_n velocity, with values of 8.05 to 8.25 km/s common, but also with many reports of P_n velocities of 8.3 and above. One problem with this dataset is that most of this work used very high-frequency data, which is influenced strongly by local variations in velocity and Moho topography. Although considerable lateral variation in shallow structure is certainly present in the shield, for this study we would like a longer-period, more stable average value. However, the scarcity of sources within the shield makes long-period observations at this distance range hard to come by.

A few additonal observations are provided by the events used in this study, although for most of these events the paths contain a small non-shield portion near the source. We have measured travel times from these events, with origin times corrected for the depth determined through the teleseismic modeling, when this depth does not agree with the reported depth. Most of these times are measured from long-period recordings, but some short-period readings are included where the long-period signal was weak. These data are shown on the triplication plot in Figure 2.4, together with the time predicted by our model. In the model we use a simplified, average crustal structure of a 40 km thick crust with a velocity of 6.4 km/sec. Details of crustal structure will not influence the modeling of mantle structure. The lid velocity in the model is 8.32 at the Moho, increasing linearly to 8.50 at 165 km. These lid velocities are high relative to other regions, but are well

within the range of reported values for the shield. The travel-time curve for the model passes through the fastest data points, which should represent the behavior of the pure shield region. The considerable scatter in the data shows the difficulty in obtaining a good measurement of lid velocities using only travel-time data. As the shadow zone is having a greater effect, around 17^{o}, the scatter becomes greater, which may result from the more emergent first arrival being missed, or possibly from more lateral variation being seen in this feature. Additional support for the high lid velocities is provided by the waveform modeling of these records, discussed in the next section.

Some additional information on lid structure is provided by waveform modeling of $P_{\underline{nl}}$ at less than 1500 km. However, the $P_{\underline{nl}}$ waveforms are most sensitive to the source orientation of the event and much less sensitive to small variations in P_n velocity, and there is some tradeoff between P_n velocity and other parameters such as crustal velocity and thickness (Wallace, 1983). Also, we are again hampered by the small number of pure-path records available. The available records show a P_n velocity of at least 8.2. These records are presented in detail elsewhere (LeFevre and Helmberger, 1990). The $P_{\underline{nl}}$ modeling provides information primarily on the velocity at the top of the lid. Far more information on lid structure is provided by long-period records at larger distances. The records at $16-19^{o}$, showing both $P_{\underline{nl}}$ and upper mantle arrrivals, are particularly important.

P with $P_{\underline{nl}}$ Data and Modeling

Recordings at $16-19^{o}$ showing both $P_{\underline{nl}}$ and upper mantle arrivals were available from the Baffin Bay, Arctic, and New Brunswick events.

Unfortunately, only a single New Brunswick record provides a path within Canada, and no other events of sufficient magnitude have occurred near the shield within recent years. The records from the Arctic and Baffin Bay events have paths across the Greenland portion of the shield. However, the fit of the synthetics indicates that the differences between these areas are not large.

Figure 2.5 shows these records with a suite of synthetics for each. The observed seismogram is the middle trace in each group. Above it are synthetics computed using a uniform mantle t* of 0.7. Below are synthetics computed with no attenuation in the lid. In addition, each synthetic is shown with and without P_{nl}. No attenuation is included in the calculation of P_{nl}. It is interesting to observe which features of the seismogram result from upper mantle arrivals, and which from crustal (P_{nl}) arrivals. Although in general P_{nl} accounts for the later part of the record, there are also minor changes in the first few cycles when it is included. Some difference in the relative amplitude of P_{nl} to upper mantle arrivals is expected between the radial and vertical records, with the more vertically incident upper mantle arrivals stronger on the vertical record. This can be seen most clearly in the two components of A2-GDH.

At this distance range there are two predominant arrivals from the upper mantle: a ray that has bottomed within the lid and a later arrival, which is reflected from the 405 km discontinuity. This later arrival is indicated by arrows in Figure 2.5. Both the relative timing and the relative amplitudes of these arrivals must be matched. The timing and amplitude of the first arrival are controlled by the gradient within the lid, and by the depth of the low-velocity zone,

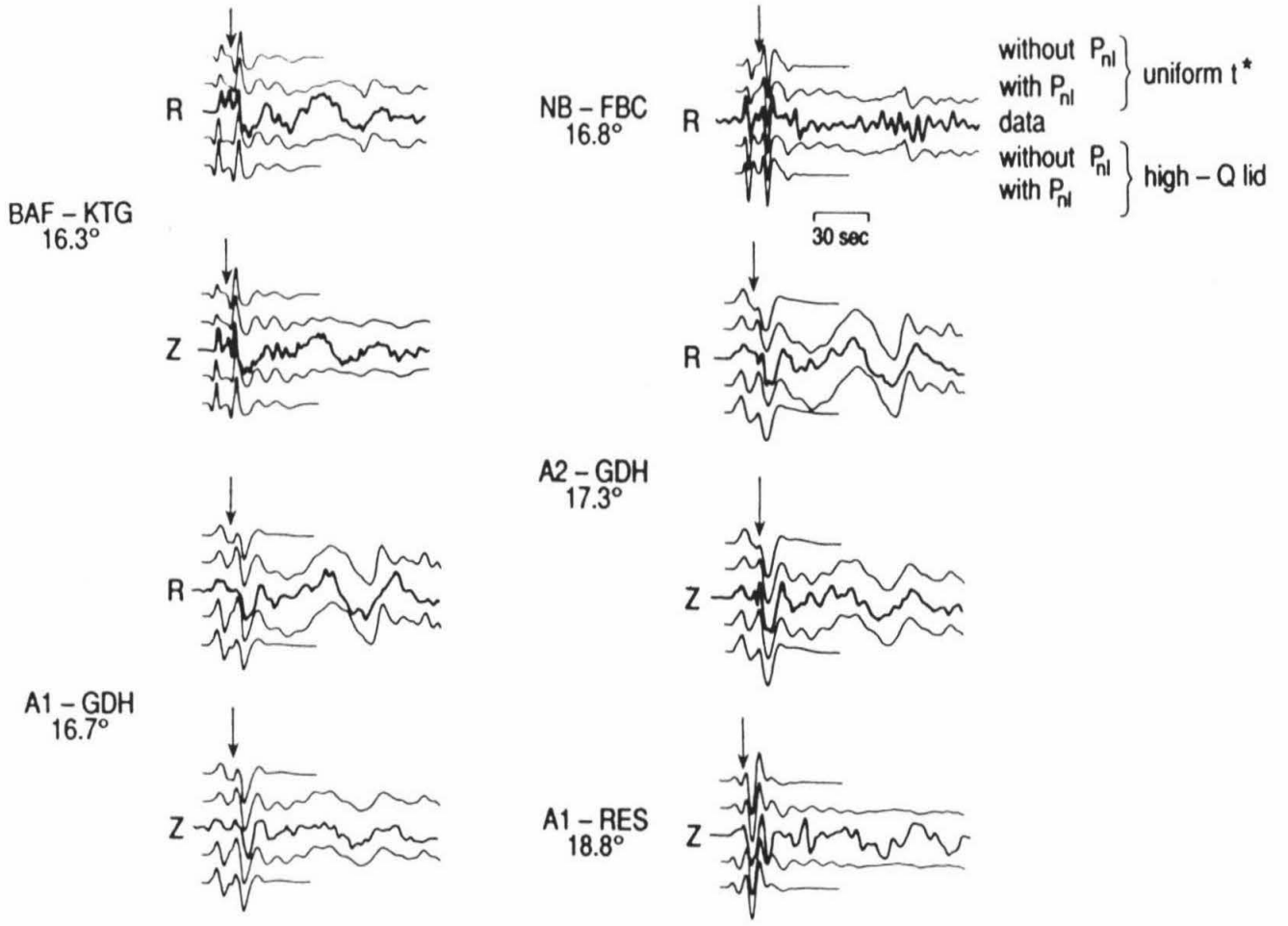

Figure 2.5: Data and synthetics from 16° to 19°, the distance range in which upper mantle arrivals are seen but P_{nl} is still strong. Synthetics are computed both with a uniform t* (above data) and with a high-Q lid (below data). In addition, each synthetic is shown with and without P_{nl} included. Arrows mark the arrival from the 405 km discontinuity. For some stations, only one component was available.

which causes the amplitude of this arrival to drop off with distance. Attenuation in the lid also strongly influences the amplitude of the first pulse. The timing of the second arrival is controlled both by the depth to the discontinuity and by the velocities throughout the upper 400 km, while the amplitude is controlled by the size of the discontinuity.

Looking through the synthetics, we see that in general the timing of the arrivals is fit quite well. The NB-FBC record, with a path within Canada, is fit particularly well. The timing of the second arrival is somewhat variable, with some of the records across Greenland, such as BAF-KTG, showing this arrival earlier than predicted by the model. This might be expected if the actual lid velocity is slightly lower here, slowing down the first arrival. The high-Q lid clearly fits better for the pure-shield paths such as NB-FBC and BAF-KTG; for the records from the Arctic events it is not so clear that a high-Q lid is necessary. By the last record, at almost 19^{o}, the first arrival has become emergent, and the Q in the lid has little influence on its amplitude. It is also interesting to look at the relative amplitude of P_{nl} to the upper mantle arrivals. The fit is surprisingly good in almost all of the records, considering the number of influences on P_{nl} amplitude. For example, this amplitude changes considerably with focal mechanism, and any irregularities in crustal structure are not considered. However, the excellent fit of these records for two minutes or so into the P wave train shows that the simple crustal structure is adequate for modeling of P_{nl}, even at relatively large distances.

P Data and Modeling

Next, we will examine a group of records at larger distances, which show the B branch of the triplication. Figure 2.6 shows a group of records from the Baffin Bay earthquake to stations in the USA and Canada. The paths are almost entirely within the shield. Looking first at the data on the right, a late arrival can be seen moving back through the section, persisting until at least 33^{o}. On the left side of the figure is a synthetic section. Several features were included in the modeling in an attempt to account for the complexity observed in the seismograms. First, this is a multiple source event. The source-time function, modeled from teleseismic records, requires that three subevents be used. In addition, most of these stations are nearly nodal. Because of the nodal character of the stations, and the wide variation in takeoff angle between the two major arrivals, the response from various depth ranges was computed separately, and the radiation pattern was calculated separately for each depth interval. Attenuation was also varied for rays bottoming in different intervals. No t* was applied to rays bottoming in the lid. For rays bottoming in the low-velocity zone, a t* of 1.4 was used. Below that, a t* of 0.7 was used. It was thought that a highly attenuating low-velocity zone might change the amplitude of the late arrival, which is a little bit too large on some of the synthetics. However, it was found that varying the t* in this way did not change the seismograms very much when compared with those computed with a uniform t*. Another possible source of complexity in the records could be multiple arrivals from within the lid. In the synthetics we included rays with one bounce within the lid. However, this inclusion made only a slight difference in the

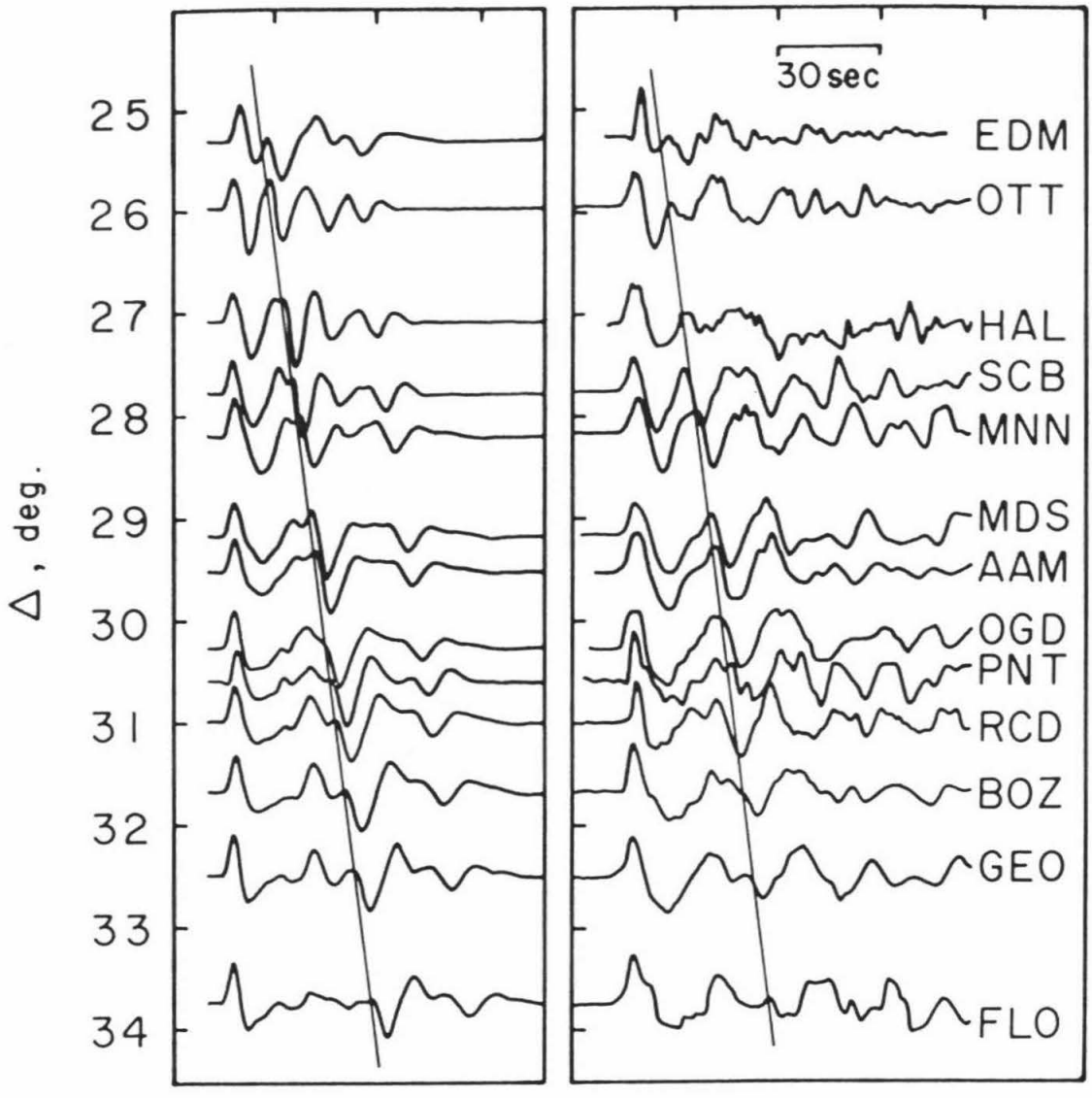

Figure 2.6: Data and synthetic profiles recorded at WWSSN stations at 25° to 34° from the Baffin Bay event. A line is drawn through both profiles to point out the secondary arrival.

synthetics, and did not improve their fit significantly.

A comparison of the data with the synthetic records shows that the timing of the late arrival is fit quite well. At these distances the first arrival is bottoming at 700 to 800 km, and the late arrival is from above 400 km. The relative timing of these arrivals therefore depends on both the overall travel time through the model, which controls the first arrival, and the exact shape of the lid and low-velocity zone, to which the timing of the late arrival is extremely sensitive. The amplitude of the first arrival is controlled by the velocity gradient at 700 to 800 km, and that of the late arrival by gradients within the lid and low-velocity zone. A more realistic Q structure would probably cause this arrival to die off faster. Also, since this arrival is so dependent on the presence of the thick lid and deep low-velocity zone, any heterogeneity encountered in leaving the shield region will stop this arrival. Some heterogeneity is seen in the data, with the timing of the later arrival varying by a second or so around the predicted value. However, only very minor variations in structure are required to account for this difference.

Additional data are provided by the inclusion of stations from the LRSM network, which was in operation at the time of the Baffin Bay earthquake. Figure 2.7 shows a profile at 22-30^{o}, with stations located from Ontario to Montana (see Figure 2.1). For each record the data are the upper trace, and the synthetic is below it. These recordings are longer-period than the WWSSN records, so that the individual arrivals making up the record are not as obvious. However, the late arrival is still clearly seen moving back through the section, and the timing and amplitude fit in the synthetics is good. In Figure 2.8

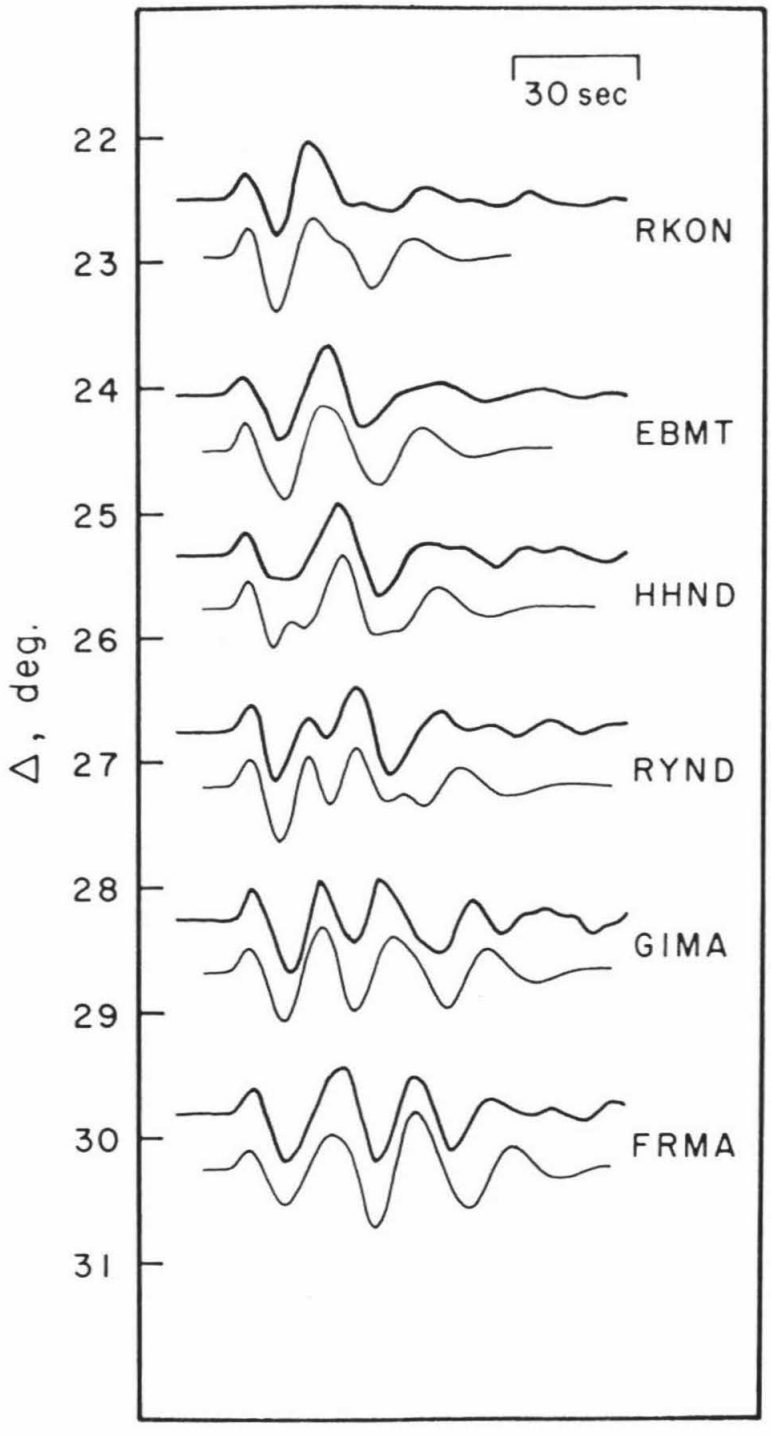

Figure 2.7: Data and synthetics for a profile of LSRM stations in Canada and the northern U.S., from the Baffin Bay event. The upper trace is the data.

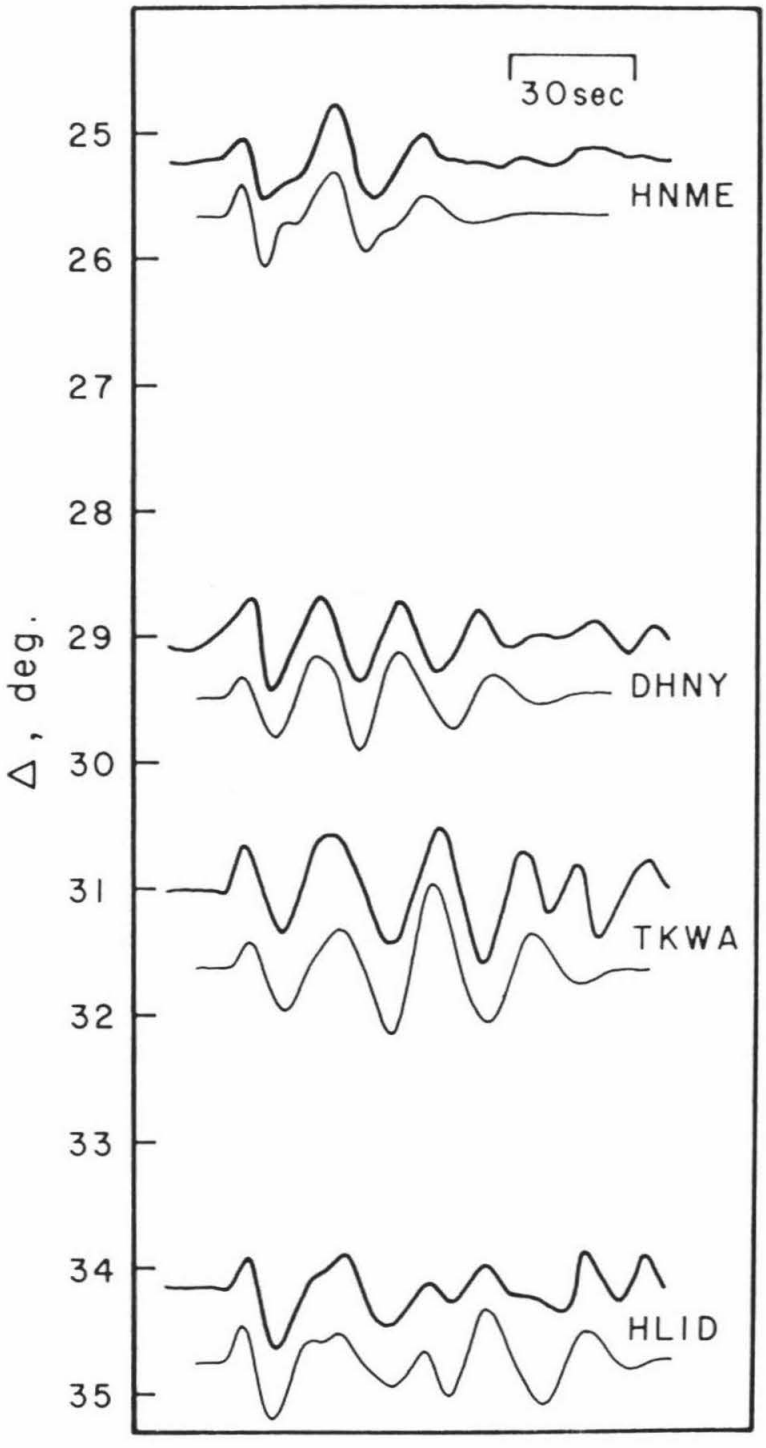

Figure 2.8: Data and synthetics for other LRSM stations, at a wide range of azimuths. The first two stations are in the northeastern U.S., and the second two are in the northwestern U.S.

four other LRSM stations are shown. These stations are from widely varying azimuths, with the first two stations in the northeastern U.S., and the others in Idaho and Washington. It is interesting that very little variation is noted in these records. The record at HNME, in Maine, matches very well with HHND in North Dakota, at the same distance. In the distance range 28-31°, the fit is equally good for DHNY, in New York, FRMA in Montana, and TKWA in eastern Washington. AT GIMA in Montana a slight difference in timing is seen, with the second arrival being earlier.

There is little evidence in any of the records presented here for the 660 km discontinuity. The D branch can be seen in the data in the first pulse at OTT and HAL, and as an inflection in the first pulse of the synthetics, where there is a slight mismatch in timing. The long-period LRSM records do not show the reflection as a distinct arrival, but its presence does influence the waveform. The gradients in velocity above and below 660 also influence these records.

PP Data and Modeling

The P dataset is quite incomplete, most notably between 19 and 25°, the middle of the triplication range. The inclusion of PP allows the gaps in the P dataset to be filled in and provides valuable additional constraints on the velocity structure. In particular, more information is provided on the structure of the discontinuities. In the PP data we see the earlier portion on the B-C branch, where it is from the 405 km discontinuity, and the D-E branch, which is hardly seen at all in the P data. Four events are used for PP (see Table 2.1): the Baffin Bay event; the July 1973 event off Juneau, Alaska; the

Pocatello, Idaho event; and the Arctic event A2.

The most complete profile is provided by the Arctic event, the location of which allows for paths of almost 60^{o} within the shield and stable continent. The records for this event are shown in Figure 2.9, along with synthetics, and the triplication branches are indicated on the figure. Throughout the section the PP-P timing is fit well. Multiple arrivals are clearly seen in the PP. The B-C branch is seen through most of the section. The records at around 48^{o} are especially important. The separation between the F and B branches can be seen clearly here, while at half this distance (24^{o}) we have little P data. The D-E branch influences the waveforms in the middle of the section, where the multiple arrival increases amplitudes. It can only be seen as a distinct arrival at around 43^{o}. The B branch is seen clearly in the data out to 53^{o} but is less clear after that. Although the data are sparse, the B branch does appear to die out faster in the PP than in the P. High attenuation in the low-velocity zone, which is not included in the synthetics, is probably contributing to this. In addition, lateral variations in structure are coming in, since these stations are no longer within the shield. The well-developed lid and low-velocity zone that are required to sustain the late arrival are no longer present.

In Figure 2.10 three records from the Pocatello event are shown. The Pocatello event, along with the July 1973 event, are valuable in that they provide a reversed profile from the Arctic and the Baffin Bay events. The fit of the synthetics, both in timing and waveform, is very good for these records. The KTG record at about 52^{o} is interesting since it shows the late B branch arrival, and the timing is

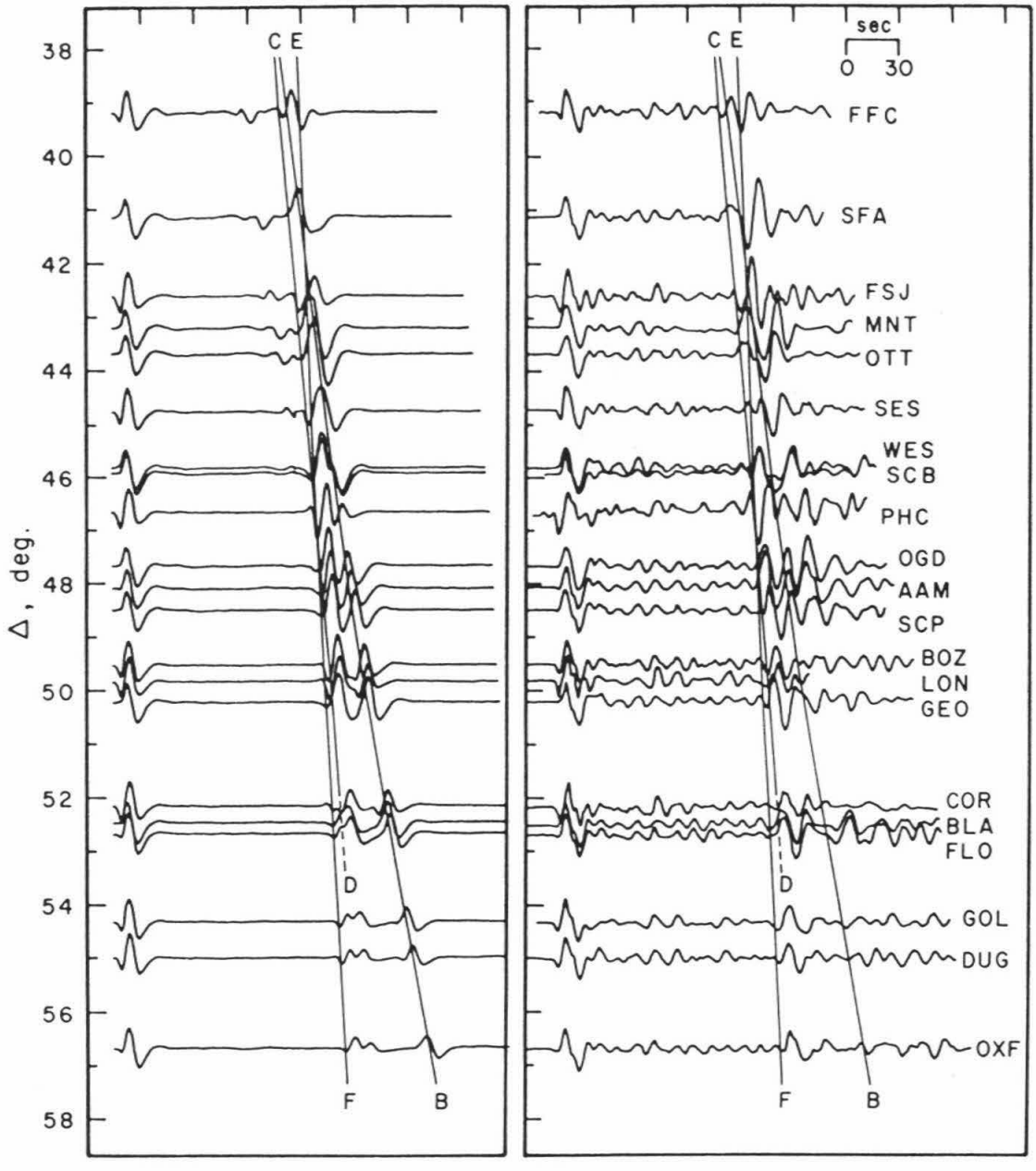

Figure 2.9: Data and synthetic profiles of PP from the Arctic event A2. The triplication branches are indicated. Because of the large shadow zone in model S25, the A branch does not produce a distinct arrival in this distance range, and so is not marked. Past about 50^{o}, the B branch is an arrival from just below the low-velocity zone. At $40\text{-}50^{o}$, this branch is the reflection from the 405 km discontinuity.

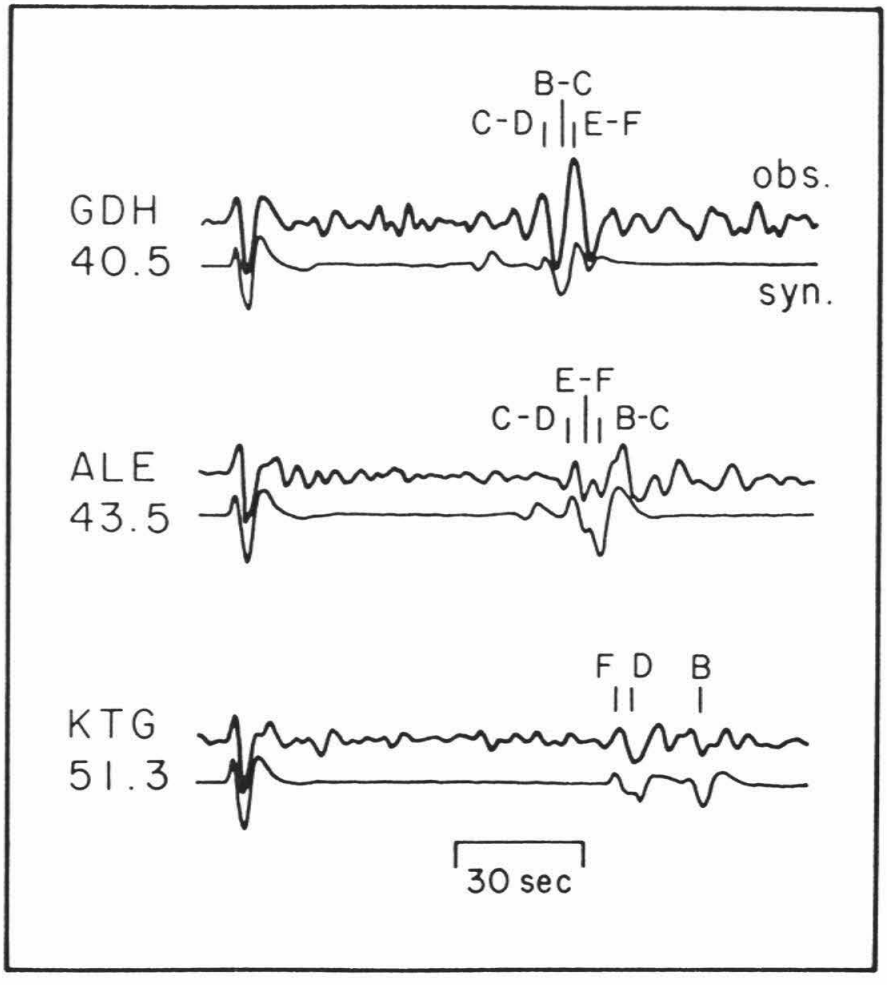

Figure 2.10: Three records from the 1975 Pocatello event, with multiple arrivals seen in the PP.

good. At this distance in the Arctic profile, this timing is not fit quite as well. This shows that there is some lateral variation in the structure, since for both events the paths are largely within the shield. The late arrival is quite sensitive to small changes in velocity in the lid and low-velocity zone, and a very minor variation in structure can account for this difference in timing. The E branch arrival can be seen at 43^{o} at ALE, where there is a complex interference pattern created by all of the triplication branches.

The profile from the July 1973 event is shown in Figure 2.11. At the distance range covered in this profile, $36-44^{o}$, the triplicated arrivals are close in time and the waveform is large and simple. The C and E branches cause the interference in the beginning of the waveform at $42-44^{o}$. The waveform fit is in general good, with the exception of the single record at 49^{o}, in which the timing is not fit as well as it is for the Arctic records at this distance. The PP-P timing is not fit quite so well as it is in the other sections, with the PP predicted by the model arriving one to two seconds too late. This is the opposite of what might be expected, since the source for these events is slightly outside the shield in a tectonic, and presumably slower, region. This again may indicate some lateral variation within the shield, with these paths crossing a particularly fast area.

The Baffin Bay event provides a short profile of PP, from $40-44^{o}$, shown in Figure 2.12. Although this distance range is covered in other profiles, the inclusion of these records provides a check on paths through a different portion of the shield. Again, waveforms are large and simple and are fit well. The PP-P timing is correct, with variations of one or two seconds seen between the records.

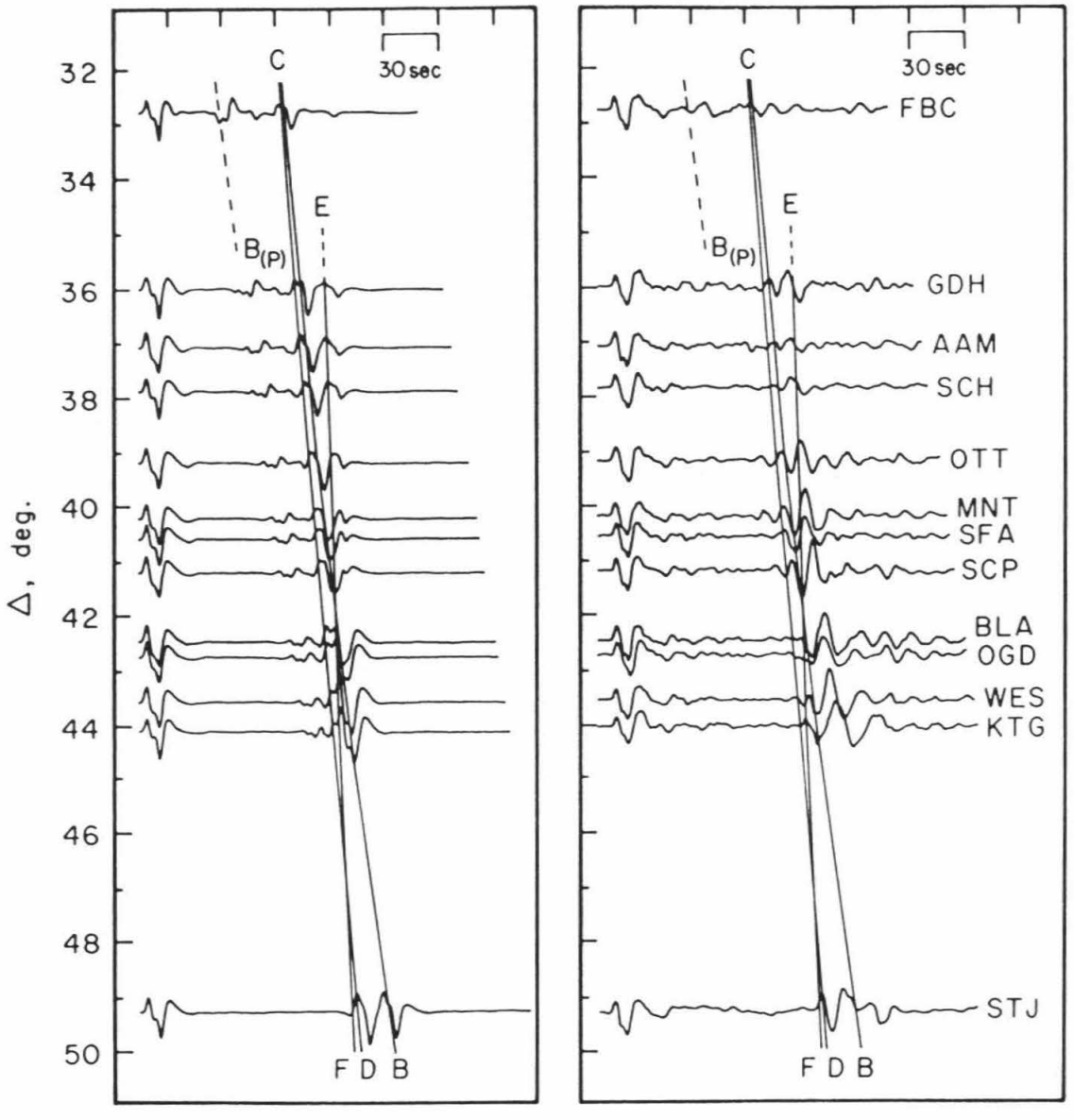

Figure 2.11: Data and synthetic profiles of PP from the July 1973 event. Triplication branches are shown for PP. In addition, the B-branch for P is present early in the section, but its amplitude is slightly overestimated in the synthetics.

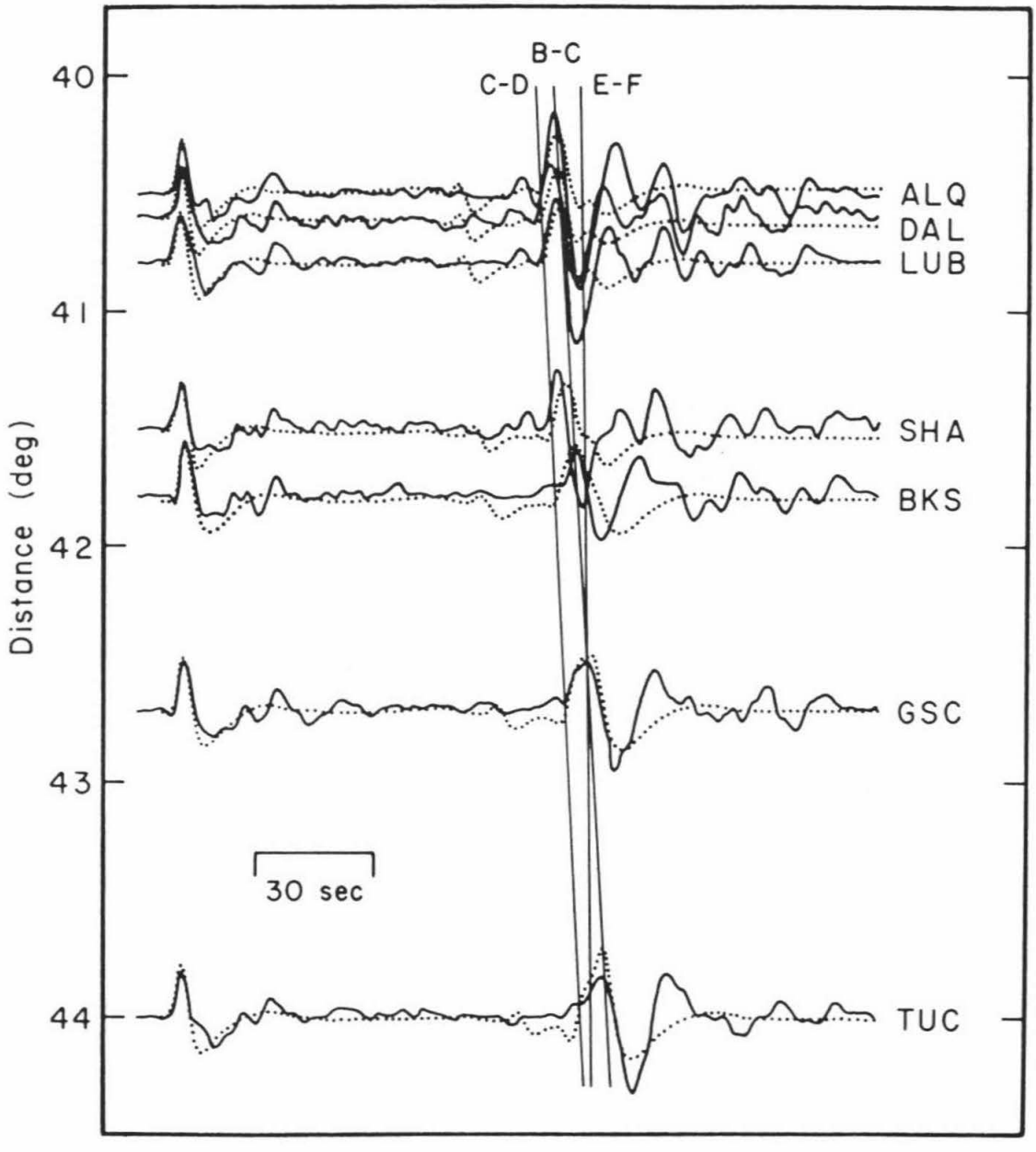

Figure 2.12: Data (solid) and synthetic (dashed) profiles of PP from the Baffin Bay event. Triplication branches are shown.

The fit of the PP waveforms, although good, is in general less satisfying than that of the P waveforms. Part of this is due to the WKBJ technique used to generate the PP synthetics, which is less exact than that of the generalized ray synthetics and tends to overestimate the amplitude of arrivals off the ends of triplications (for example, the B branch at large distances in the PP synthetics). However, aside from this there is clearly more complexity in the PP waveforms than we are modeling, especially late in the wave train. This is not likely to be due to any major structure in the mantle, since there is no evidence for it seen in the P waves. SV contamination is causing some of the complexity. Because of the extra bounce at the midpoint, there can be considerably more SV in the PP wave train than in the P, and it will appear late in the wave train, as seen.

Discussion

Although S25 adequately models the data we have presented, this alone does not tell us how well-constrained the model is. Since the forward modeling process does not provide a quantitative determination of error, some discussion is necessary of what we feel to be the margins of error on various features of the model. Several questions naturally arise in looking at the model and the data. For example, how well-constrained are features such as the depths and shapes of the discontinuities? Is the low-velocity zone in S25 truly necessary, or is it possible to create a late arrival such as that seen in the Baffin Bay profile with other structures?

The structure in the upper 400 km of S25 is the most tightly constrained by our dataset. The combination of data profiles at both

ends of the triplication range provides excellent control on velocity gradients in the lid and low-velocity zone. The depth of the 405 discontinutiy is slightly less well constrained, since the P data at 24-34^{o} do not show the actual reflection from the discontinuity. The data at 16-19^{o} show this reflection clearly; however, the timing of it is somewhat variable. Additional data are provided in the PP waveforms, where the timing of the B-C branch is fit well in the 40-48^{o} distance range. We are also relying somewhat on Grand and Helmberger's (1984) S wave study to set the depths of the discontinuities. Their study covered the same area, using many of the same events, and provided the basis for our starting model. The S and SS waveforms are more simple than P and PP, with the arrivals more separated in time, and show the discontinuities quite clearly. Using the P and PP data, a shift of 5 or 10 km in the depth of the 405 km discontinuity is possible; however, we found no reason to move the discontinuity, since this depth provides excellent fits with our data.

Moving to greater depths, the PP-P timing, which is much more consistent than the P travel times, provides tight constraint on the overall travel time through the model. The velocity gradient between 400 and 660 km is controlled by this and by the few PP records, which show an arrival from this depth range as the first arrival. We cannot rule out the presence of some small-scale structure in this region, such as the kink in gradient at 550 km reported in some previous models, but we certainly do not see any evidence for such structure. Information on the 660 km discontinuity and velocity gradients around it is provided by the records at the beginning of the Baffin Bay profile, where relative amplitudes are fit well. The PP waveforms also

provide some information. Unfortunately, we have very little data that clearly show the 660 km reflection, so that details of its structure are not resolved. However, the structure below 660 km must be fairly accurate, since the timing and relative amplitudes are fit well when the F branch is the first arrival.

It is interesting to compare S25 with various other upper mantle models. There is an enormous difference in the synthetics produced by different models in the upper mantle triplication range, and the effects produced by other models are helpful in understanding the constraints on various features of S25. We will discuss four other upper mantle models, two for shield regions and two for tectonically active regions. The models are shown in Figure 2.13. KCA was presented by King and Calcagnile (1976) for the Fennoscandian region, and was determined through inversion of $dT/d\Delta$ observations at the NORSAR array. There is no low-velocity zone in this model. K8, from Given and Helmberger (1980), is another shield model for Europe. It has a somewhat slower lid than S25, with a shallower low-velocity zone. T7, from Burdick and Helmberger (1978), is a model for the tectonically active western U.S. Both K8 and T7 were determined through forward modeling of long-period and some short-period WWSSN records. The fourth model, GCA (Walck, 1984), is a model for a spreading center, the Gulf of California. It was arrived at from analysis of travel-time, $dT/d\Delta$ and waveform data. T7 and GCA have very thin lids, and are much slower than S25 throughout the upper 200 km.

The records which we will discuss are presented in Figures 14 and 15. We show both the upper mantle step response (the derivative of this becomes the mantle response M(t) in Equation 1), and the complete

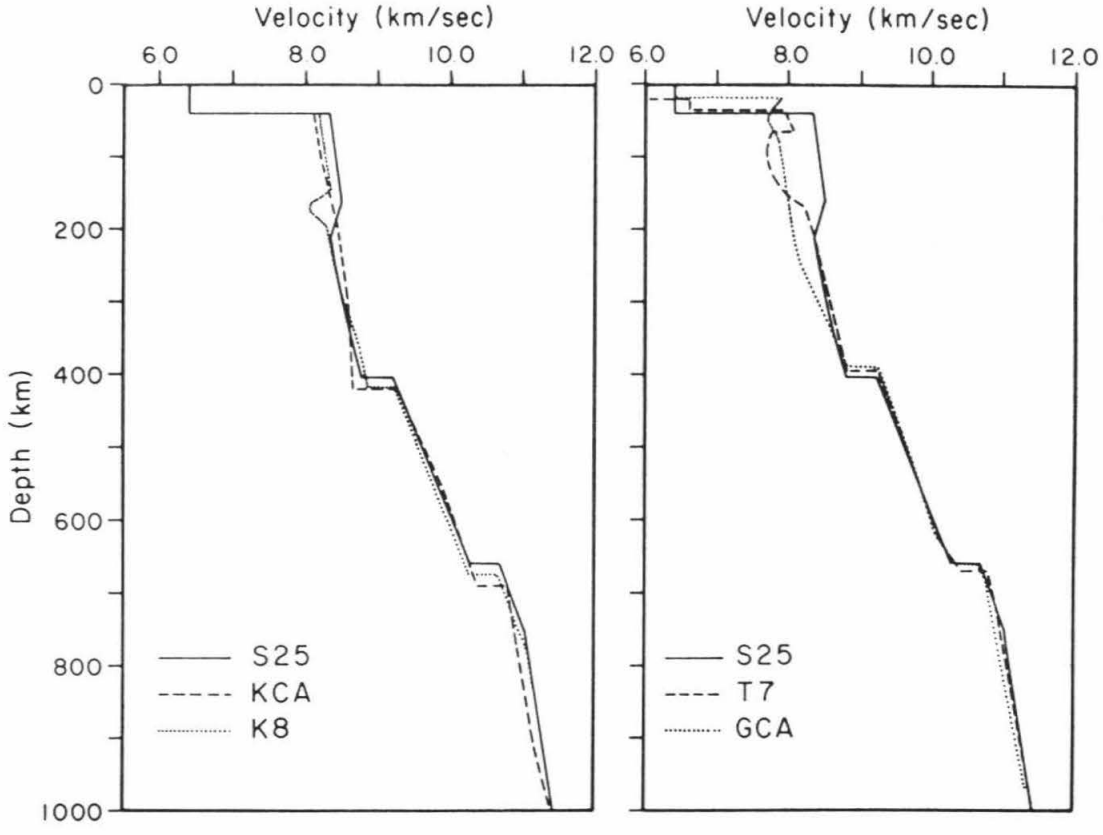

Figure 2.13: Velocity models S25 for the Canadian shield, KCA and K8 for the shield region in Europe, and T7 and GCA for tectonically active areas in North America.

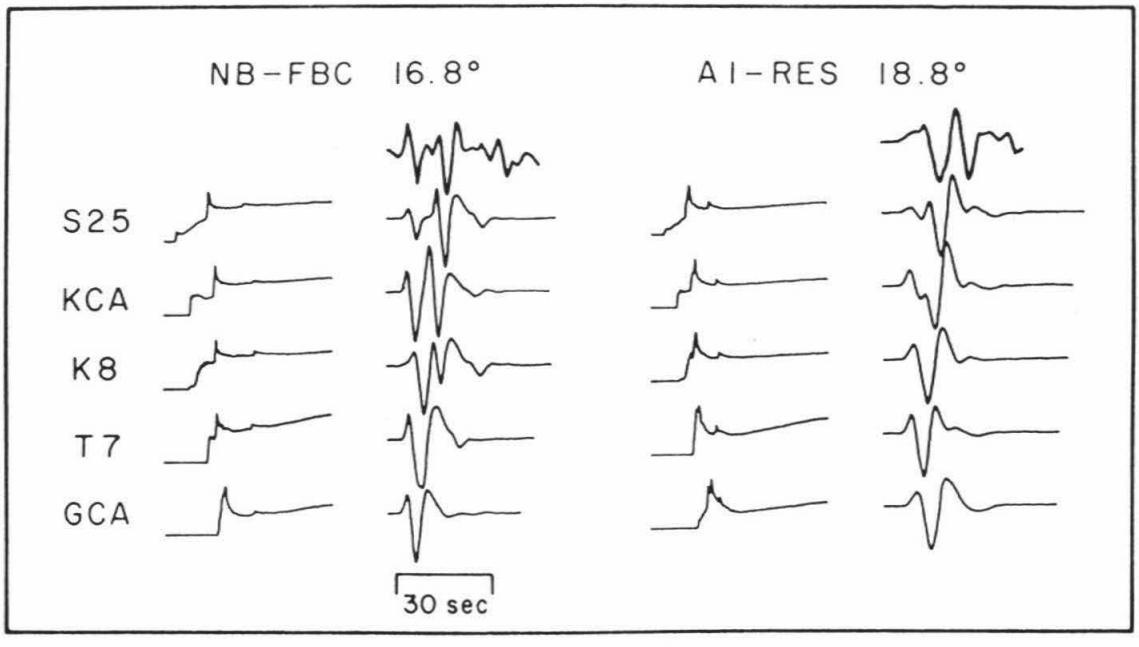

Figure 2.14: Upper mantle step responses computed for various velocity models, and synthetics calculated using these responses. The upper line in each group is the data. The step responses are shown on an absolute time scale, but the synthetics are aligned on the first arrival. Although the best fit for S25 was provided by a high-Q lid, for this example a uniform t* of 0.7 is used for all arrivals to facilitate comparison between the models.

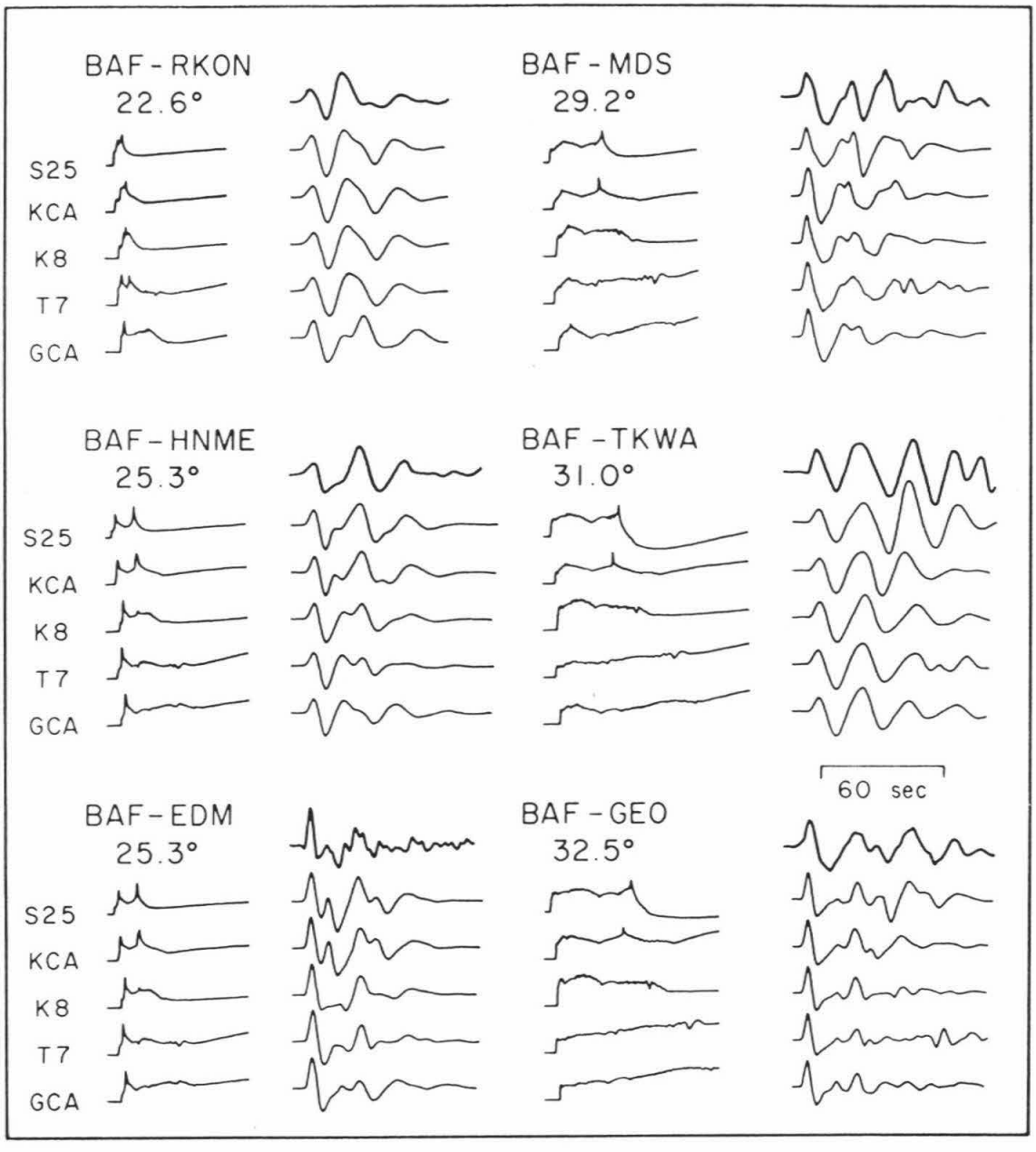

Figure 2.15: Upper mantle step responses computed for various velocity models, and synthetics calculated using these responses. The upper line in each group is the data. The steps are shown on an absolute time scale, but the synthetics are aligned on the first arrival. Both WWSSN and LRSM examples are shown.

synthetic computed using this response. The step responses are aligned on an absolute time scale to show the difference in travel times, but the seismograms are shifted so that the first arrivals are aligned, as would be done in the modeling process. All of the seismograms were computed using a t* of 0.7. This value is appropriate only for the shield region, but was kept the same for purposes of comparison. Also, although the high-Q lid provided the best fit for our data (Figure 2.5), for this comparison a uniform t* was used, since lid thickness varies between the models. In Figure 2.14, we look at records at 16.8^{o} and 18.8^{o}, showing the forward branch of the first triplication. At these distances, the step responses begin with an arrival from above 400 km, followed by a large arrival from the discontinuity around 400 km. The discontinuity at about 660 km produces a small arrival farther back in the response, which scarcely shows in the synthetic. In S25, the high velocities in the lid cause the first arrival to be early, so that there is a delay before the arrival from the 400 km discontinuty. This causes the two distinct arrivals in the NB-FBC record at 16.8^{o}. At 18.8^{o}, in the A1-RES record, there is still a well-separated first arrival, although it is now emergent. It can be seen that no other model produces this separation between these arrivals, including a model with a relatively pronounced lid such as K8. It is possible to create a model shaped like K8 that will produce the correct timing, by increasing the lid velocity and including a more pronounced low-velocity zone. However, such a model breaks down at greater distances, where the B branch is far too slow, and the PP waveforms are quite different.

Figure 2.15 shows six records at 23 to 32^{o}, covering the center

and back branches of the triplications. At 23°, our data are from the long-period LRSM instrument. All of the models have several arrivals in the first few seconds, and the long-period synthetics do not show any significant differences from each other. At larger distances the arrivals are more well separated and the differences between the models more apparent. Both a WWSSN and an LRSM record are shown at a distance of 25.3°. At this distance the initial large arrival is from the 660 discontinuity. S25 and KCA show a second large arrival from 400 km. The other models have no distinct second arrival by this distance. Moving out in distance, we have records at 29 to 32.5°. For all of the models, the responses at these distances begin with energy from around 800 km. A small arrival from the 660 km discontinuity can be seen just after the beginning of the step function at 29.2°, but is no longer seen by 32.5°. The later arrivals vary considerably for the different models. In the tectonic regions, the triplications are over, and the response has become essentially a smooth step. The synthetics are simple, showing only the source complexity. S25 and KCA show a distinct late arrival. For S25, this arrival is from rays which have interacted strongly with the low-velocity zone. For KCA, which does not have a low-velocity zone, the late arrival is the reflection from the large 400 km discontinuity in that model. The B branch persists to a large distance because of the extremely low gradient above the discontinuity. The B branch arrival in S25 is larger and comes in later, matching the time separation shown in the data.

The interpretation of the late arrival seen in the shield data is important to our results, since together with the data at around 17° it forces the inclusion of a low-velocity zone in the model. The

persistent late arrival in KCA, a model without a low-velocity zone, suggests another possible interpretation of the arrival, as a reflection from 400 km. In fact, it is possible to create a model with no low-velocity zone that does a better job than KCA of fitting our data, by speeding up the velocities in the upper 200 km and below 400 km so that they are closer to those in S25. However, even with velocities as fast as S25 in the upper 200 km, to speed up the A branch, the separation between the A and C branches is too small, and the B branch is too early. Lowering the 405 km discontinuity then improves the fit somewhat, but the B branch is still not matched well. In addition, the initial arrival at around 19^{o} is too large without the shadow zone effect.

Although S25 was derived from long-period data, this model has important implications for short-period propagation in the shield as well. The decay of short-period P_n amplitudes is known to vary dramatically in different tectonic provinces (Romney et al., 1962). Several features of S25 will tend to cause large short-period amplitudes. The slight positive gradient in the lid will increase P_n amplitudes relative to a model with no gradient or a negative gradient (Hill, 1971). In any model with a lid and low-velocity zone, the shadow zone that is created decays the short-period amplitudes more than the long periods (Helmberger, 1973b). The shadow zone in S25 does not occur until several degrees farther out than in tectonic regions. By the distance at which the shadow zone has decreased the P_n amplitudes considerably, the upper mantle arrivals from below the low-velocity zone are becoming large. Hence, the region of very low amplitudes between P_n and upper mantle P, which is seen in tectonic

regions, will not be nearly as pronounced in the shield. The low attenuation in the lid will also contribute to large short-period amplitudes. All of these effects combine to cause unusual short-period recordings, with high-amplitude, high-frequency signals seen far beyond where they might be expected in other regions.

It is interesting to compare S25 with Grand and Helmberger's (1984) S wave model SNA. This comparison of P and S is particularly valuable since both models were derived for the same area, using largely the same modeling techniques, although they rely more on SS than we do on PP. The shield P and S wave models are shown in Figure 2.16, along with tectonic models GCA for P waves (Walck, 1984) and TNA for S waves (Grand and Helmberger, 1984). Comparing the lids in S25 and SNA, there is a positive velocity gradient in the P wave structure, while the S wave structure shows a very slight negative gradient. We feel that the gradient in the P wave structure is quite well resolved. This feature in the S wave structure may be slightly less well resolved; however, it is possible that this difference in gradients is a real feature. The lid is 15 km thicker for the P waves, but that difference is probably not significant. The 400 km discontinuity represents a 4.9% jump in velocity for P and a 4.5% jump for S, about the same. The 660 km discontinuity jumps 4.1% for P and 7.5% for S. The larger jump for S at 660 km is seen in comparisons in many regions. Having P and S wave models for the same region allows an accurate calculation of the V_p/V_s ratio and seismic parameter ($\Phi = V_p^2-(4/3)V_s^2$), which is valuable since these parameters are sensitive to composition changes, while remaining relatively insensitive to temperature. Gradients in V_p/V_s and Φ provide information on compositional changes

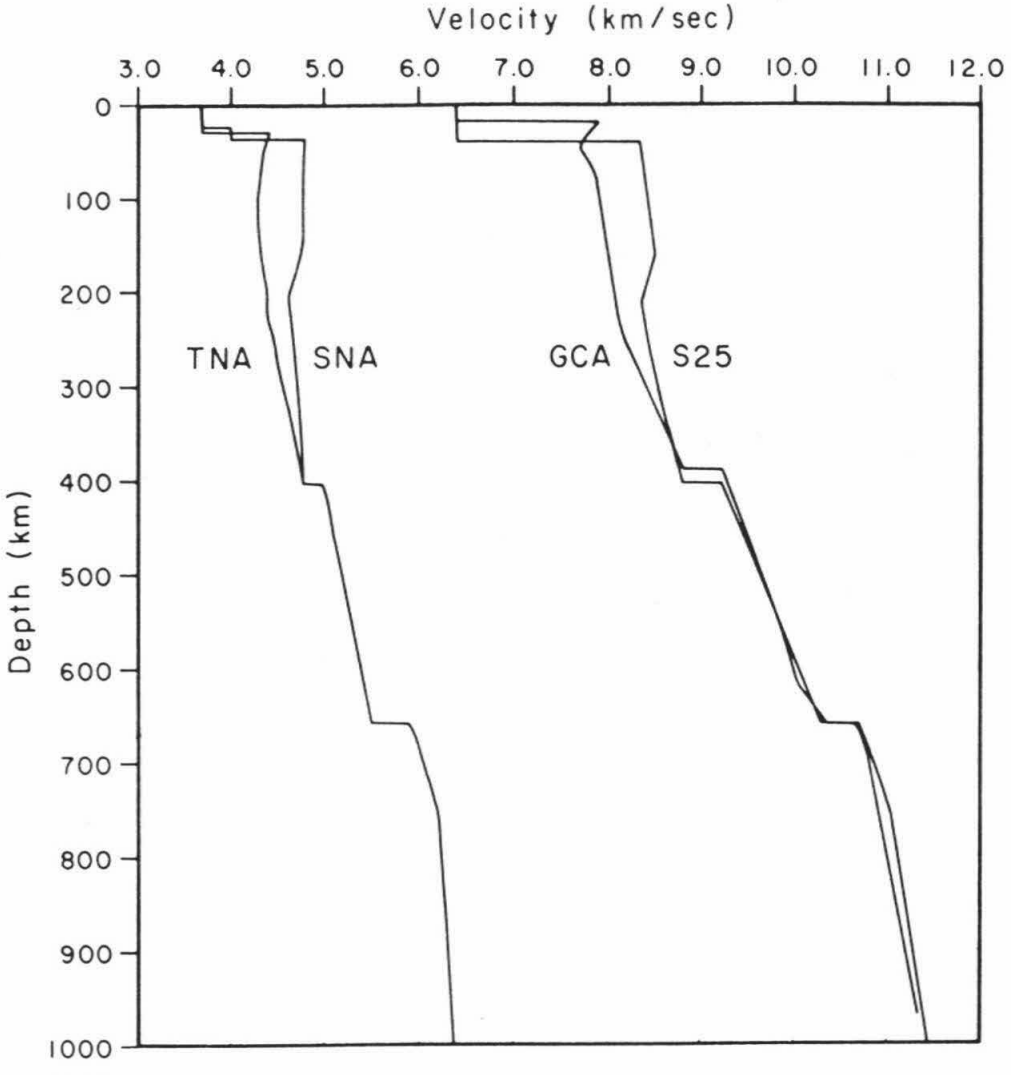

Figure 2.16: P-wave model S25 for the Canadian shield is shown with S-wave model SNA for the same area. Also shown are models for tectonic areas, GCA for P-waves and TNA for S-waves.

and partial melting in the upper mantle. Calculations of these values using S25 and SNA yield values more in line with a pyrolitic lithoshpere composition than those previously calculated for shield regions, using results presented in Anderson and Bass (1984). Several interpretations of these results are discussed in Duffy and Anderson (1989).

P wave velocity models are now available for many regions with various tectonic regimes. Using those models discussed in this paper (Figure 2.13), several points can be made about stable shield versus tectonically active regions. In comparing S25 with shield models KCA and K8, large differences (up to 5%) are seen in the structure above the 400 km discontinuity. Below the discontinuity the differences are about 1%. In comparing with tectonic models T7 and GCA, even larger differences, up to 8%, are seen in the uppermost mantle. However, again differences below the 400 km discontinuity are only about 1%, and there is no pattern of shield versus tectonic to the deeper variations. This difference of 1% is about the limit of resolution of these studies, so it may not represent a real difference between the regions. However, differences of this magnitude are being found in global studies of velocity variations (Woodhouse and Dziewonski, 1984; Dziewonski, 1984). Above about 300 km, the differences in structure are clearly resolved and represent a real difference between the tectonic and shield regions, and probably between various shield regions as well. The depth of the discontinuities is another potentially important difference between the various models. The "400" discontinuity varies from 390 (GCA) to 420 km (KCA), although the two extreme values are probably the least well resloved. The "660" varies

from 660 (this study, GCA) to 690 km (KCA). There is no consistent pattern of shield to tectonic in the variations. If well-resolved, this difference would be an exciting result from these studies, but unfortunately this is not the case. The depth of the discontinuity is determined by the timing of the reflection from it. In the model, this timing will be influenced by assumptions made about the shallow structure, and by any inaccuracies in the structure above the discontinuity. A careful comparison of data from each region will be necessary before any conclusion can be made about topography on the discontinuities.

Many questions remain on the differences between various shield regions. A model quite similar to S25 has been proposed for part of the Eurasian shield (Stork and Helmberger, 1985). However, K8, which covers a different portion of the Eurasian shield, has a significantly thinner lid and a more distinct low-velocity zone, and the data used in determining this part of their model are quite complete. Little work has been done on shield regions in South America and Africa, and models proposed for Australia (Simpson et al., 1974) are more similar to KCA, with no low-velocity zone. It is not known whether or not an S25-type structure may characterize many other shield regions.

Conclusions

The Canadian Shield can be modeled as a laterally homogeneous region using long-period P waveforms. The phase PP is valuable in providing additional data from a region where seismic sources are scarce. P_{nl}, P, and PP data together place tight constraints on the structure above 400 km and velocities below 400 km, although we did not

find enough data to constrain the shape of the 660 km discontinuity. Important features of our model, S25, are: 1) a thick, high-Q, high-velocity (P_n=8.32) lid; 2) a low-velocity zone, followed by a positive velocity gradient to 400 km; 3) a 5% jump in velocity at 400 km; 4) a simple linear velocity gradient to 660 km, where there is a jump in velocity of 4%. This model is quite different from other upper mantle models above 400 km, but only slightly different below that.

Acknowledgements

Steve Grand provided valuable advice throughout the course of this work. Gladys Engen helped with the computations, and Cindy Arveson helped with the data processing. This research was supported by the National Science Foundation grant EAR-8707709.

Chapter 3

P_{nl} Propagation in Eastern North America

Introduction

Earthquakes within the stable interior of North America, though relatively few in number, are of enormous importance because of concerns over seismic safety standards and siting of critical structures. Determinations of earthquake source parameters such as seismic moment, source duration and stress drop are always subject to some uncertainty. However, the exact values given to these parameters for a few large events in eastern North America can have a great influence on source-scaling relations being proposed for this region. For this reason, the larger events that have occurred within eastern North America, particularly since the advent of extensive instrumentation in the early 1960's, have been subject to extreme scrutiny. Still, basic questions such as magnitude/stress drop scaling remain quite open to debate.

For moderate-sized earthquakes, in the magnitude range 5.0 to 6.5, recordings at regional distances (5-15^{o}) will be particularly important. These events are not large enough to produce many good recordings at teleseismic distances, especially for long-period body waves, which contain much information about the overall source processes and size of the event. Any information about the seismic source that can be determined from the regional records will be

valuable. In this chapter, long-period regional records are used to study the sources of several eastern North America events. The portion of the records considered is P_{nl}, the entire wave train before the S arrival time. The P_{nl} waveform is relatively insensitive to source duration. However, it is quite sensitive to focal mechanism, and P_{nl} amplitiudes are stable and can be used to calculate the seismic moment. These calcuations are discussed for four eastern North America events. The moment calculations discussed here have been included as part of a larger study on scaling relations for eastern North American earthquakes (Somerville et al., 1987).

For most previous modeling of P_{nl}, a very simplified layer-over-a-halfspace model of the crust and mantle has been shown to provide surprisingly good results. However, with a structure such as that proposed in the previous chapter for the Canadian shield, the thick lid with a positive velocity gradient causes significant arrivals from within the lid at regional distances. The second part of this chapter consists of an investigation of the effects of lid structure on the P_{nl} waveforms. This investigation is useful for two purposes. First, we can better understand how good a fit can be expected, when using P_{nl} for calculations such as seismic moment. Second, these records can be used to study the lid structure of eastern North America, and its lateral variations. Unfortunately, there are not enough recordings for a comprehensive study of the region. However, the available recordings provide some valuable information.

Modeling Techniques

The term P_{nl} is used to refer to the entire wave train before the

S-wave time, in long-period records seen at regional distances. These seismograms are dominated by waves travelling in the crustal waveguide. In terms of rays, the wave train includes rays that have undergone multiple reflections within the crust, including mode conversions at the free surface and at the Moho. The initial part of the record is dominated by P headwaves (P_n) and the later part of the record includes more SV energy (PL).

The method of computing the P_{nl} synthetic seismograms is developed in detail in Helmberger and Engen (1980) and Wallace et al. (1981). Briefly, a simple layer-over-halfspace model is used to represent the crust and Moho. Green's functions are computed by summing generalized rays for various paths through the model. For example, the vertical displacement can be written as

$$w(r,z,\theta,t) = \frac{M_o}{4\pi\rho_o} \times (\dot{D}(t) \times \sum_{i=1}^{3} w_i(t) \times A_i),$$

where M_o is the seismic moment, ρ_o the source region density, $\dot{D}(t)$ the far-field time history, w_i are the Green's functions for the three fundamental faults, and A_i are orientation constants that depend on the source orientation. The Green's functions are computed by summing generalized rays, with multiples added until the waveform does not change significantly with additional rays. This requires up to 3 to 6 bounces in the crust, depending on distance. Both P and SV modes, in all combinations, are included.

Since the computation of the Green's functions is rather time-

consuming, they are computed for each of the fundamental faults, at 100 km intervals from 200 to 1400 km, and stored. A synthetic for any desired fault orientations can then be created by computing the appropriate A_i's, summing, and convolving with the source-time function and instrument response. When the desired distance falls between those of the Green's functions, the closest distance can be used rather than recomputing the Green's function for the exact distance. This approximation is quite adequate since the waveforms at adjacent distances do not change abruptly (Helmberger and Engen, 1980).

The Green's functions are calculated for an average continental crustal structure, given in Table 3.1, and a source depth of 8 km. Although this model is obviously simplified, it has nevertheless been shown to work quite well for modeling of P_{nl} in most continental regions (Wallace and Helmberger, 1982). Variables that need to be considered in the structure include crustal thickness, P_n velocity, and the presence of a mid-crustal discontinuity. Wallace (1983) presents illustrations of the effect of changing each of these parameters. Increasing crustal thickness and increasing P_n velocity primarily affect the separation between P_n and direct P, and hence the dispersion of the waveform. The effect is small for reasonable variation of these model parameters, and is similar to the effect of increased distance. If necessary, these variations in structure can be accounted for by using the response calculated at the next larger distance. An example is also shown by Wallace of a calculation including a mid-crustal discontinuity. It is found that the long-period waveforms are not significantly affected unless the discontinuity is extreme.

Table 3.1

Crustal Structure for P_{nl} Modeling

Thickness (km)	P wave Velocity (km/s)	S wave Velocity (km/s)	Density (g/cm^3)
32	6.2	3.5	2.7
--	8.2	4.5	3.4

The Green's functions used here are calculated for a source depth of 8 km. The effect of varying source depth is discussed in Helmberger and Engen (1980). They show that increasing source depth increases dispersion of the waveform, again an effect similar to that of increased distance. For events of source depth somewhat greater than 8 km, a slightly increased distance will approximate satisfactorily the effect of the change in source depth. This is a problem for only one event discussed here.

Because of the flat-layered, simple structure of the model, it is expected that the synthetic waveforms may contain more high frequencies than the data. Non-uniformity in structure or less sharpness in boundaries in the real earth will diminish the high frequencies. For this reason it may be necessary to filter the data and synthetics. This is done by convolution with a 1.5 or 2.0 s triangle.

Determination of seismic moment using P_{nl} is discussed in Helmberger and Engen (1980), Wallace et al. (1981), and Wallace and Helmberger (1982). Their comparisons show that seismic moments determined from P_{nl} modeling compare well with those determined through body and surface wave modeling. Because the effects of Q on P_{nl} are negligible, these moment estimates may be more accurate than those obtained from teleseismic body and surface waves.

Seismic Moment Determinations Using P_{nl}

This section describes the analysis of P_{nl} records from four eastern North American earthquakes, primarily for determination of seismic moment. Event and station locations are shown in Figure 3.1. Origin times and locations are given in Table 3.2.

Table 3.2

Earthquake Locations

Event	Date	Time	Lat.	Long.	Depth	m_b	M_s
Baffin Bay	1963/ 9/ 4	13:32: 8.0	71.30N	73.00W	7.0	5.9	
New Brunswick	1982/ 1/ 9	12:53:51.7	46.98N	66.66W	7.0	5.7	5.2
Illinois	1968/11/ 9	17: 1:42.0	37.95N	88.48W	18.0	5.3	
Kentucky	1980/ 7/27	18:52:21.8	38.18N	83.94W	13.5	5.2	4.7

Baffin Bay, 4 September 1963

The Baffin Bay earthquake was a relatively large (m_b = 5.9) event located along the margin of the Canadian shield. Long-period teleseismic P waves from this event were modeled by Liu and Kanamori (1980). They determined a focal mechanism of strike=98°, dip=66°, and slip=-103°, a source depth of 7 km, and a moment of 1.7×10^{25} dyne-cm. An inversion of P_{nl} data from three stations was done by Wallace and Helmberger (1982). They obtained a focal mechanism of strike=74°, dip=66°, and slip=-100°, but did not calculate seismic moment. This event has also been used extensively in modeling of upper mantle structure of the Canadian shield (Chapter 2).

Four stations with a good distribution of azimuths are available for modeling P_{nl}. These are the WWSSN station GDH and three Canadian stations, listed in Table 3.2. A reproduction of the east component seismogram at station RES is shown in Figure 3.2, illustrating the good

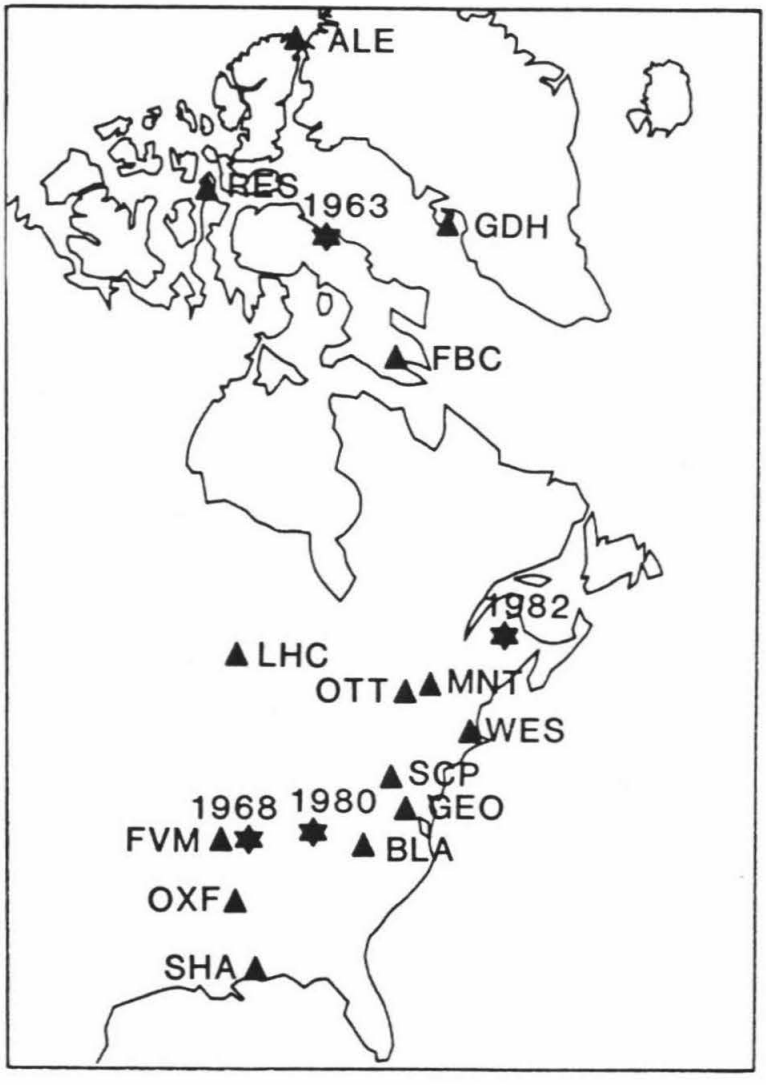

Figure 3.1: Stations and events discussed in this chapter. Locations are shown for the 1963 Baffin Bay, 1982 New Brunswick, 1968 Illinois, and 1980 Kentucky earthquakes.

signal-to-noise ratio of the P_{nl} recordings of this event. This event is at the lower end of the magnitude range for teleseismic modeling of the long-period records, but the P_{nl} recordings are excellent.

Table 3.3
Seismic Moment Estimates of the
September 4, 1963 Baffin Bay Earthquake

Station	Distance	Azimuth	Moment Ratio
GDH	765 km	98°	Z 3.78+ R 2.30+
RES	802 km	308°	Z 0.64 R 0.53
FBC	866 km	165°	Z 0.54 R 0.53
ALE	1273 km	7°	Z 1.89 R 1.89

+nodal, not used in final calculation

One of the previously determined focal mechanisms for this event (Liu and Kanamori, 1980) was determined from a subset of the available teleseismic records. The other (Wallace and Helmberger, 1982) was determined from three of the four available P_{nl} recordings. Both of these mechanisms prove unsatisfactory when applied to the other dataset. Combining all of the long-period data on this event (P_{nl}, upper mantle, and teleseismic) we prefer a revised mechanism of strike=78°, dip=70°, and slip=-100°.

Data and synthetic waveforms are shown in Figure 3.3. A time function of 0.75, 1.0, 0.75 sec was used for the synthetic waveforms, and no filtering was done. The match to the data is quite good for RES and FBC. At station GDH, the downgoing P waves leaving the source are

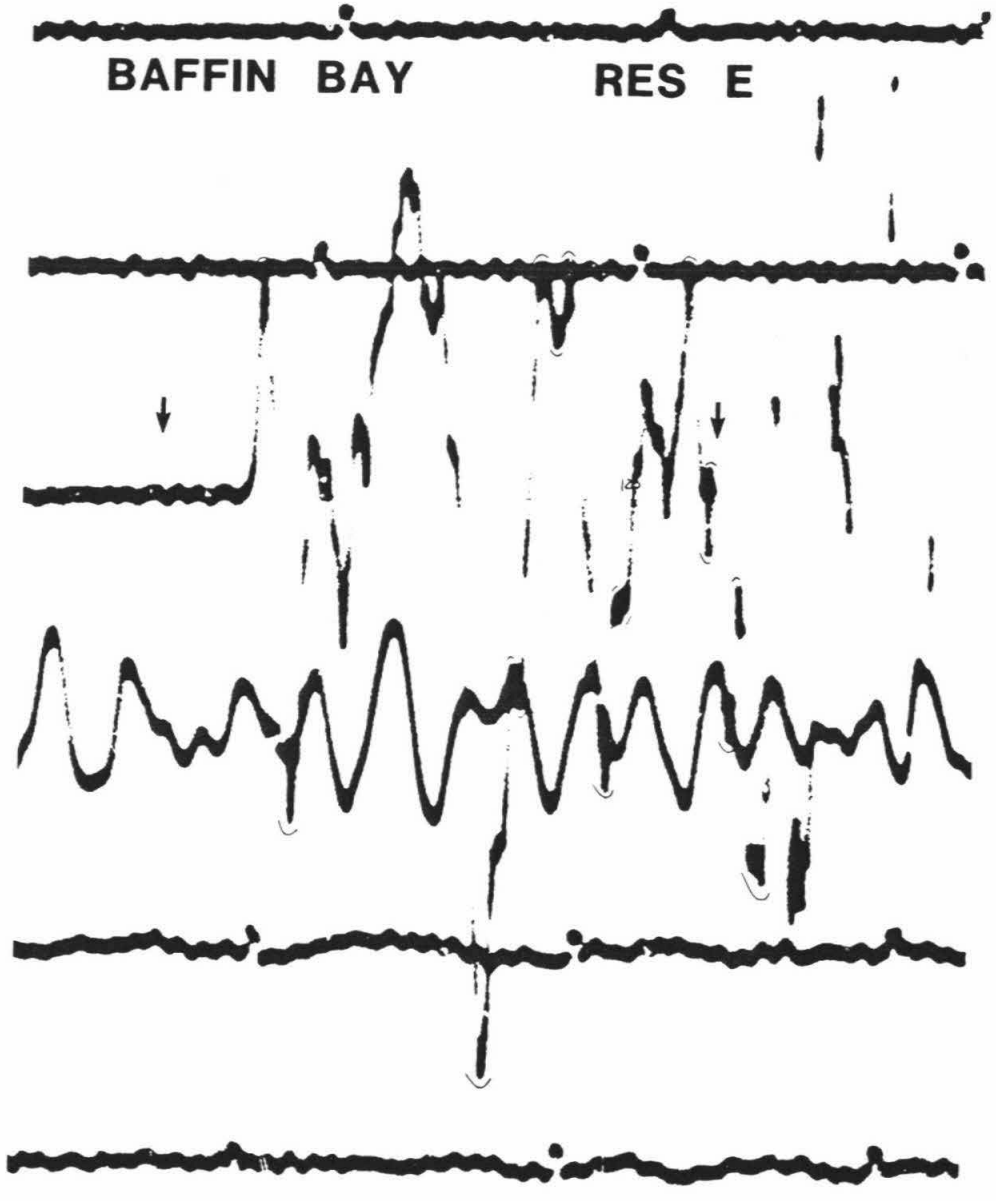

Figure 3.2: An example of high-quality P_{nl} data from the m_b=5.9 Baffin Bay earthquake. Arrows indicate the portion of the record that is modeled. This event is only just large enough for modeling of the teleseismic long-period waveforms.

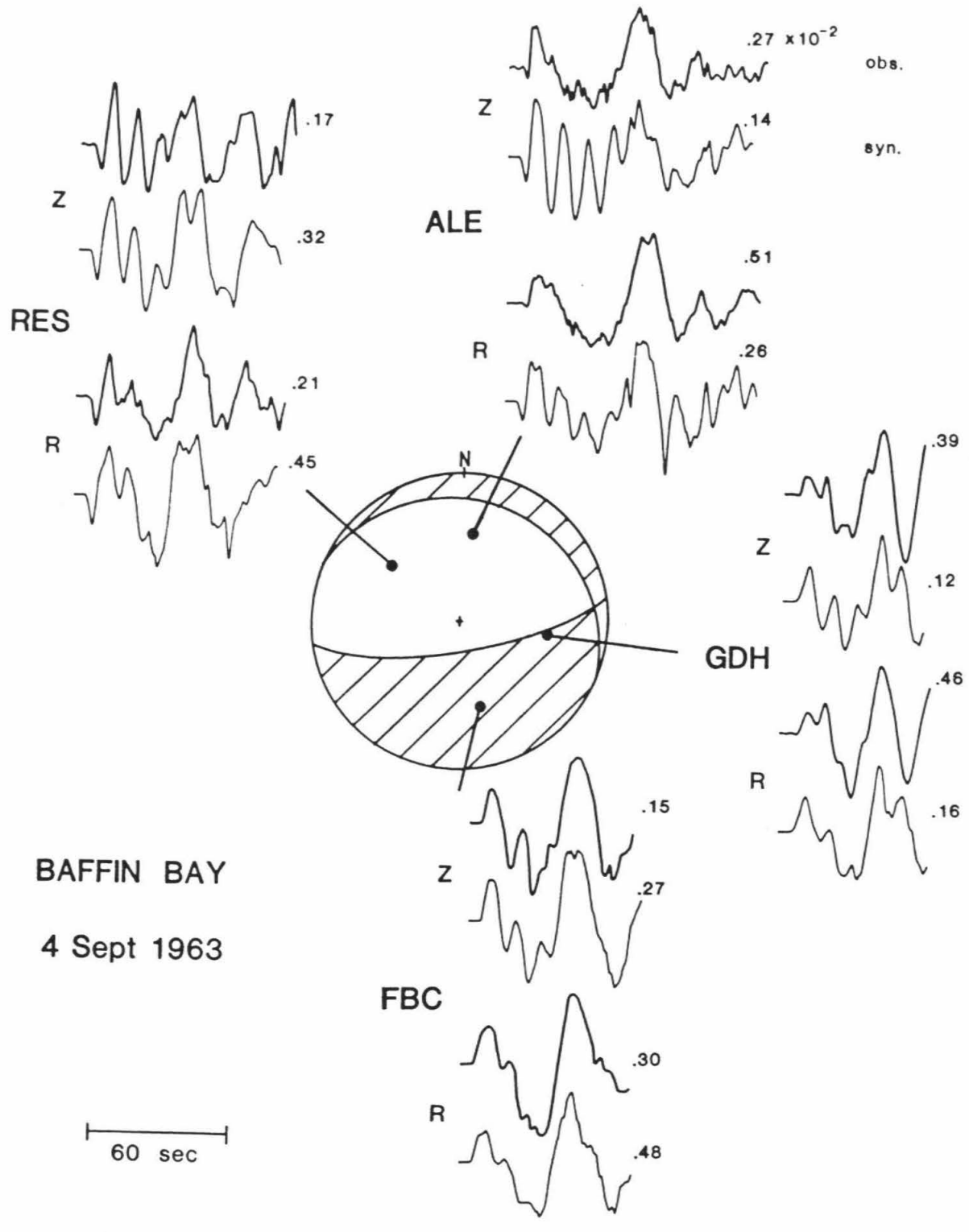

Figure 3.3: Observed (upper) and synthetic (lower) P_{nl} waveforms for the 1963 Baffin Bay earthquake, with both radial (R) and vertical (Z) components shown. Peak-to-peak amplitudes are given in cm x 10^{-3}. Synthetic amplitudes represent the average moment of 2.2 x 10^{25} dyne-cm determined from the modeling of these records.

nearly nodal. The amplitude of the synthetic is not stable for this station, changing rapidly for small changes in mechansim. Although the waveform fit is good, this station is not included in the moment calculation. The waveform mismatch at ALE is problematic. The focal mechanism is quite well constrained, with a large dataset from all azimuths. Even fairly large adjustments to the source orientation do not improve the fit at this station. This station is included in the calculation of seismic moment, with the amplitude comparison based on overall fit to the long- period (PL) part of the waveform, not the first few swings (P_n) which are not fit well.

The calculation of seismic moment is described in Table 3.3. The moment ratio given in the table is defined as the ratio of the moment that would be calulated from this record alone to the final moment, which is determined by averaging all of the stations. The seismic moment for this event, determined from the three non-nodal stations, is 2.2×10^{25} dyne-cm, which is just slightly larger than the body-wave estimate of Liu and Kanamori (1980).

New Brunswick, 9 January 1982

This earthquake was the mainshock of the New Brunswick sequence. An inversion of teleseismic body-wave data was performed by Nabalek (1984) to determine source orientation, time function, and moment. He found strike=175°, dip=54°, rake=85°, source depth=7 km, and $M_o = 1.6 \times 10^{24}$ dyne-cm. Four stations, listed in Table 3.4, provided usable waveforms for P_{nl} modeling. Three are WWSSN or Canadian, long-period (analog) records, and one is from the digital WWSSN station SCP. Data and synthetic waveforms are shown in Figure 3.4. Both have been

convolved with a 2 sec triangle, which has little effect on the data but removes high frequencies from the synthetic waveforms. The synthetic waveforms were generated using the mechanism determined by Nabalek, and a trapezoidal time function (0.2, 0.4, 0.2 s) based on his estimate of overall source duration. The synthetics fit very well for this mechanism, and since all four stations for P_{nl} are in a narrow range of azimuth, there seems to be little point in attempting to adjust the mechanism for this dataset.

Table 3.4
Seismic Moment Estimates of the
January 9, 1982 New Brunswick Earthquake

Station	Distance	Azimuth	Moment Ratio
MNT	561 km	255°	Z 0.97 R 1.06
WES	632 km	218°	Z 0.67 R 0.73
OTT	721 km	259°	Z 1.01 R 1.20
SCP	1131 km	236°	Z 1.30 R 1.05

The excellent fit of the records for this event shows that the layer-over-a-halfspace model is adequate for fitting even many of the details of the long-period waveforms. It is unfortunate that only a narrow azimuth range is represented by these stations, and station WES is nearly nodal. However, since the agreement with the data is so good, all stations are included in the moment calculation. The seismic moment determined is 1.3×10^{24} dyne-cm, which is in very good agreement with the body-wave calculation of Nabalek (1984).

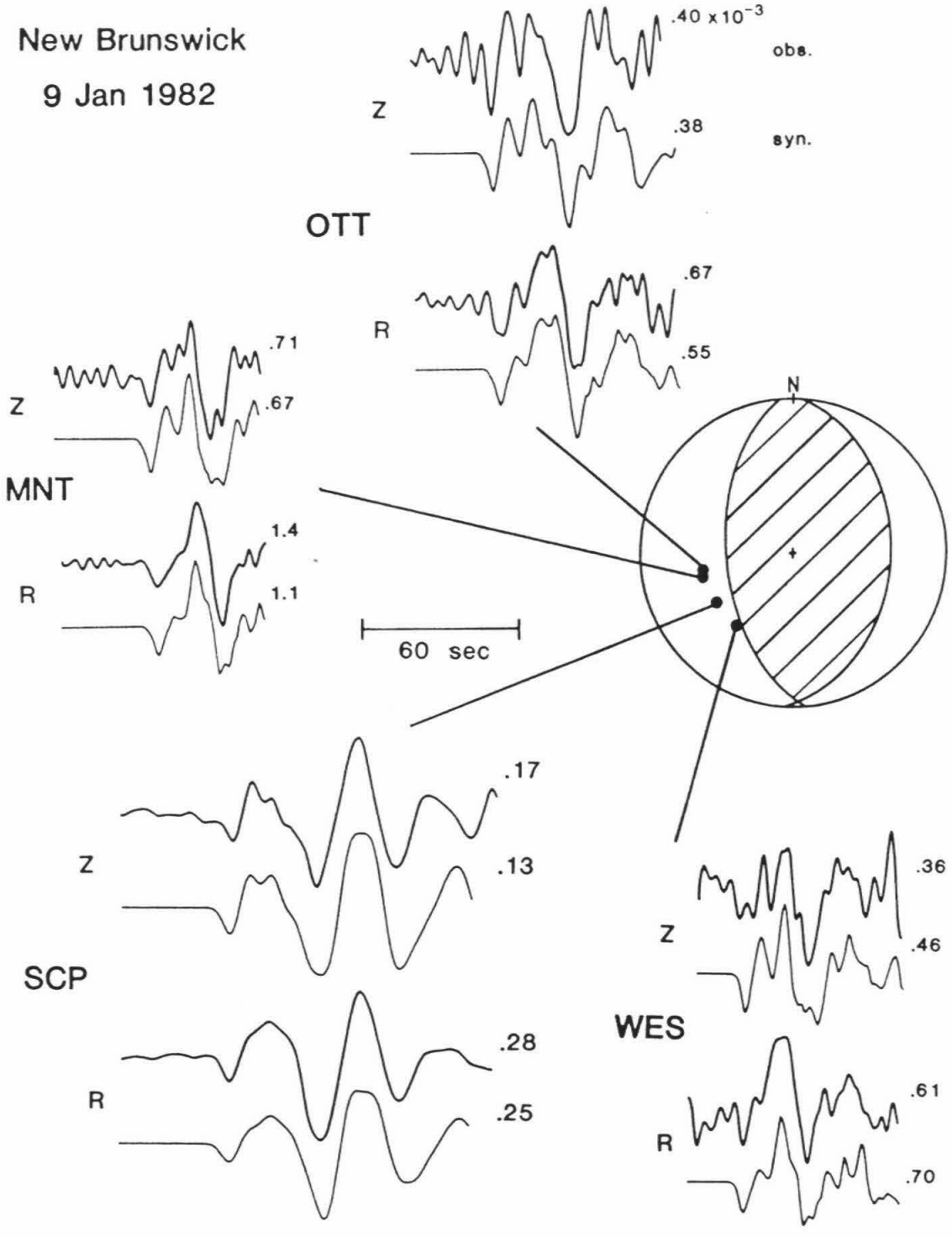

Figure 3.4: Observed and synthetic P_{nl} waveforms for the January 9, 1982 New Brunswick earthquake. Peak-to-peak amplitudes in cm x 10^{-3} are shown. Synthetic amplitudes represent the average moment of 1.3×10^{24} dyne-cm determined from the modeling of these records.

Illinois, 9 November 1968

The central Illinois earthquake of 9 November 1968 was relocated by Stauder and Nuttli (1970), and their location and origin time is given in Table 3.2. They determined a focal depth of 25 km, and m_b=5.5, M_s=5.2. NOAA gives m_b=5.3 and focal depth 18 km. P wave first motions indicate a focal mechanism of strike=195°, dip 45°, and rake 102° (Stauder and Nuttli, 1970). A study of surface-wave spectral amplitudes supports this mechanism and gives M_o=9.0x10^{24} dyne-cm for a focal depth of 22 km (Herrmann, 1979).

Only two stations, listed in Table 3.5, provided usable records of P_{nl} waveforms. Data and synthetic waveforms are shown in Figure 3.5. Convolution with a smoothing filter (1.5 s triangle for OXF, 1.0 s triangle for BLA) has been performed on both data and synthetic waveforms.

Table 3.5

Seismic Moment Estimates of the
November 9, 1968 Illinois Earthquake

Station	Distance	Azimuth	Moment Ratio
OXF	396 km	192°	Z 0.95 R 1.09
BLA	719 km	95°	Z 0.95 R 1.02

This earthquake is the only one for which the mismatch between the model used to construct the Green's functions, and the true structure is significant. First, the source depth of this event is quite a bit deeper than 8 km, the source depth for which responses were calculated. Second, the crust is thicker and faster here, and a mid-crustal

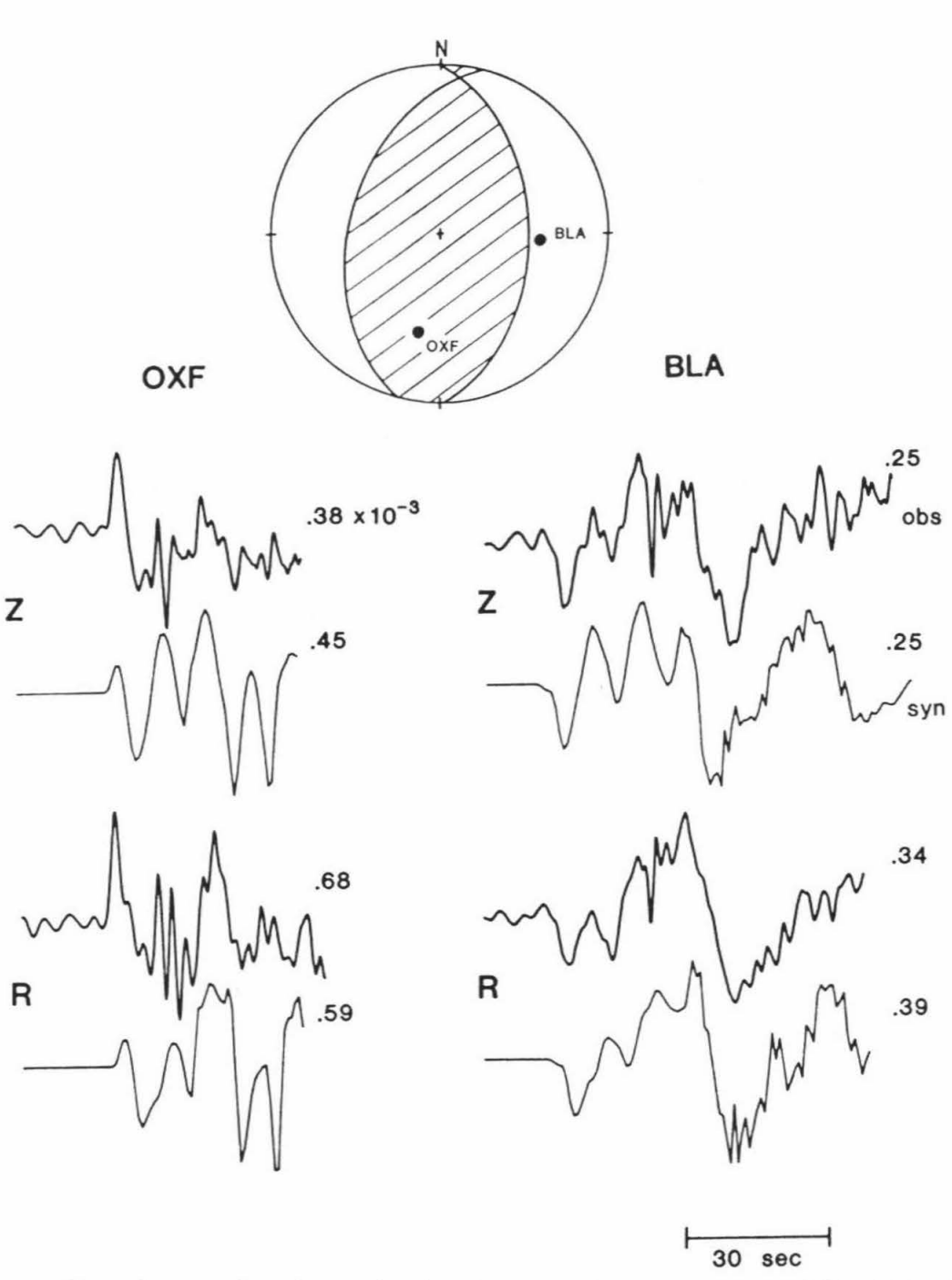

Figure 3.5: Observed and synthetic P_{nl} waveforms for the 1968 Illinois earthquake. Peak-to-peak amplitudes are given in cm x 10^{-3}. Synthetic amplitudes represent the average moment of 1.3 x 10^{24} dyne-cm determined from the modeling of these records.

discontinuity may be significant (Herrmann, 1979; Soller et al., 1982). These effects have been somewhat compensated for by using Green's functions calculated for a larger range (500 km for OXF and 900 km for BLA). A trapezoidal time function (0.2, 0.2, 0.2 s) appropriate for an event of this size is used.

The match of the synthetic seismograms to the data is good for BLA, and somewhat less good for OXF, which is at a smaller distance and is more affected by the variations in structure. The seismic moment obtained is 1.4×10^{24} dyne-cm, which is about 50% greater than the surface-wave estimate of Herrmann (1979).

Kentucky, 27 July 1980

The Sharpsburg, Kentucky earthquake of 27 July 1980 occurred in eastern Kentucky, west of the Appalachian front in an area of low historical seimic activity. NEIS assigned this event a depth of 8 km. A well-constrained, first-motion mechanism presented by Mauk et al. (1982) gives oblique strike-slip movement of strike=42°, dip=50°, and slip=184°. Herrmann et al. (1982) studied surface-wave spectral amplitudes, performing a search for the best-fitting focal mechanism. They found a similar mechanism of strike=30°, dip=60°, and slip=180°, and a depth of 14 to 22 km. The moment calculated from the surface waves varies considerably with depth. Assuming a depth of 18 km, they calculated a seismic moment of 4.1×10^{23} dyne-cm. They also modeled teleseismic short-period body waves, which give a better resolution of depth. This gave a depth of 12 km, and a triangular time function with 0.8 sec rise and 0.2 sec fall.

For P_{nl} modeling, eight stations, listed in Table 3.6, produced

usable, long-period records. Five are WWSSN stations within the eastern US and three are from the Canadian network, with distances ranging from 329 to 1216 km. This event is near the lower limit of seismic moment, which can be modeled using P_{nl}, and the signal-to-noise ration is very small at some stations, as illustrated in Figure 3.6. At most stations, only the vertical component could be used. Radial components were obtained for three stations (BLA, FVM, and LHC).

Table 3.6

Seismic Moment Estimates of the
July 27, 1980 Kentucky Earthquake

Station	Distance	Azimuth	Moment Ratio
BLA	329 km	108°	Z 0.42 R 0.39
FVM	569 km	270°	Z 0.57 R 0.77
GEO	604 km	80°	Z 1.31
SHA	916 km	206°	Z 2.29
OTT	1052 km	38°	Z 1.77+
WES	1167 km	63°	Z 0.93
MNT	1180 km	43°	Z 2.03+
LHC	1216 km	341°	Z 1.28 R 1.05

+ poor-quality station not used in final calulation

Data and synthetic waveforms for this event are presented in Figure 3.7. Both are convolved with a 1.5 s triangle. Considering the noise level of the data, the fit of the synthetic seismograms to the data is in general quite good. Adjustments to the focal mechanism were tried but did not improve the fits, and the mechanism of Herrmann et

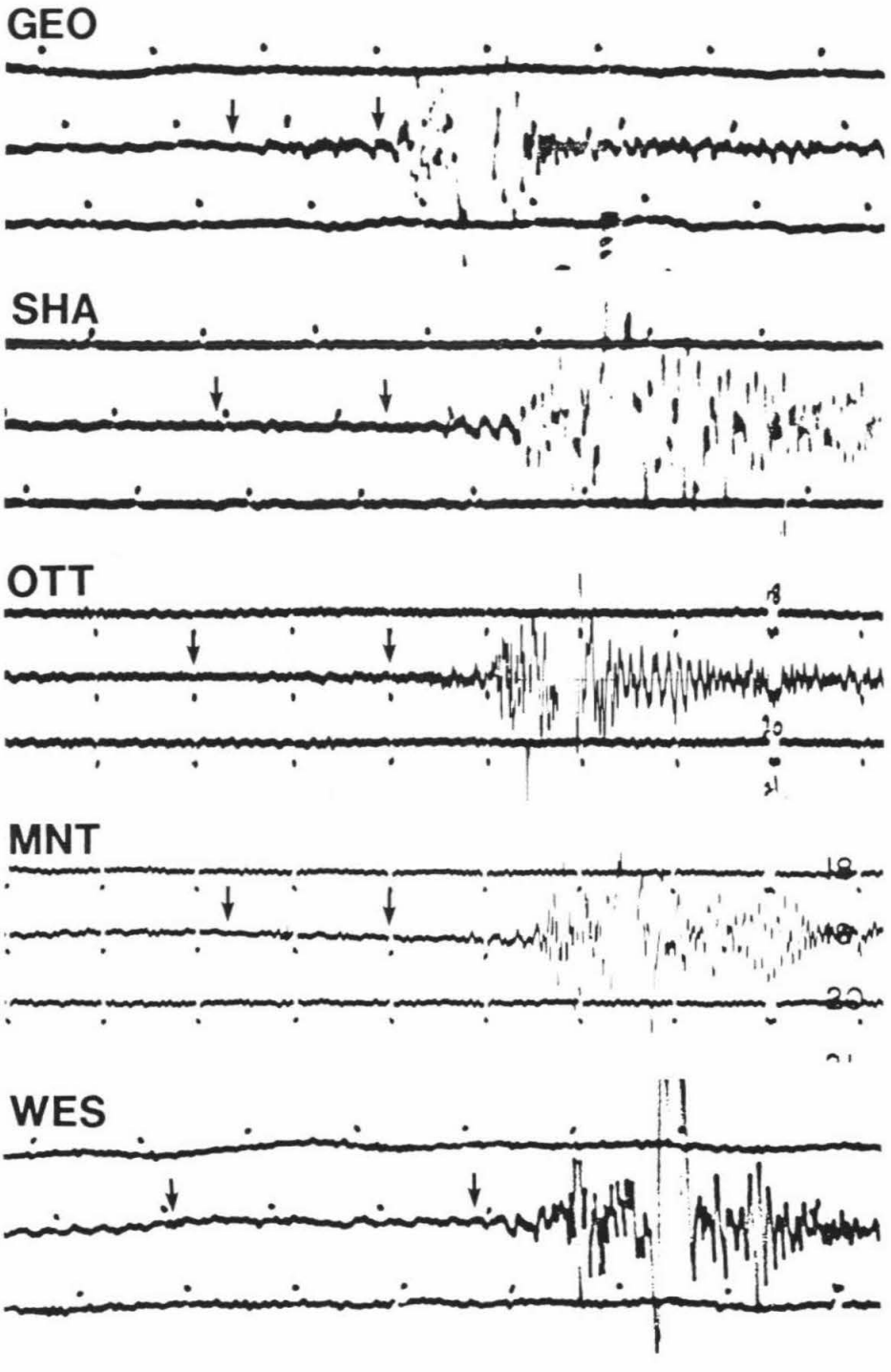

Figure 3.6: Reproduction of the lowest-quality seismograms used in modeling the 1980 Kentucky earthquake. Vertical component is shown. The portion of the record between the arrows is modeled. At m_b=5.2, M_S=4.7, this event is at the lower limit of size for modeling of P_{nl} using WWSSN records.

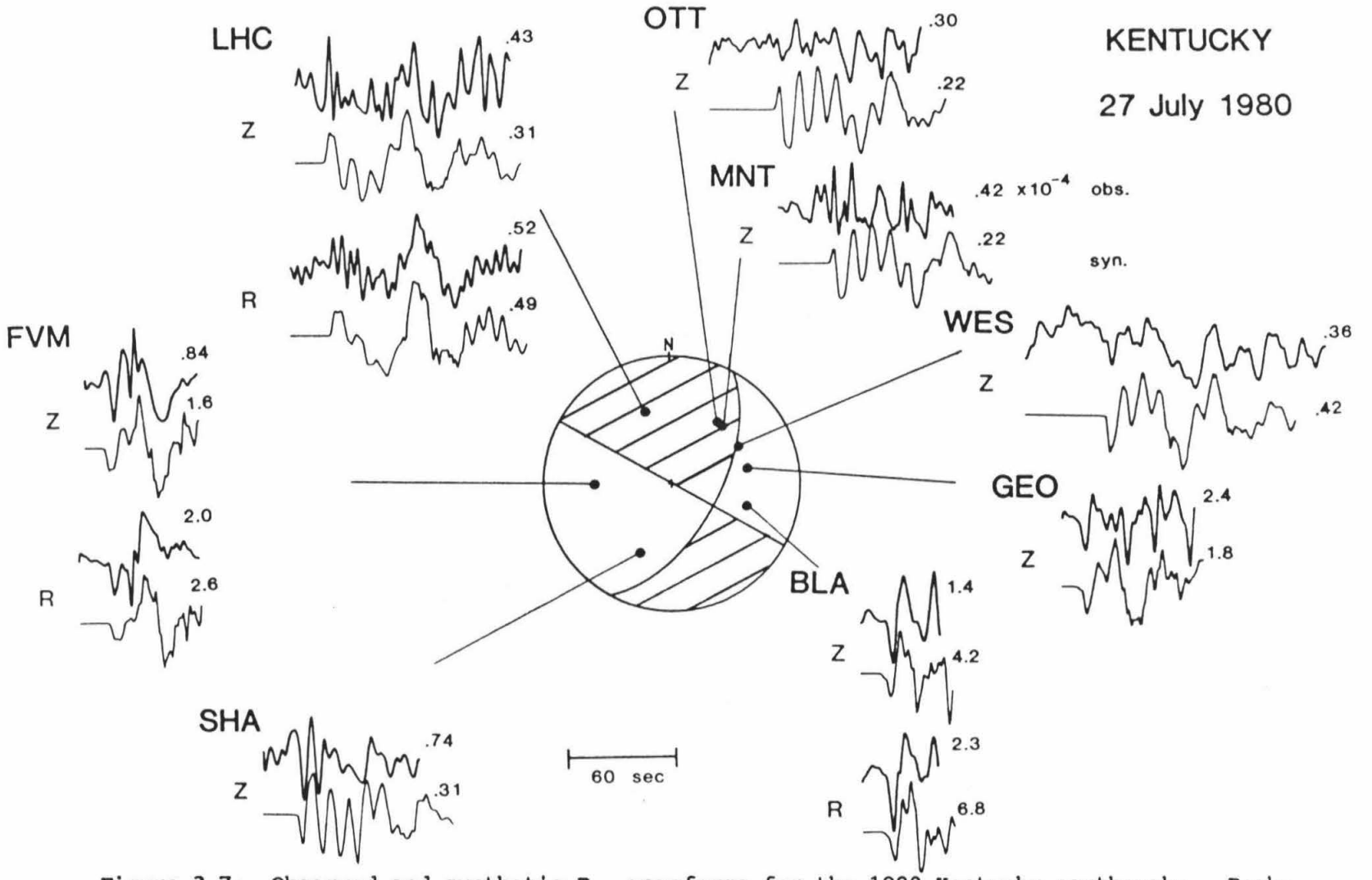

Figure 3.7: Observed and synthetic P_{nl} waveforms for the 1980 Kentucky earthquake. Peak-to-peak amplitudes in cm x 10^{-3} are shown. Synthetic amplitudes represent the average moment of 7.5 x 10^{23} dyne-cm determined from the modeling of these records.

al. (1982) is used. The best fits are at the less distant stations, and at the stations away from the nodes: LHC, FVM, and BLA. Non-linearity of the instrument response may cause the later part of the FVM radial component to be poorly fit. The first two cycles at SHA are well fit but the data do not show the ringing character of the synthetic seismogram. However, the amplitude of this record was very small. Station GEO displays similar behavior in that the overall features of the waveform are matched, but fit in detail is not as good, partly because of the high noise level. The waveform fit is surprisingly good at nodal station WES but less good at near-nodal stations OTT and MNT.

In determination of seismic moment, stations MNT and OTT are not included, since these stations are more distant, near-nodal, and the fit is not satisfactory. Averaging the remaining nine records (three radial and six vertical) gives $M_o=7.5x10^{23}$ dyne-cm, which is approximately twice the surface-wave estimate of Herrmann et al. (1982).

Effects of Lid Structure on P_{nl}

The simplified layer-over-a-halfspace model used in the previous section has proven quite valuable for the study of a large body of data, including the eastern North American events presented here as well as western North American events and those in other continents. The 32 km crust, 6.2/8.2 km/sec model seems a reasonable approximation for many continental areas. However, it is probably not the best model for the shield portions of North America. In addition, at some distance the halfspace mantle model will no longer be adequate. For a

structure such as that proposed in Chapter 2 for the Canadian shield, this distance will be relatively small, as the positive gradient and high velocities create arrivals from within the lid. Previous studies using P_{nl} have generally used the layer-over-a-halfspace model to distances of about 1200 km. To obtain the maximum information from the P_{nl} records, it is important to investigate further how sensitive they are to changes in structure, and to see to what extent the modeling can be improved with more accurate structures. In addition, if it is found that a choice can be made between various structures based on the P_{nl} recordings, this will provide additional information about the shield structure and possible lateral variations within it.

To investigate the effect of structure within the lid, we have taken the layer-over-a-halfspace responses used in the previous section, which were calculated for a mantle P velocity of 8.2 km/s, and added to them the response from an additional boundary, located at a depth of 132 km. This computation is done for four different P wave velocities in the lower layer: 7.9, 8.1, 8.3, and 8.5 km/s. (These velocities are for a flat-layered model; velocities corrected for a spherical earth would be slightly less.) Since the velocity in the middle layer is 8.2 km/s, two models have a higher velocity at depth, approximating the effect of a positive gradient in the lid, and two models have a lower velocity, illustrating the effect of a low-velocity zone. Only rays that have interacted once with this boundary are included in the synthetics. The multiples from this boundary will be small for these distances, because of the relatively small velocity contrast across the boundary.

Responses have been calculated at 100 km intervals for distances

of 200-1400 km, for radial and vertical components of displacement from each of the three fundamental fault orientations. The complete set of these responses is shown in the Appendix. In addition, in the Appendix the responses are shown convolved with a WWSSN long-period instrument. One component, the vertical dip-slip case, will be discussed in detail here, with some mention made of the others.

The responses for the vertical dip-slip component are shown in Figure 3.8. No instrument response has been included, but the responses are convolved with a typical 0.5 s trapzoidal time function (0.5,0.5,0.5 s). The two left columns show the slow models, the middle column shows the responses computed using only the layer-over-a-halfspace, and the two right columns show the fast models. For the fastest model, the change in the initial part of the waveform, caused by arrivals from the high-velocity layer, can be clearly seen by 800 km. By 900 to 1000 km, this arrival dominates the record, and the relative amplitude of the $P_{\underline{nl}}$ (layer-over-a-halfspace) arrivals become neglible compared to the large arrival bottoming within the lid. For a structure such as this, the layer-over-a-halfspce model would not be adequate past about 800 km. The other components of motion (Appendix) are affected somewhat less dramatically, but the change in waveform can be clearly seen at 900 to 1000 km. The relative amplitude of $P_{\underline{nl}}$ is not diminished quite as much, but the lid arrivals are still quite obvious, and dominate the beginning of the record.

For the less extreme velocity structure (8.2/8.3), the effects are not as great. Some change in the beginning of the waveform is seen by 1000 km for this component, with a significant change by 1200 km. By this distance the halfspace model would not provide good results. For

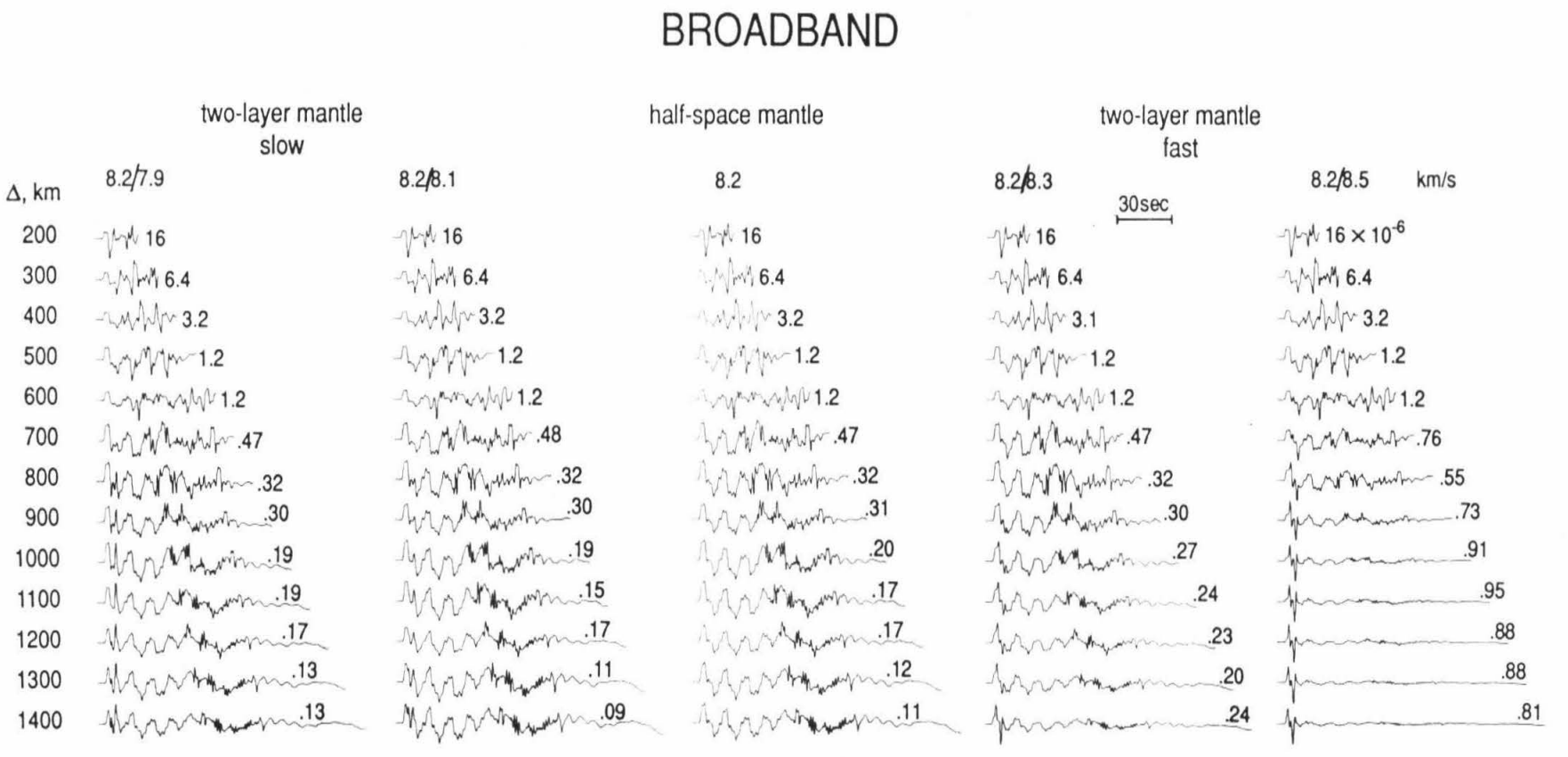

Figure 3.8: Profiles of the vertical displacement, for the pure dip-slip fault orientation. A broadband signal is shown, with no instrument convolution. A typical trapezoidal time history (0.5, 0.5, 0.5 s) has been convolved with the delta function responses. Displacements are shown for five different velocity models: two on the left with a low-velocity zone in the mantle; one in the center with a uniform mantle (half-space model only); and two on the right with a high-velocity layer in the mantle.

the other components (Appendix) little change is seen until 1300 to 1400 km. The overall amplitude of the records is not changed significantly, although the lid arrival can be seen in the beginning of the waveform.

For the case of the low-velocity zone (8.2/7.9 structure), some interference can be seen in the beginning of the waveform at the larger distances. The halfspace model would not fit well in the first few cycles; however, the overall fit would still be quite good, and amplitude estimations would be accurate. Other components (Appendix) are affected even less.

Figure 3.9 shows the same group of responses, the vertical componemt for the pure dip-slip fault, convolved with a long-period WWSSN instrument. The smoothing effect of the instrument response causes some of the effects to be less obvious. For example, for the 8.2/8.3 structure, the change in the initial pulse is not clear until about 1300 km, and the halfspace model provide good fit until this distance.

Figure 3.10 shows the same responses convolved with the much longer-period response of the digital long-period WWSSN instrument. Here only a very subtle change in waveform is seen. For the fastest model, a relatively larger amplitude of the first cycle of the waveform can be seen past about 1000 km. However, overall amplitude does not change much, and calculations done using the halfspace model would be quite adequate.

Figure 3.11 shows the same responses convolved with the short-period WWSSN instrument. Although this simplified structure model will not be adequate to match real short-period records, some interesting

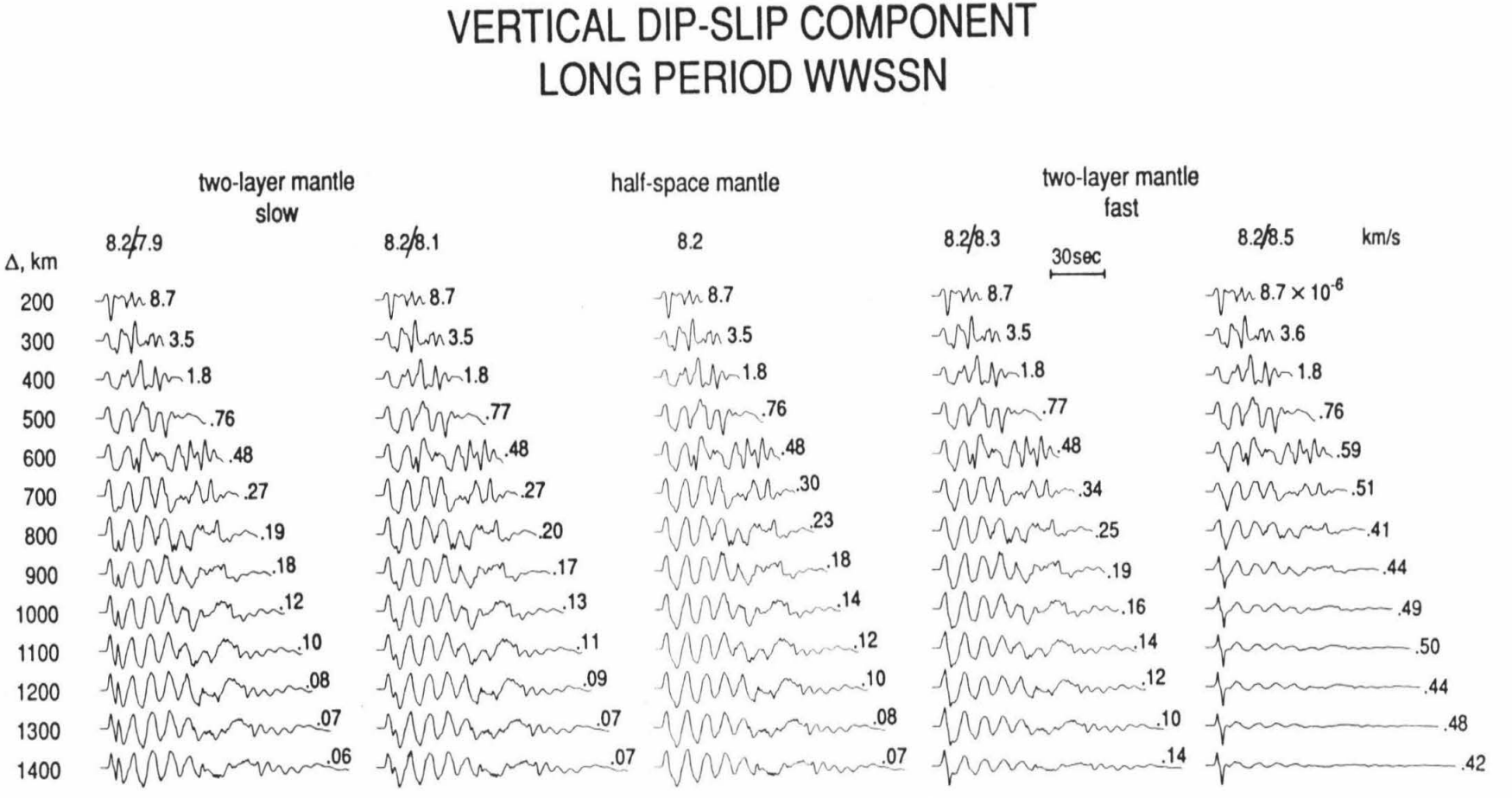

Figure 3.9: The displacements in the Figure 3.8 are shown convolved with the WWSSN long-period instrument response. The numbers above each trace indicate the zero - to - peak amplitude in cm, assuming $M_o = 4\pi\rho_o \times 10^{20}$ dyne cm.

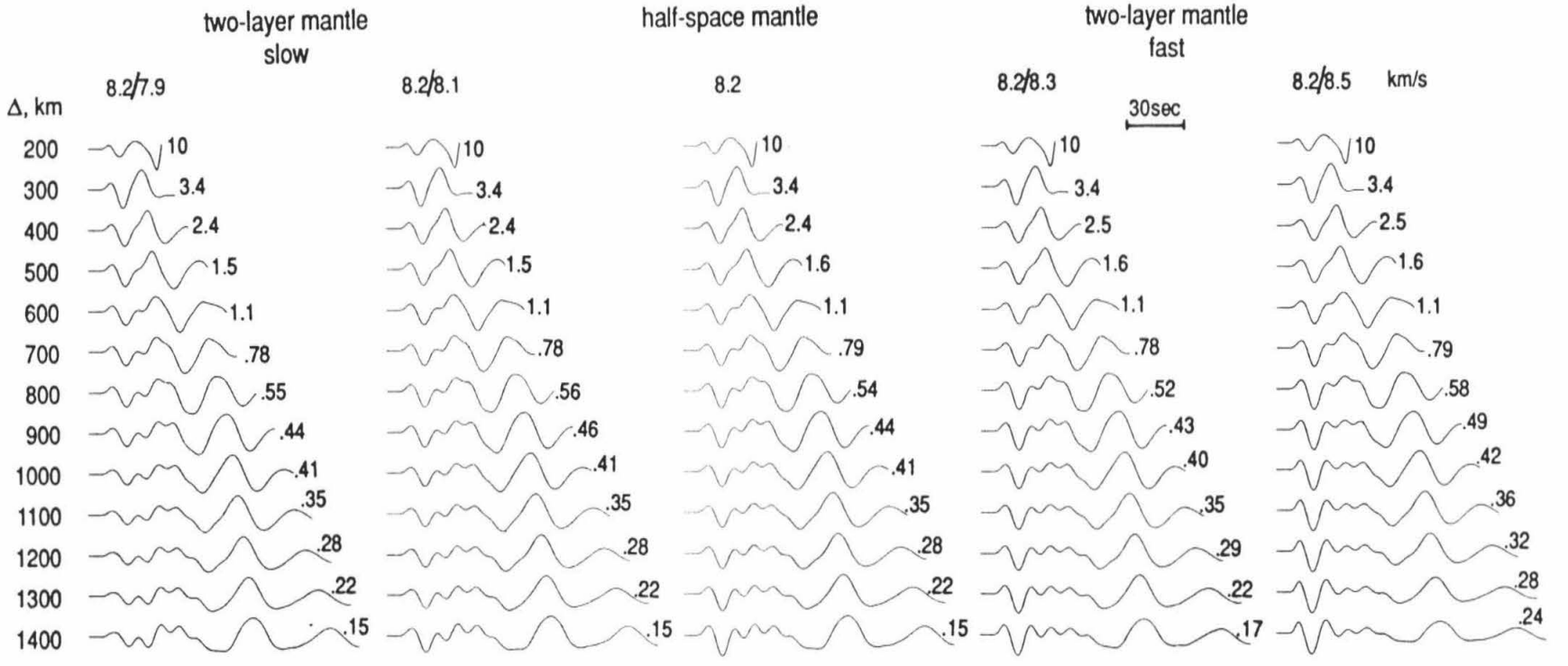

Figure 3.10: The displacements in Figure 3.8 are shown convolved with the digital long-period WWSSN instrument response. The numbers above each trace indicate zero - to - peak amplitude in digital counts, assuming $M_o = 4\pi\rho_o \times 10^{20}$ dyne cm.

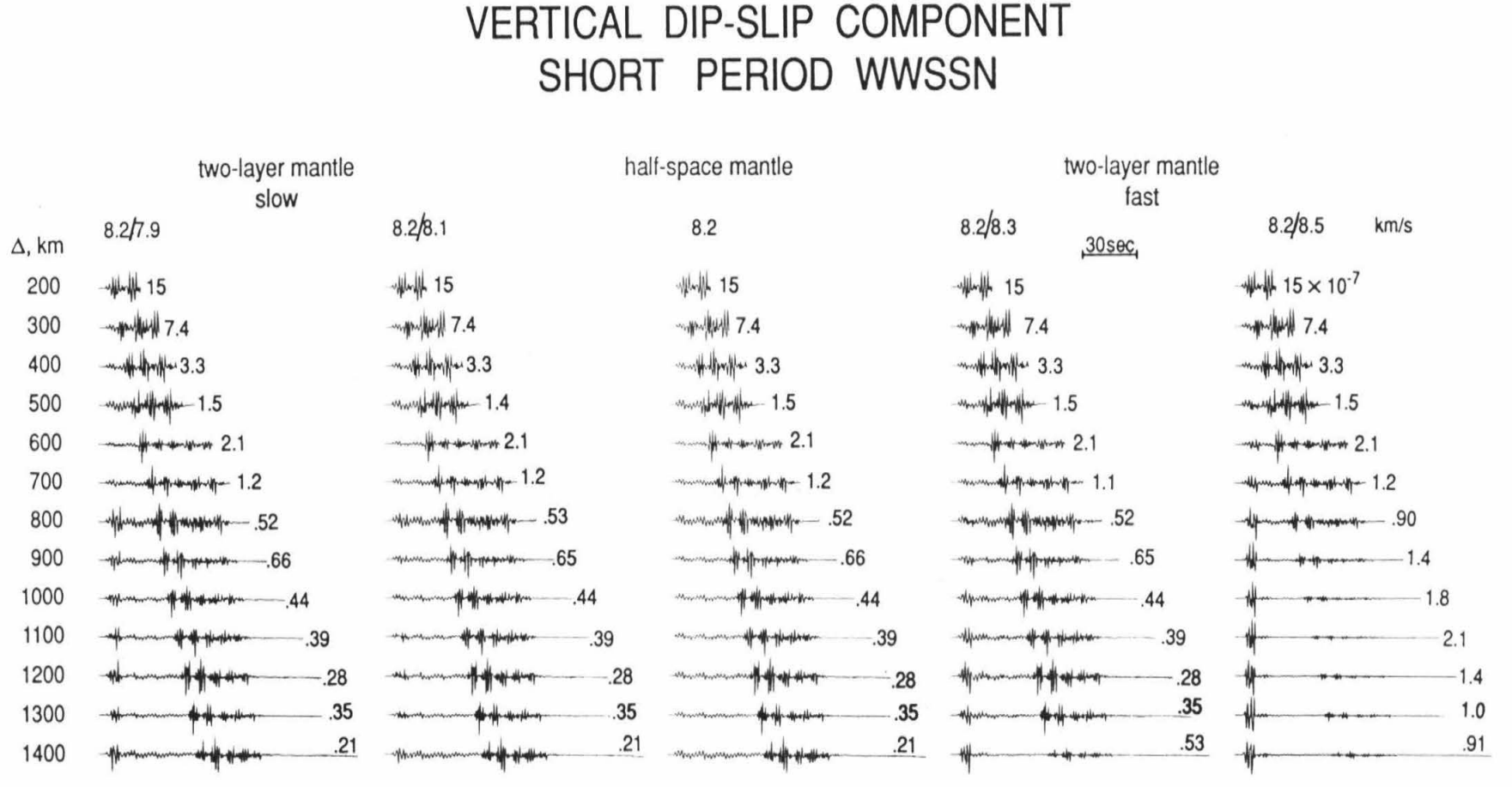

Figure 3.11: The displacements in Figure 3.8 are shown convolved with the short-period WWSSN instrument response. The numbers above each trace indicate the zero - to - peak amplitude in cm, assuming $M_o = 4\pi\rho_o \times 10^{20}$ dyne cm.

points can be made. Comparing the halfspace with the fastest mantle models, the nature of the seismogram changes completely by 800-900 km, with the P_n arrivals dominating the records for the fast case. Records such as these are discussed in more detail by Langston (1982). It is interesting to note that the 8.2/7.9 and 8.2/8.3 records look very much alike, as both models cause increased interference in the beginning of the record.

Examples and Discussion

In this section we will recalculate some of the previously shown P_{nl} seismograms, using the responses for the five lid-structure models. If possible, we would like to obtain more information on lid structure, which might be used to improve the top of the Canadian shield velocity structure model. Unfortunately, we have no records for which the propagation paths are truly within the shield. The records here all have paths skirting the edge of the shield or within the stable central United States. Future incorporation of data from the 1985 Nahanni, 1988 Chicoutimi, and 1989 Ungava Bay earthquakes in Canada will improve this situation somewhat. However, the data presented here may be valuable in showing the lateral extent of the very fast lid proposed for the shield region. In the synthetics presented here, the fastest model, 8.2/8.5 km/s, is most like the lid in S25. The P_n velocity in S25 is faster, so that P_n arrival times calculated from S25 would be earlier.

Figures 3.12 through 3.15 show the P_{nl} records for the Baffin Bay event, calculated for five structure models. In the previous presentation of P_{nl} data, observed and synthetic seismograms were

aligned arbitrarily in time. In this section, records are presented with the same absolute start time, whenever it is known, so that travel-time information can be compared. For each figure, the upper two synthetics are computed for positive gradient lid structure, the middle synthetic is computed using only the layer-over-a-halfspace structure, and the lower two synthetics are computed for the negative gradient lid structure.

Figures 3.12 and 3.13 show stations GDH at 765 km and RES at 802 km. At this distance, the effect of the lid structure is just beginning to show, but makes no significant difference in the synthetics. The P_n velocity of 8.2 km/s fits these stations well. At FBC, 866 km (Figure 3.14), again only a slight change in the synthetics is seen, with the lid arrival beginning to enhance the amplitude of the initial pulse in the case of the positive gradient. The final station for Baffin Bay, ALE, is at a distance of 1273 km (Figure 3.15). At this distance the synthetics vary markedly, with the arrival from within the lid dominating the synthetic for the fastest structure. Unfortunately, none of these models solves the problems with the fit at this station. However, a model with a very high gradient in the lid can clearly be ruled out.

Records from the New Brunswick event are shown in Figures 3.16 and 3.17. Stations MNT, WES, and OTT are at too small a distance to show the effects of the lid structure. The data and synthetics are shown simply to provide a check on travel time (Figure 3.16). The 8.2 km/s P_n velocity fits well here. The record from SCP, 1131 km, is shown in Figure 3.17. This record is from the digital long-period WWSSN instrument. For this long-period response, the change in waveform is

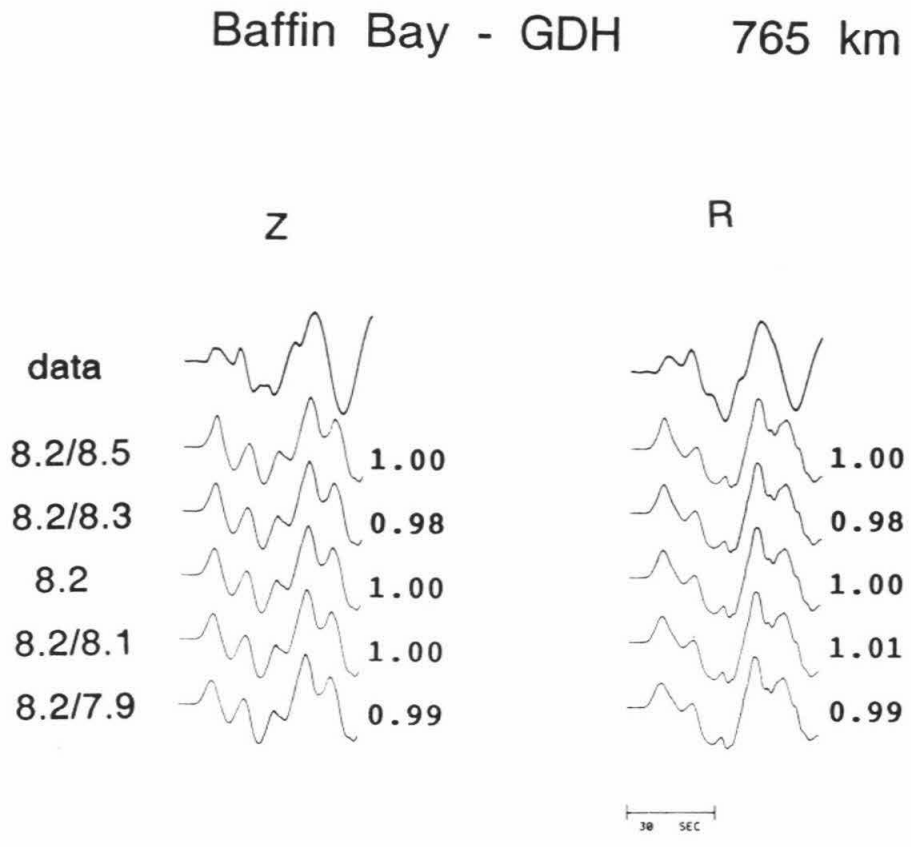

Figure 3.12: Vertical and radial records are shown for the Baffin Bay event at station GDH. Start time is the same for each trace. The upper trace is the data; below are synthetics computed for the five lid structure models. Zero-to-peak amplitudes are given relative to the halfspace model. At this distance and azimuth there is little difference in the synthetics.

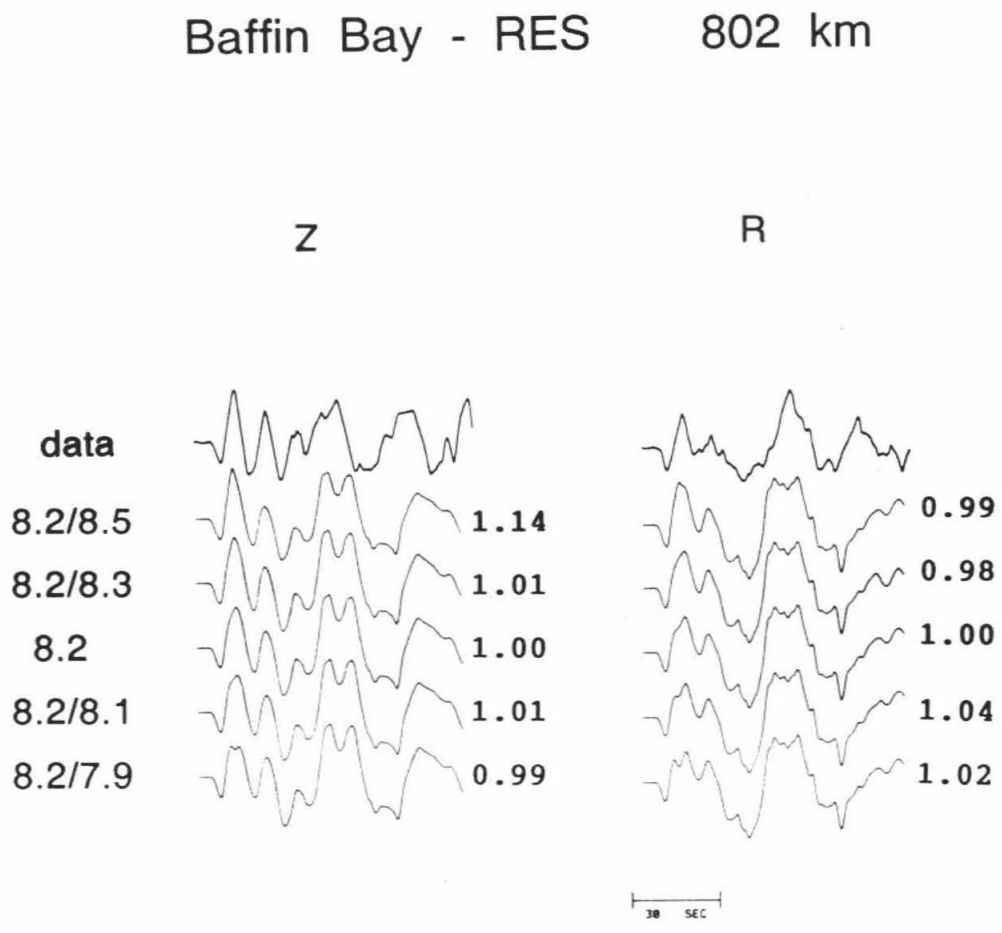

Figure 3.13: Vertical and radial data and synthetics for the Baffin Bay event at station RES, aligned at the same start time. The timing is fit well. Both these synthetics and those for GDH in the previous figure were computed using the Green's functions at 800 km. However, for this azimuth a slight change in the initial pulse can be seen in the synthetics.

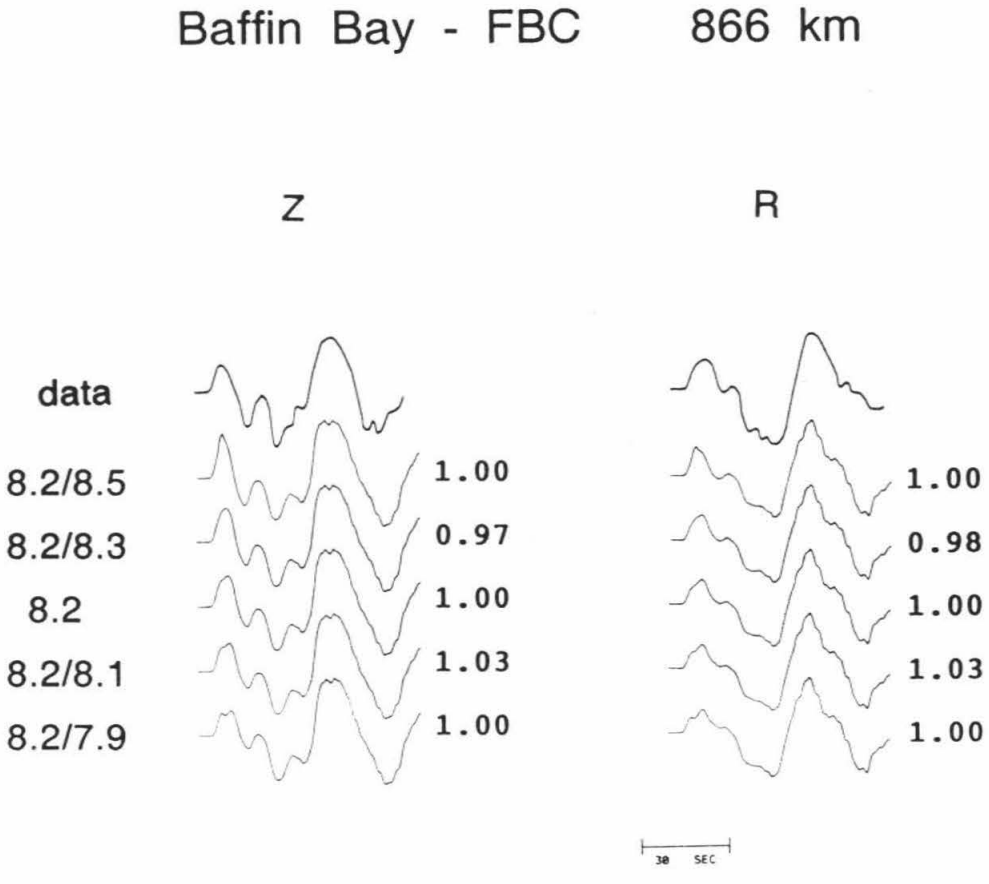

Figure 3.14: Data and synthetics for the Baffin Bay event at station FBC. The clock was not functioning at this station, so the data are aligned arbitrarily in time.

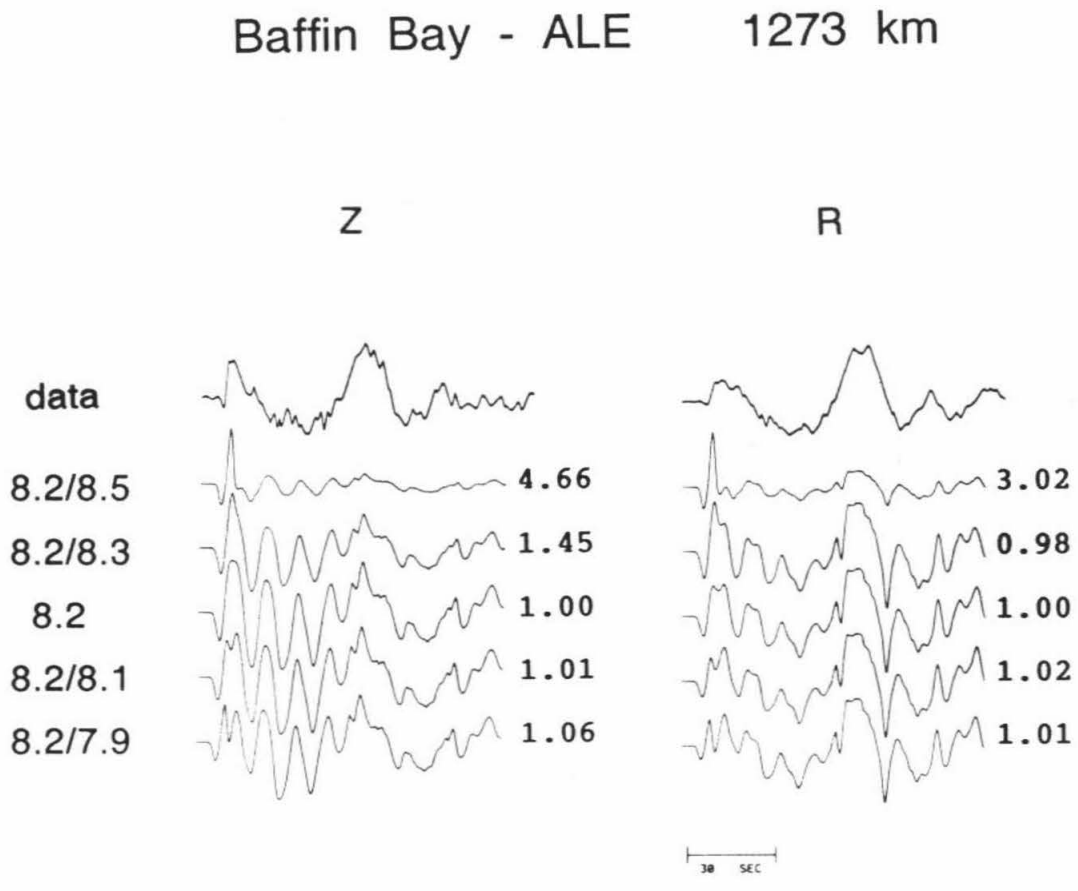

Figure 3.15: Data and synthetics for the Baffin Bay event at station ALE, aligned at the same start time. The initial pulse in the data is slightly late relative to the models. At this distance there is a dramatic difference in the synthetics. The data do not fit well with any of these models, but the fastest lid model can be ruled out.

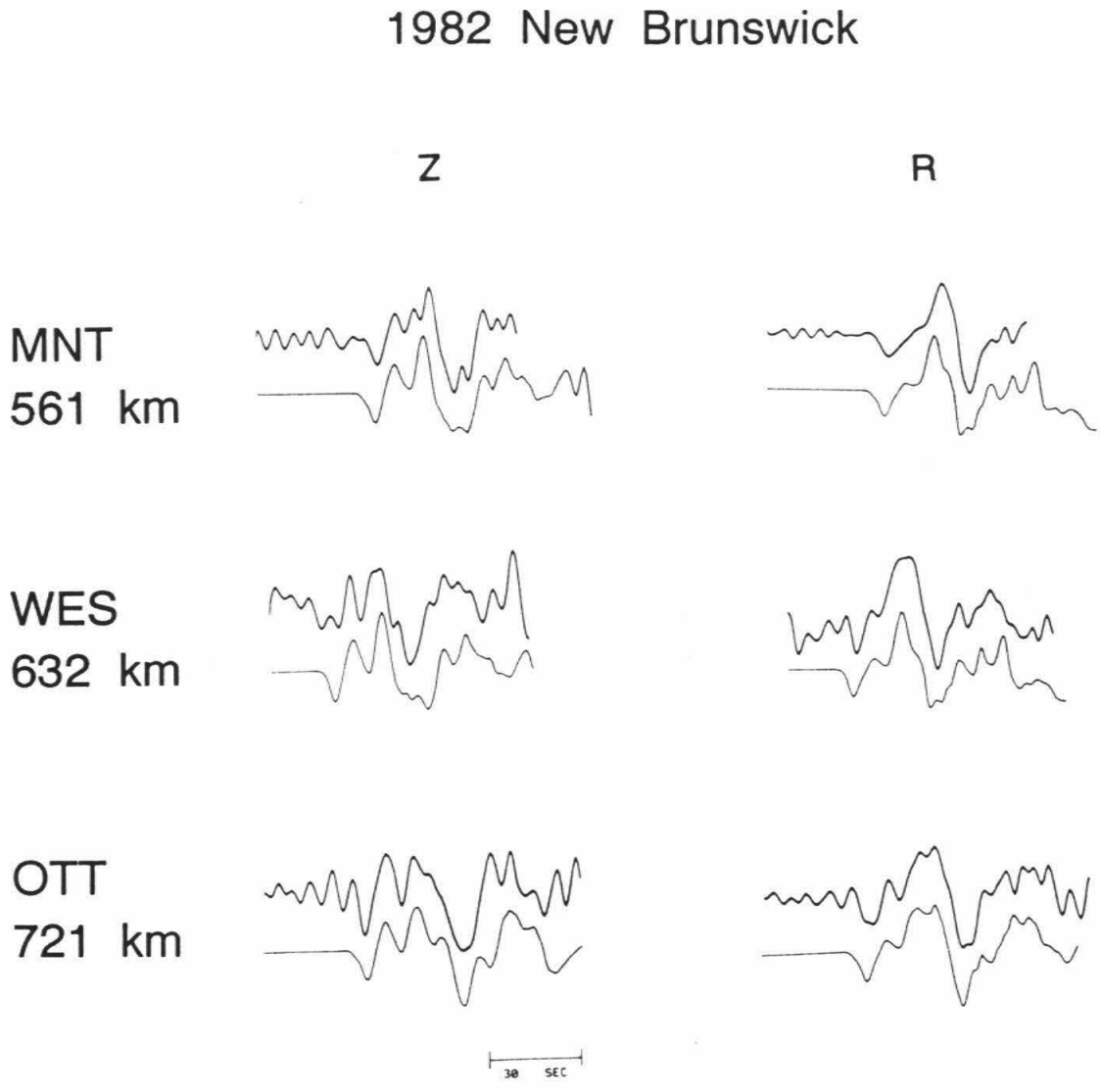

Figure 3.16: Data and synthetics for the New Brunswick event, aligned at the same start time. At these distances the various lid models produce essentially identical synthetics, so only one is shown. For these paths, the absolute timing is matched well by the 8.2 km/sec P_n velocity.

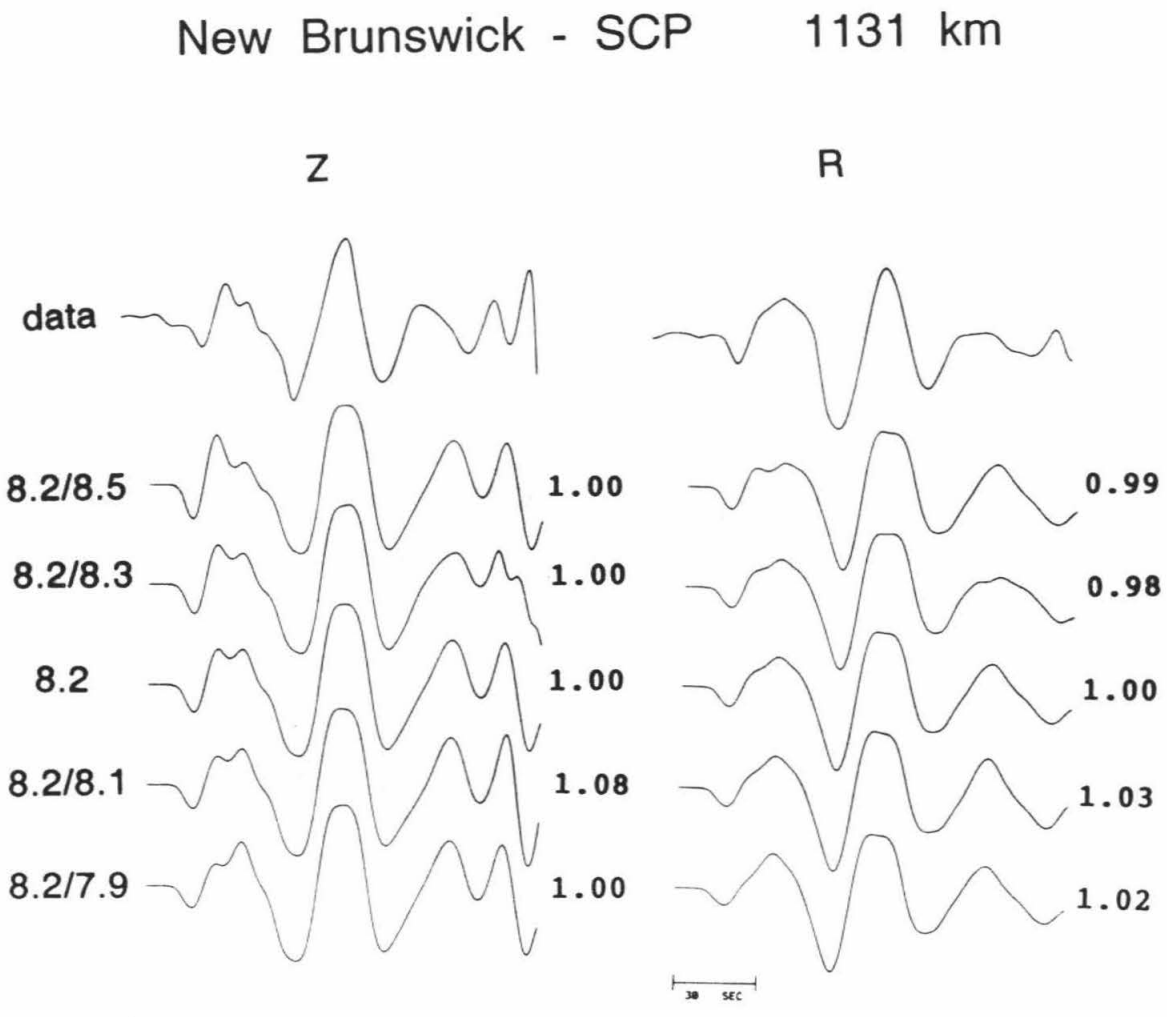

Figure 3.17: Data and synthetics for the New Brunswick event recorded on the digital long-period WWSSN instrument at SCP. Timing is not absolute, becuase of difficulties in reading the tape header. The arrivals from within the lid cause a clear difference in the initial pulse of the synthetics. The vertical data match the fastest lid structure. The changes in the radial case are less pronounced, but the fastest model does not seem to provide the best fit.

subtle but can nevertheless be seen clearly in the initial pulse. For the vertical record, the best fit is provided by the fastest (8.2/8.5) model. For the radial record, the 8.2/8.3 or halfspace model would probably be chosen.

Figures 3.18, 3.19 and 3.20 show records from the Kentucky event. One of the better stations was LHC, at 1216 km (Figure 3.18). For the vertical record, the first arrival time in the data is clearly earlier than that for these models. The arrival time in the radial record is less clear. The best fit is provided by one of the fast lid models. The high-frequency initial pulse suggests the fastest model, but the relative amplitude of the PL portion of the record is then a little too small.

Figure 3.19 shows data and synthetics for SHA, 916 km. The data are early relative to the synthetics. The best waveform fit is clearly provided by the fastest model, where the arrival from the lid enhances the first pulse, and the seismogram does not then have the ringing character that is not seen in the data. However, it must be remembered that the data quality is quite poor at this station. Looking at the amplitudes of the synthetics, it can be seen that a significant misestimation of moment would be possible here, if the appropriate model is not known.

Figure 3.20 shows stations WES and MNT. For these stations the data quality was very poor, and the only real conclusion that can be drawn is that the data are early relative to the synthetics. Again, the synthetic amplitudes illustrate that seismic moment could easily be misestimated.

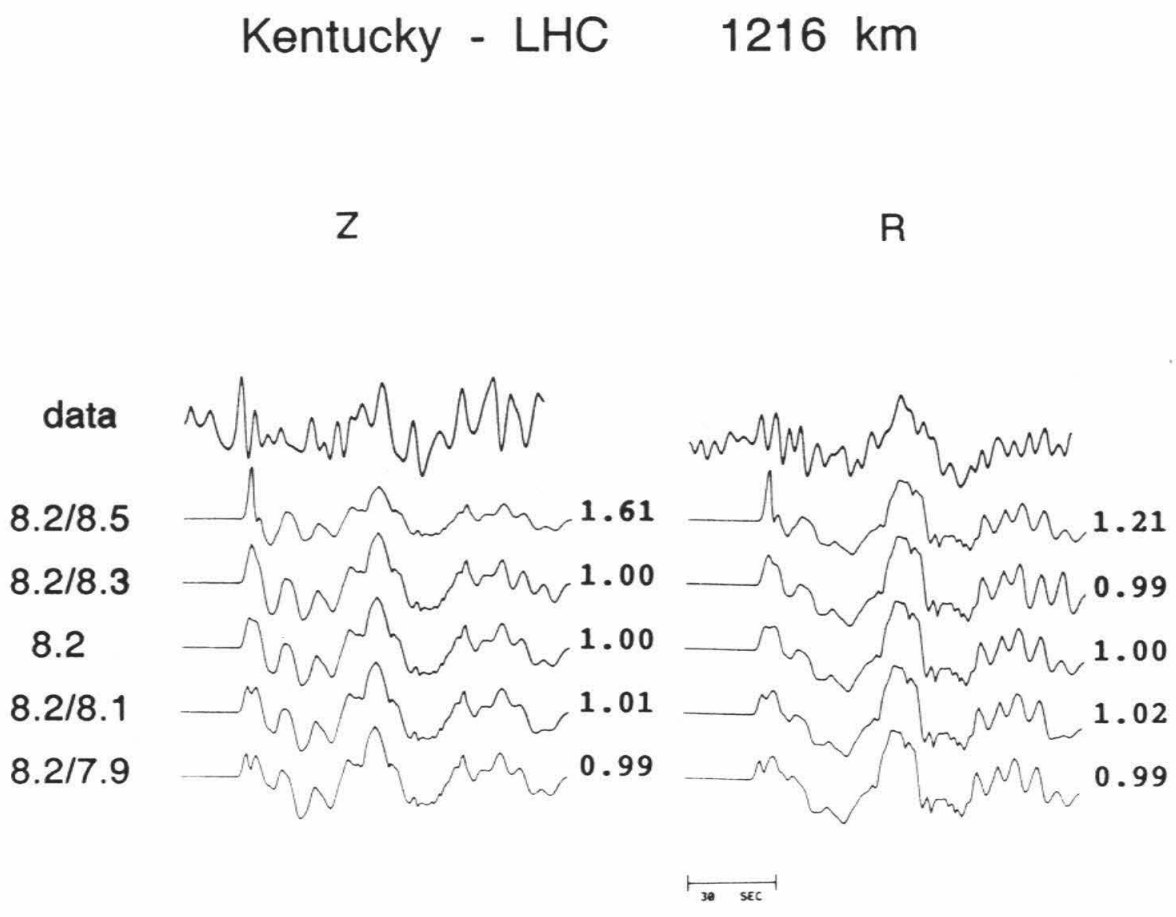

Figure 3.18: Data and synthetics for the Kentucky event at station LHC, at which the data quality was relatively good. Zero-to-peak amplitudes are given relative to the halfspace model. Data and synthetics are shown with the same start time, and the first arrival in the data is early relative to that predicted by the models. The large initial pulse in the vertical record seems to support a fast lid structure, although the radial case is less clear.

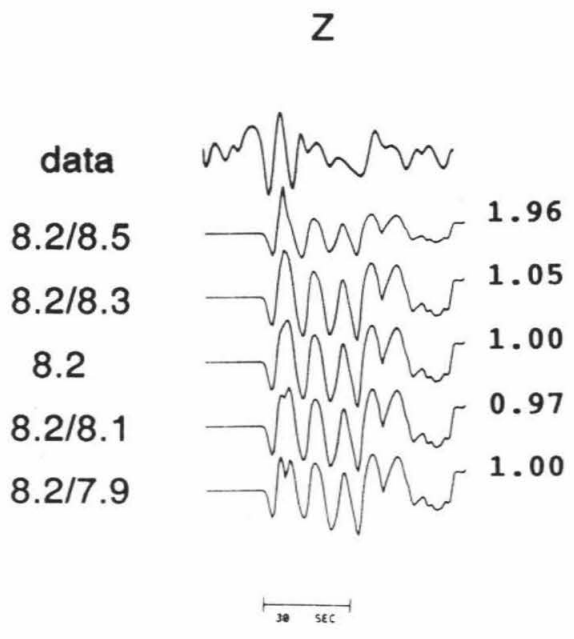

Figure 3.19: Data and synthetics for the Kentucky event at station SHA, vertical component only, aligned on absolute time. The data quality at this station was poor, and this record should not be over-interpreted. However, the first swings of the data are early by over a second relative to the synthetics, and the waveform fit is best for the fast model.

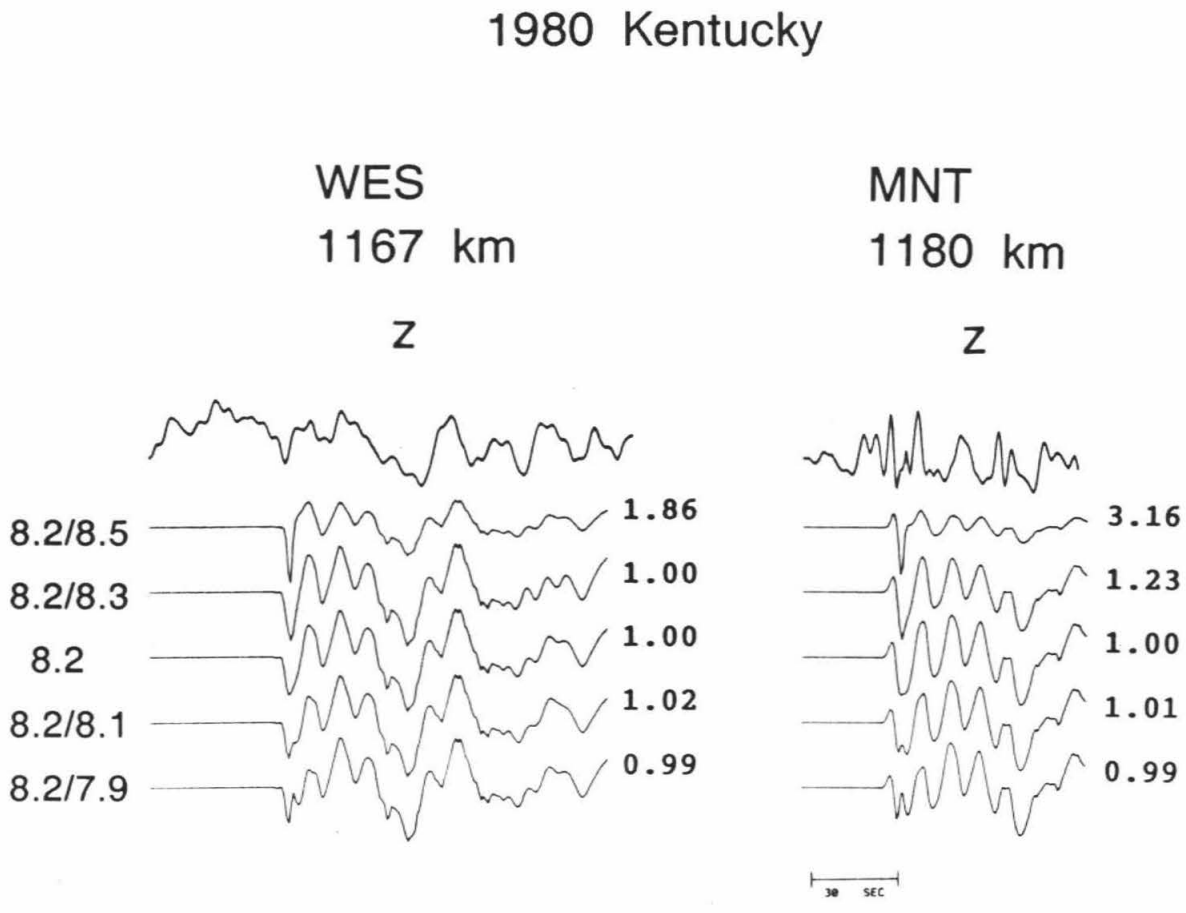

Figure 3.20: Data and synthetics for the Kentucky event at stations WES and MNT, vertical component only, aligned on absolute time. The data quality at these stations is poor and these records should not be overinterpreted. For both of these stations the first pulse in the data is early by more than a second relative to the synthetics. The synthetics provide a good example of the large-amplitude, high-frequency initial arrival from within the lid and the relative suppression of the long-period part of the waveform for the fast lid model. With poor-quality data at these distances, some miscalculation of moment is possible if the appropriate model is not known.

Conclusions

Modeling of P_{nl} shows lateral variations in lid structure. In general, paths within the stable central United States support a faster structure, and paths in the non-shield regions of eastern North America a somewhat slower structure. The dataset presented here is sparse, but future inclusion of data from the more recent Canadian earthquakes will improve this. With more data, P_{nl} modeling should prove useful in investigating lithosphere structure, possibly improving on the simple linear gradient used in S25, and determining over what region this structure is appropriate.

Accurate modeling of P_{nl} requires that an appropriate lid structure be included, for distances as little as 800 km, in regions with a thick lid and a significant gradient in lid velocity, such as the Canadian shield. This will be particularly important as more broadband recordings become available. Events too small to be well recorded by WWSSN long periods may make good broadband recordings, which are more sensitive to structural variatons.

Appendix

The following twelve figures present profiles of P_{nl} displacements, for movement on each of three fundamental fault types, for each of five lid velocity models. The first six figures show a broadband signal, with no instrument response convolution. The second six figures show the displacements convolved with the long-period WWSSN instrument response. For each group of figures, the first three show the radial displacements, and the next three show the vertical displacements. For all figures, a typical trapezoidal time history (0.5, 0.5, 0.5 s) has been convolved with the delta function responses. The numbers above each trace indicate the zero-to-peak amplitude in cm assuming $M_o = 4\pi\rho_o \times 10^{20}$ dyne-cm.

The middle profile in each figure is for a simple, layer-over-a-halfspace model (32 km thick crust with V_p=6.2 km/s, halfspace mantle V_p=8.2 km/s). For the other profiles, an additional boundary is added at a depth of 132 km. The velocity below this boundary is 7.9, 8.1, 8.3 or 8.5 km/s. Velocities of 7.9 and 8.1 km/s create a negative lid gradient, and these profiles are shown on the left of each figure. Velocities of 8.3 and 8.5 km/s create a positive lid gradient, and are shown on the right.

These figures should provide a useful reference for comparison with observed P_{nl} records.

RADIAL STRIKE-SLIP COMPONENT
BROADBAND

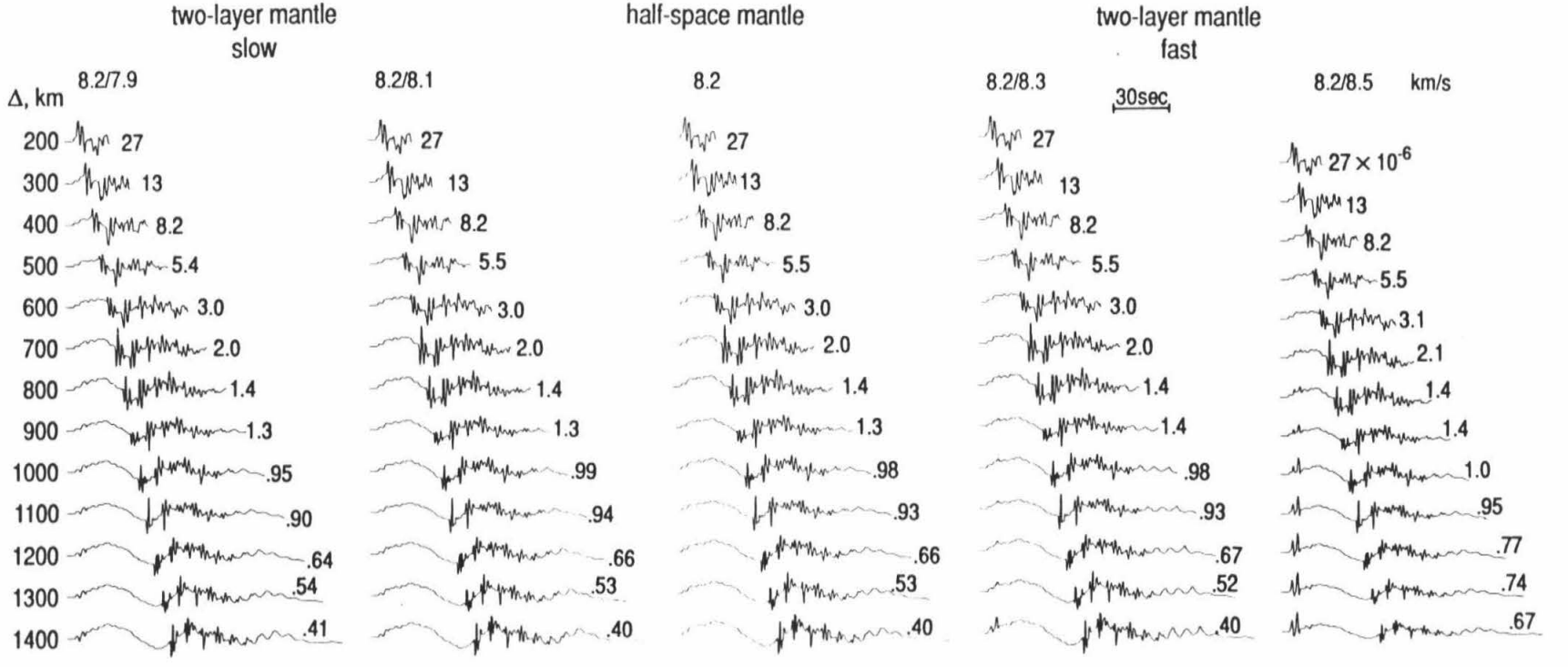

RADIAL DIP-SLIP COMPONENT
BROADBAND

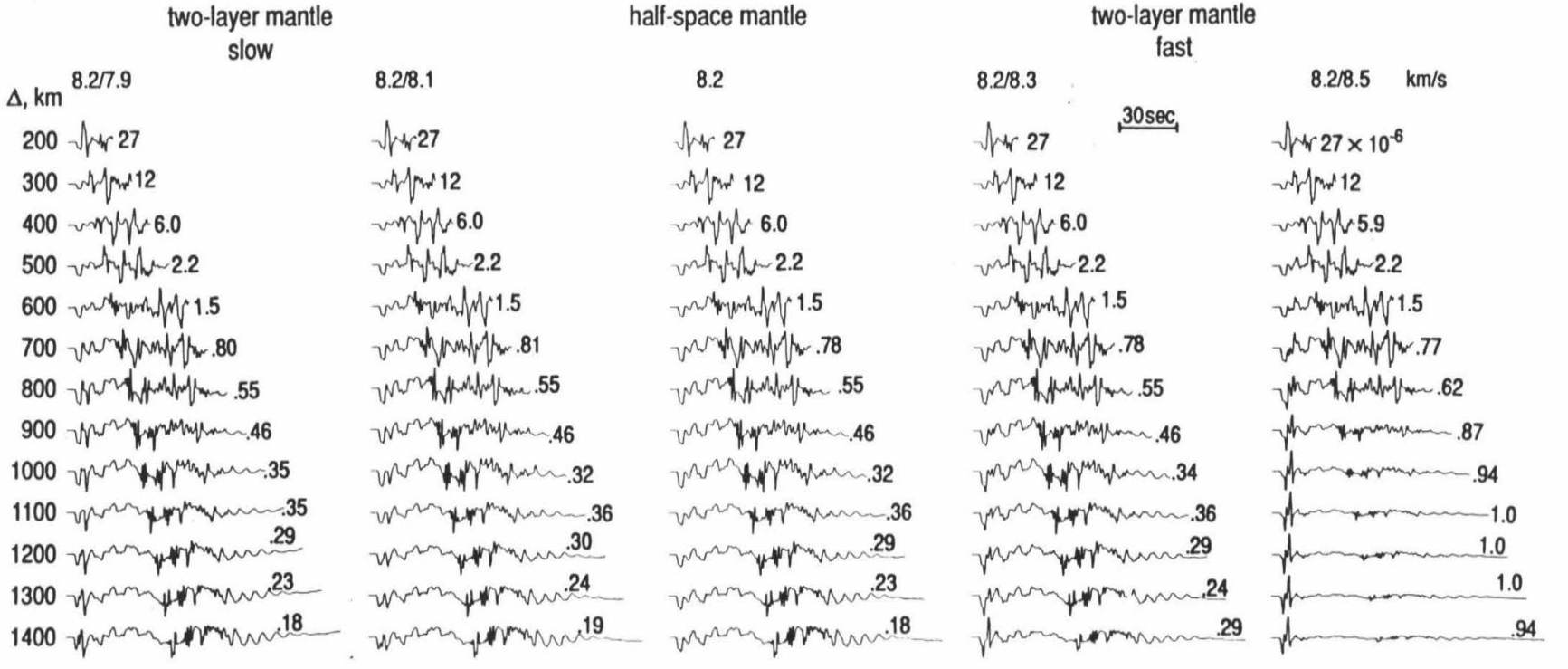

RADIAL 45°-DIP-SLIP COMPONENT
BROADBAND

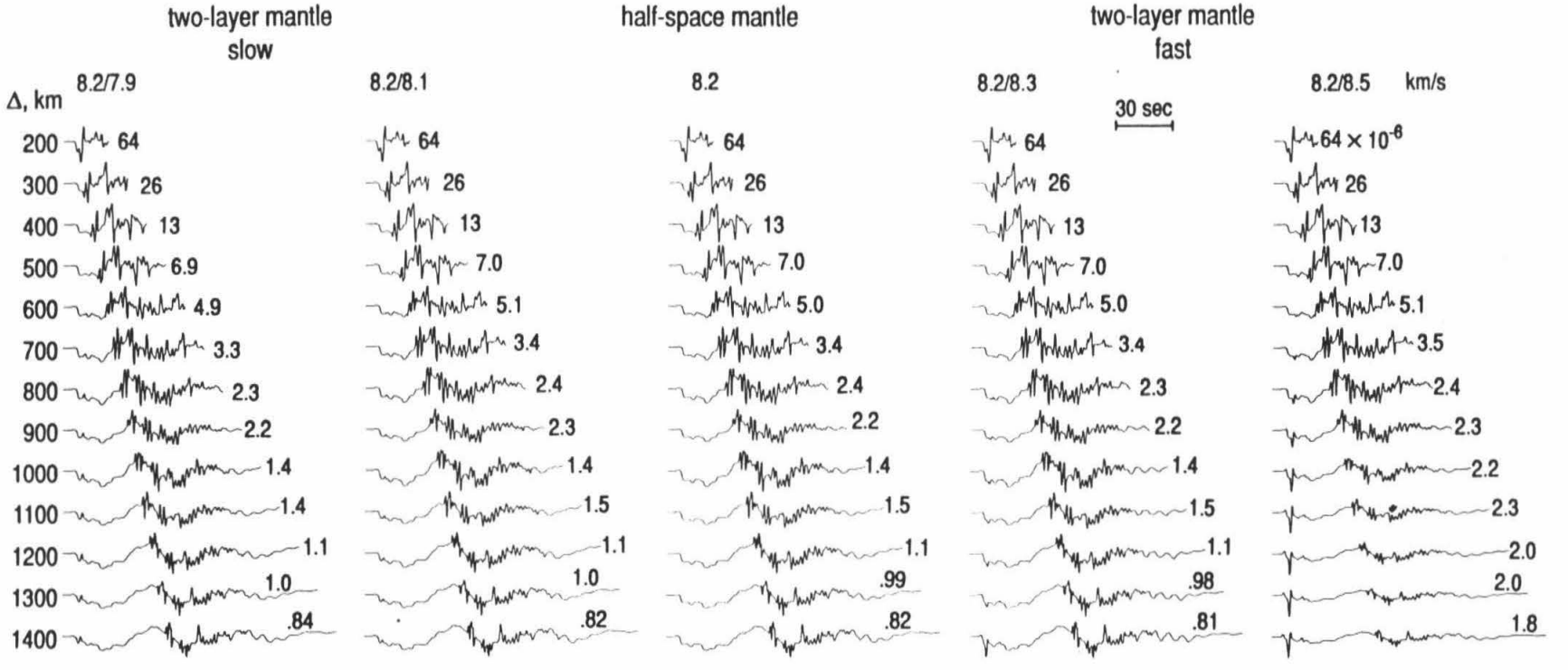

VERTICAL STRIKE-SLIP COMPONENT
BROADBAND

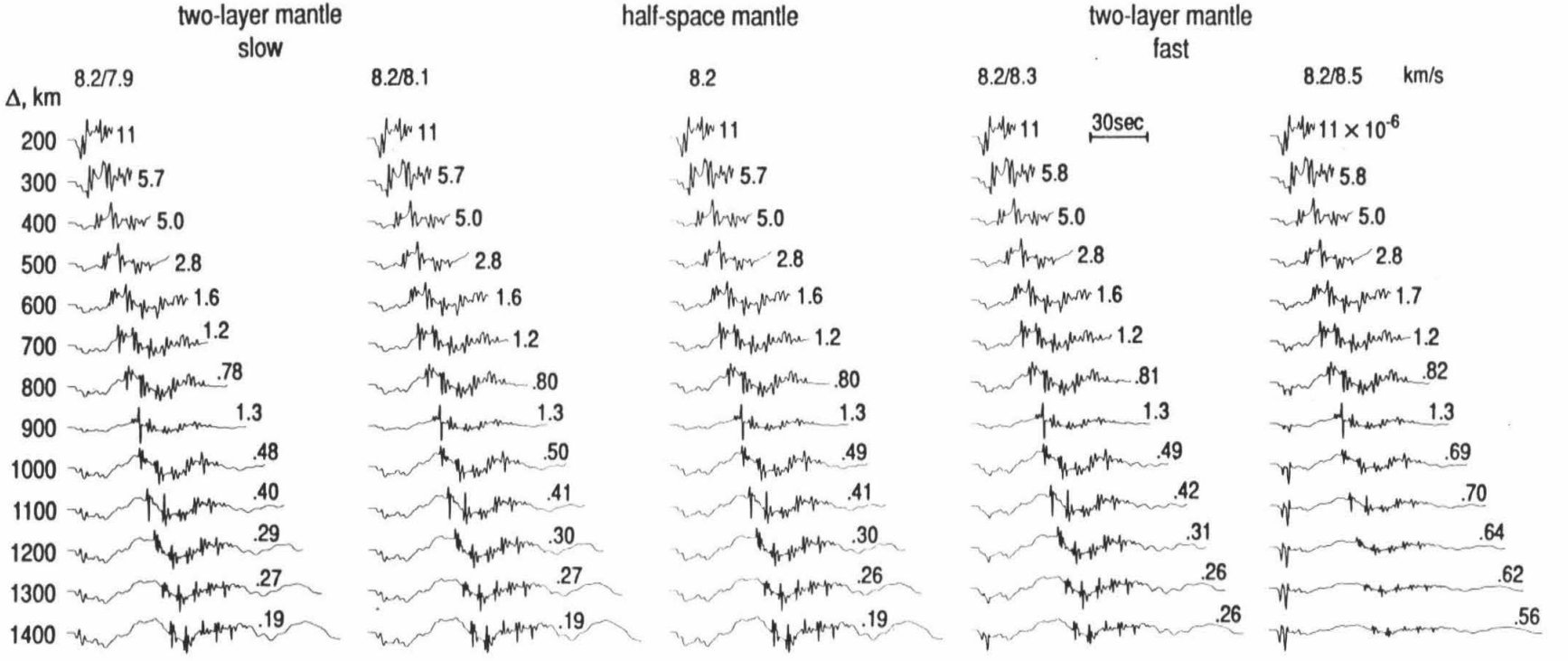

VERTICAL DIP-SLIP COMPONENT
BROADBAND

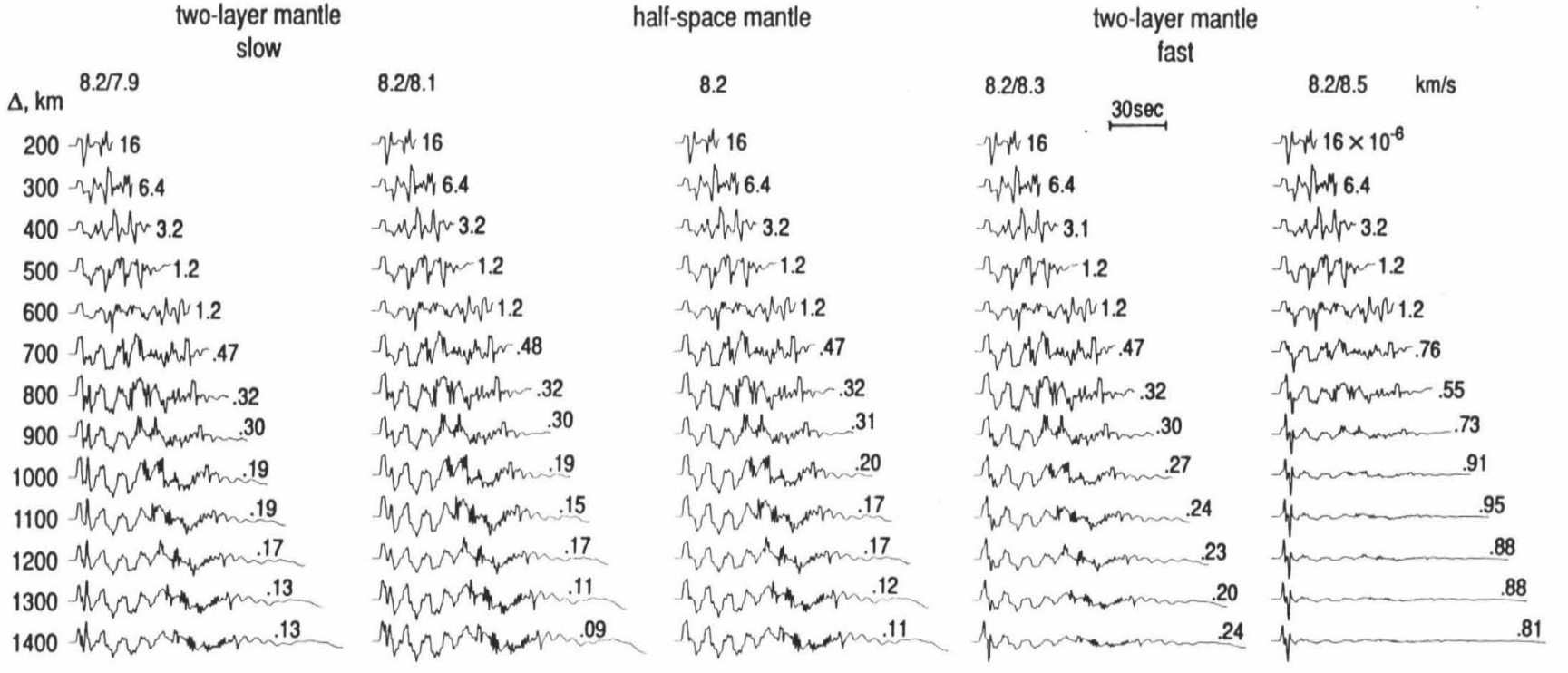

VERTICAL 45°-DIP-SLIP COMPONENT
BROADBAND

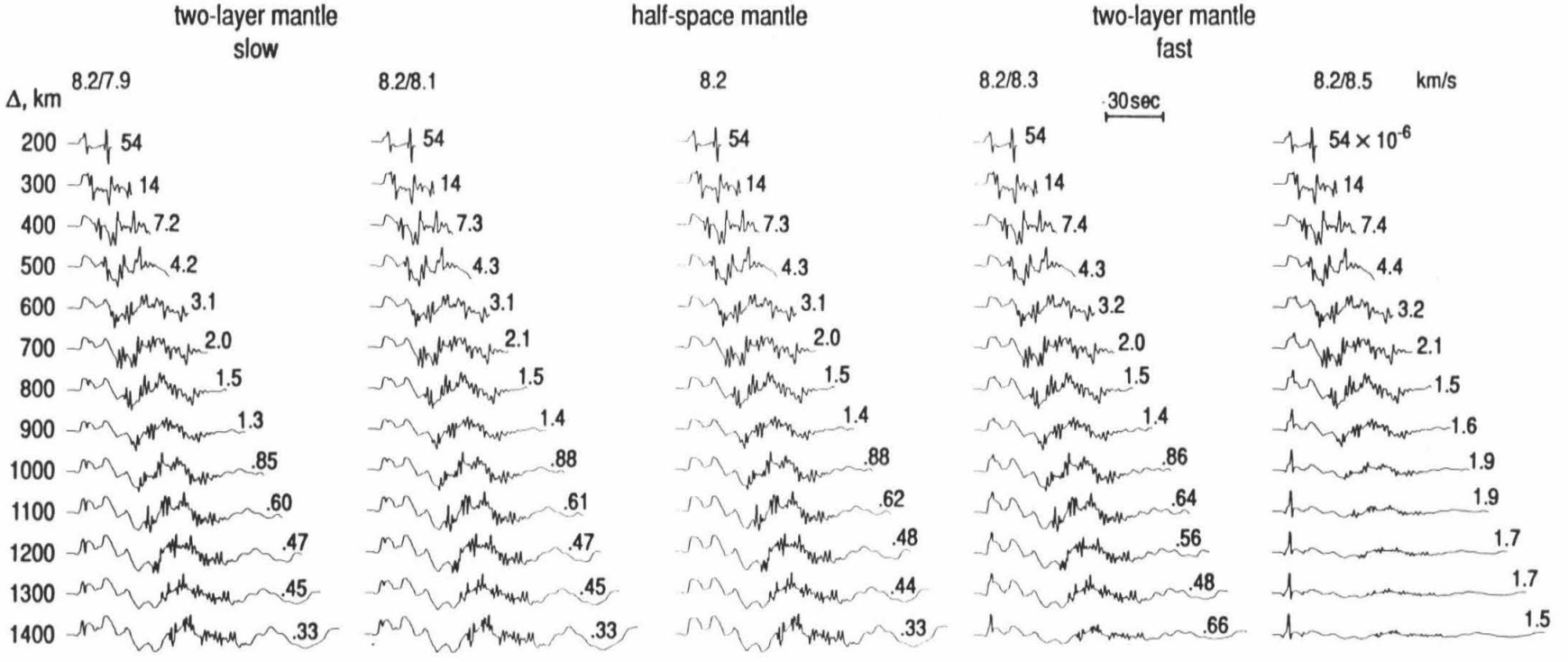

RADIAL STRIKE-SLIP COMPONENT
LONG PERIOD WWSSN

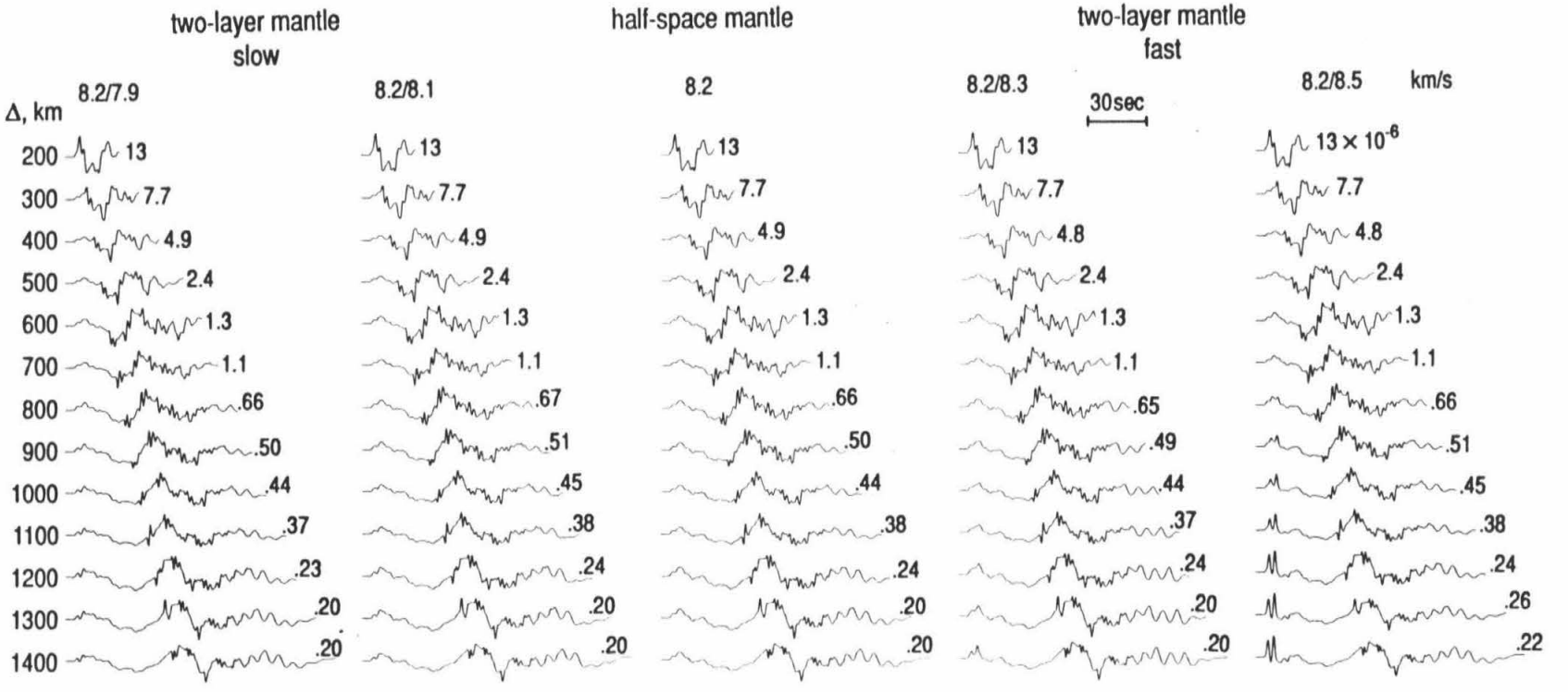

RADIAL DIP-SLIP COMPONENT
LONG PERIOD WWSSN

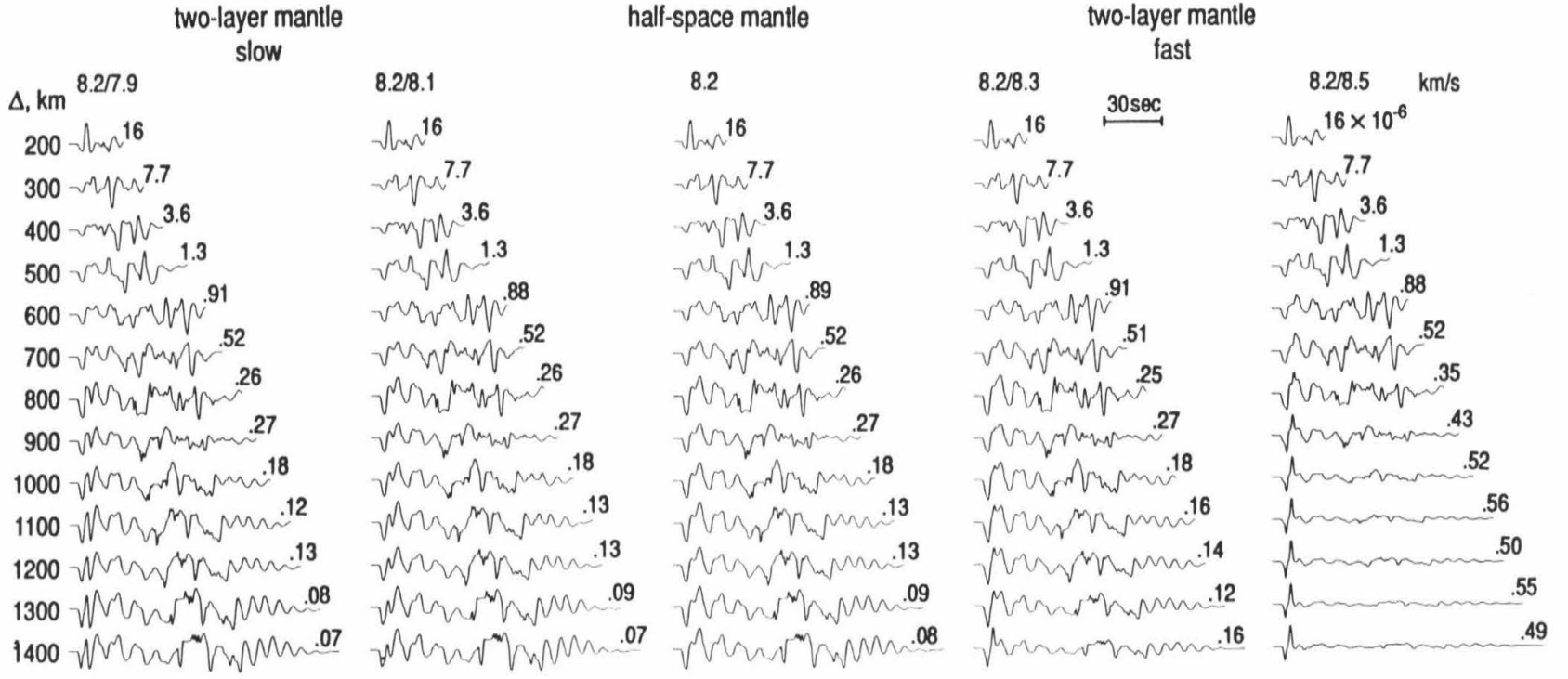

RADIAL 45°-DIP-SLIP COMPONENT
LONG PERIOD WWSSN

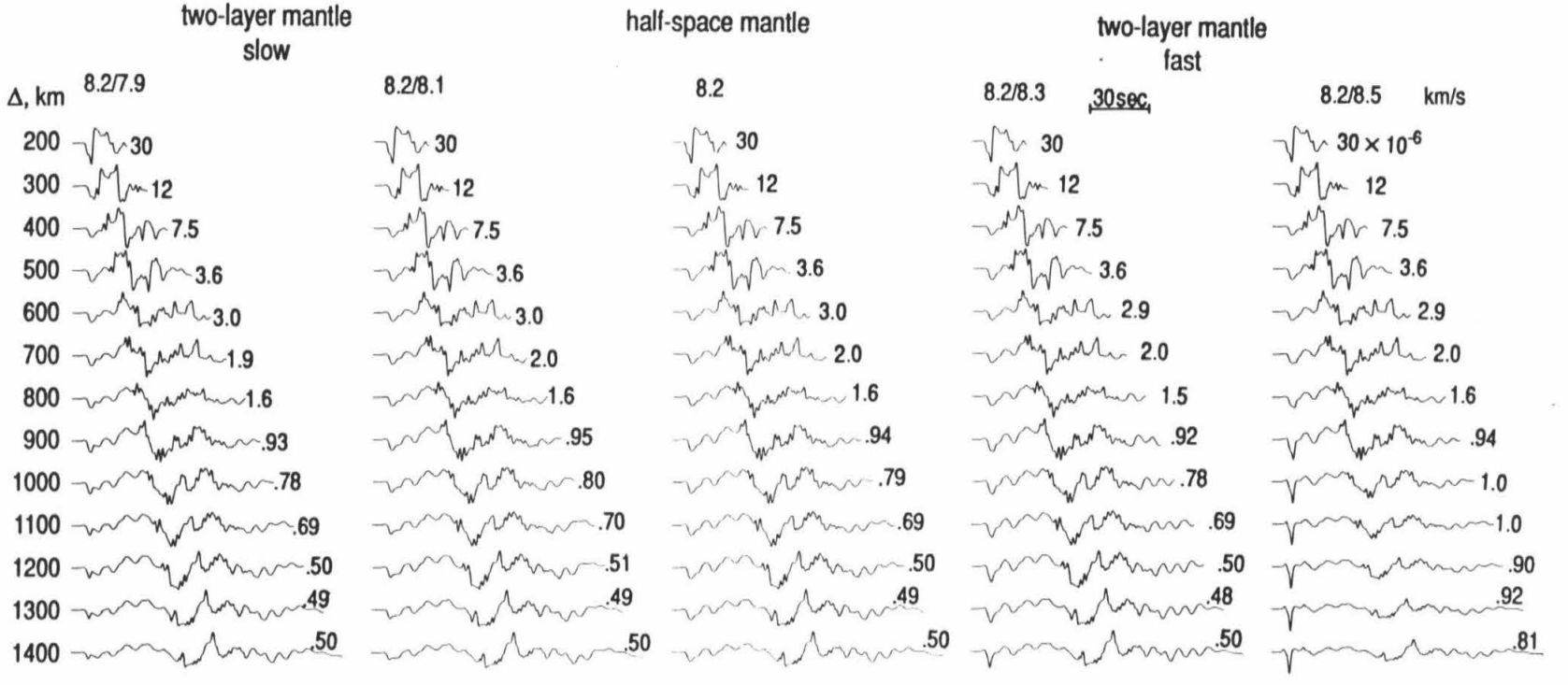

VERTICAL STRIKE-SLIP COMPONENT
LONG PERIOD WWSSN

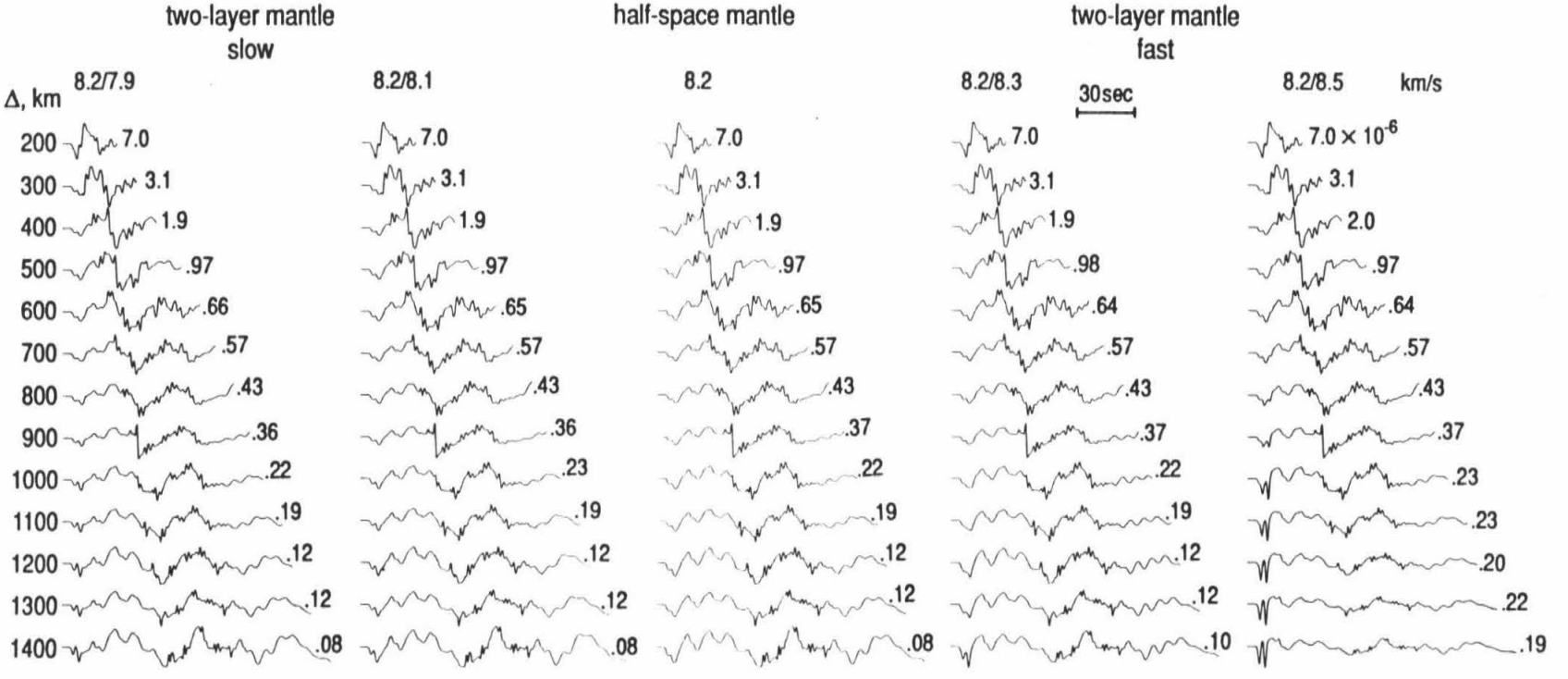

VERTICAL DIP-SLIP COMPONENT
LONG PERIOD WWSSN

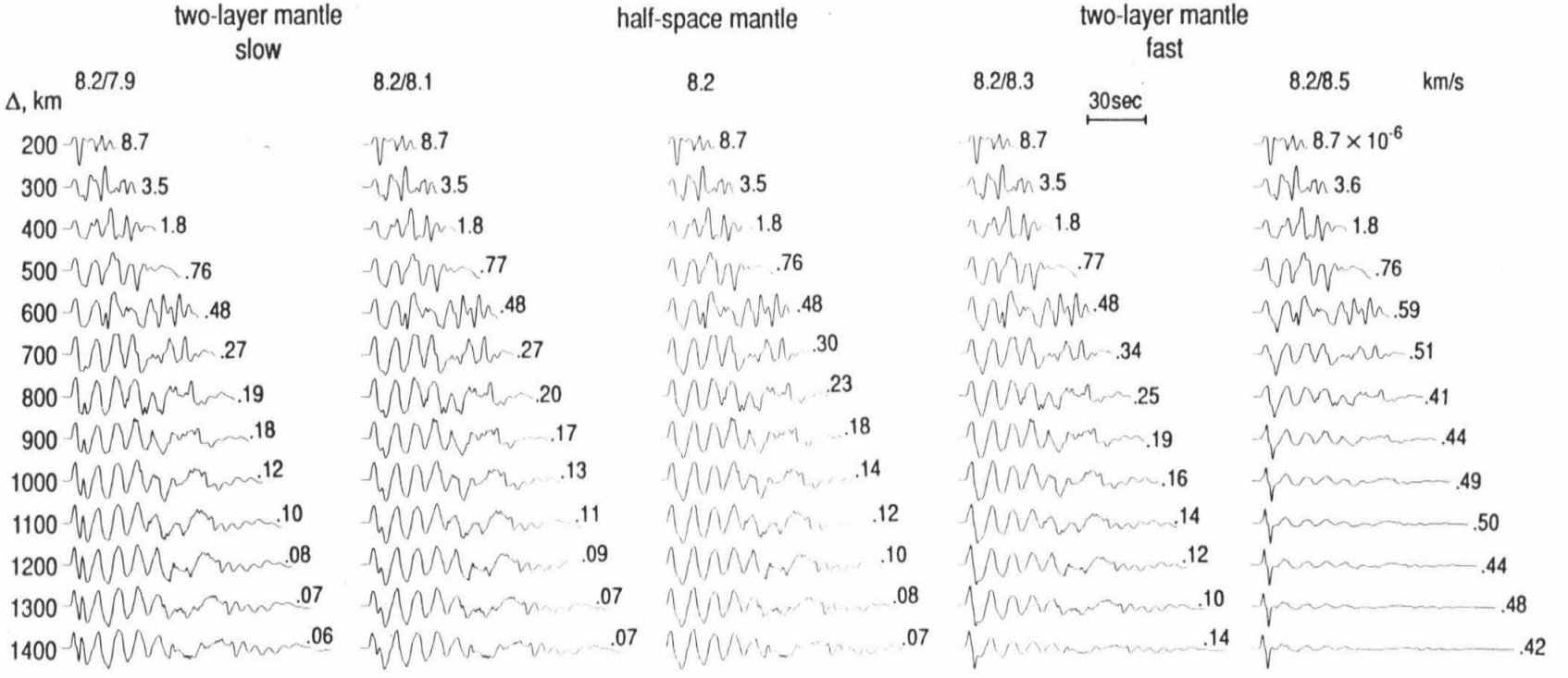

VERTICAL 45°-DIP-SLIP COMPONENT
LONG PERIOD WWSSN

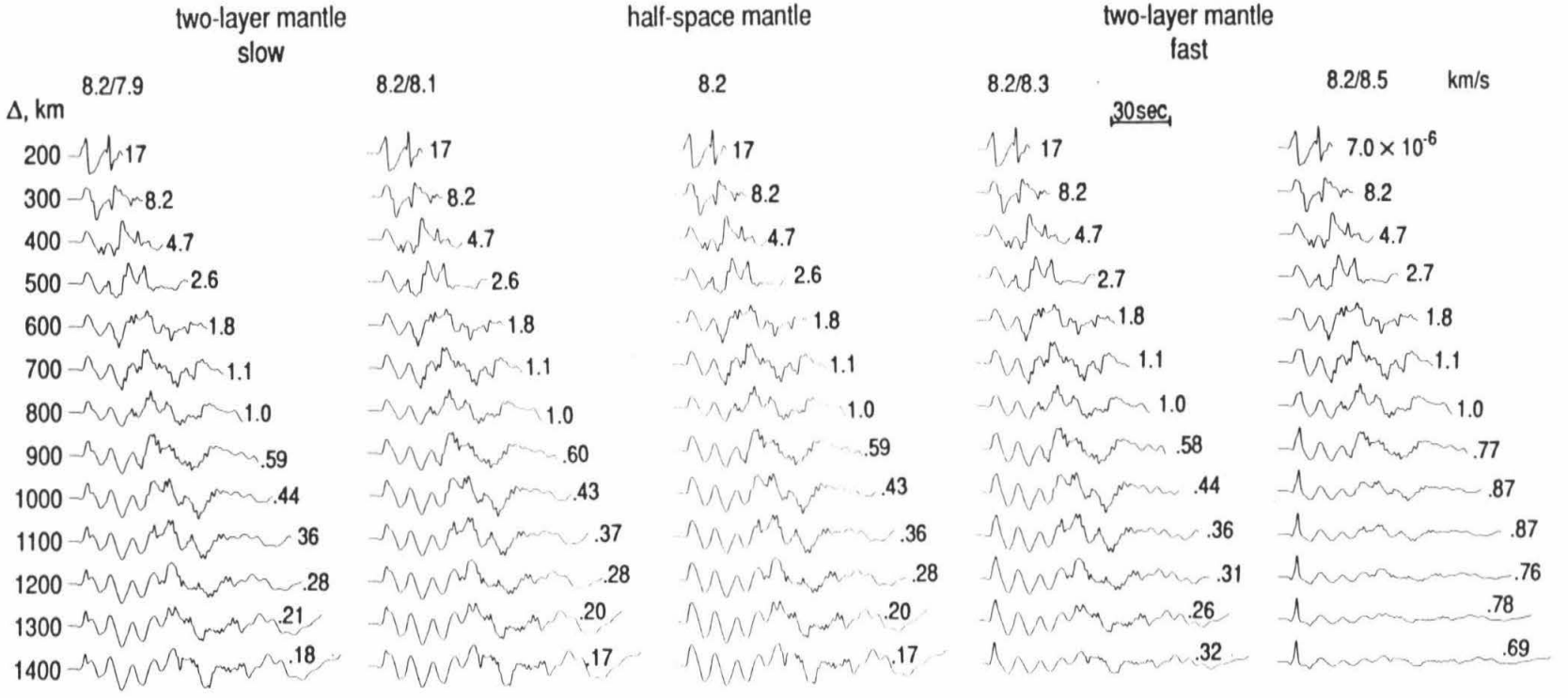

References

Anderson, D. L., The deep structure of continents, J. Geophys. Res., 84, 7555-7560, 1979.

Anderson, D. L., and J. D. Bass, Mineralogy and composition of the upper mantle, Geophys. Res. Lett., 11, 637-640, 1984.

Barr, K. G., Evidence for variations in upper mantle velocity in Hudson Bay area, Earth Science Symposium on Hudson Bay, Geol. Surv. Can. Pap., 68-53, 365-376, 1969.

Barr, K. G., Crustal refraction: Yellowknife 1966, J. Geophys. Res., 76, 1929-1947, 1971.

Berry, M. J., Structure of the crust and upper mantle in Canada, Tectonophysics, 20, 183-201, 1973.

Berry, M. J., and K. Fuchs, Crustal structure of the Superior and Grenville provinces of the northeastern Canadian Shield, Bull. Seismol. Soc. Am., 63, 1393-1432, 1973.

Berry, M. J. and J. A. Mair, The nature of the earth's crust in Canada, in The earth's crust, edited by J. G. Heacock, Am. Geophys. U. Monogr. No. 20, 319-348, 1977.

Brune, J. and J. Dorman, Seismic waves and earth structure in the Canadian Shield, Bull. Seismol. Soc. Am., 53, 167-200, 1963.

Burdick, L. J., A comparison of upper mantle structure beneath North America and Europe, J. Geophys. Res., 86, 5926-5936, 1981.

Burdick, L. J., and D. V. Helmberger, The upper mantle P velocity structure of the western United States, J. Geophys. Res., 83, 1699-1712, 1978.

Butler, R., Shear-wave travel times from SS, Bull Seismol. Soc. Am., 69, 1715-1732, 1979.

Carpenter, E. W., Absorption of elastic waves -- an operator for a constant Q mechanism, A. W. R. E. Rep. 0-43/66, U. K. At. Energy Auth., 1966.

Chandra, U., Seismicity, earthquake mechanisms and tectonics along the western coast of North America, from 42°N to 61°N, Bull. Seismol. Soc. Am., 64, 1529-1549, 1974.

Chapman, C. H., A first-motion alternative to geometrical ray theory, Geophys. Res. Lett., 3, 153-156, 1976.

Chapman, C. H., A new method for computing synthetic seismograms, Geophys. J. R. Astron. Soc., 54, 481-518, 1978.

Choy, G. L. and P. G. Richards, Pulse distortion and Hilbert transformation in multiply reflected and refracted bodywaves, Bull. Seismol. Soc. Am., 65, 55-70, 1975.

Cumming, G. L., G. D. Garland and K. Vozoff, Seismological measurements in southern Alberta, Final Rep. 1, Contract AF19 (604)-8470, 1-31, 1962.

Dainty, A. M., C. E. Keen, M. J. Keen, and J. E. Blanchard, Review of geophysical evidence on crust and upper-mantle structure of the eastern seaboard of Canada, Am. Geophys. U. Monogr., 10, 349-368, 1966.

Dey-Sarkar, S. K., and R. A. Wiggins, Upper mantle structure in western Canada, J. Geophys. Res., 81, 3619-3632, 1976.

Dziewonski, A. M., Mapping the lower mantle: Determination of lateral heterogeneity in P velocity up to degree and order 6, J. Geophys. Res., 89, 5929-5952, 1984.

Duffy, T. S., and D. L. Anderson, Seismic velocities in mantle minerals and the mineralogy of the upper mantle, J. Geophys. Res., 94, 1895-1912, 1989.

Futterman, W. I., Dispersive body waves, J. Geophys. Res., 67, 5279-5291, 1962.

Given, J. W., and D. V. Helmberger, Upper mantle structure of northwestern Eurasia, J. Geophys. Res., 85, 7183-7194, 1980.

Grand, S. P., Tomographic inversion for shear velocity beneath the North American Plate, J. Geophys. Res., 92, 14,065-14,090, 1987.

Grand, S. P., and D. V. Helmberger, Upper mantle shear structure of North America, Geophys. J. R. Astron. Soc., 76, 399-438, 1984.

Greenhalgh, S. A., Seismic investigations of crustal structure in east-central Minnesota, Phys. Earth Planet. Inter., 25, 372-389, 1981.

Gregersen, S., Surface wave dispersion and crustal structure in Greenland, Geophys. J. R. Astron. Soc., 22, 29-39, 1970.

Gurbuz, B. M., A study of the earth's crust and upper mantle using travel times and spectrum characteristics of body waves, Bull. Seismol. Soc. Am., 60, 1921-1935, 1970.

Hager, B. H., Subducted slabs and the geoid: constraints on mantle rheology and flow, J. Geophys. Res., 89, 6003-6015, 1984.

Helmberger, D. V., Numerical seismograms of long-period body waves from seventeen to forty degrees, Bull. Seismol. Soc. Am., 63, 633-646, 1973a.

Helmberger, D. V., On the structure of the low velocity zone, Geophys. J. R. Astron. Soc., 34, 251-263, 1973b.

Helmberger, D. V. and G. R. Engen, Modeling the long-period body waves from shallow earthquakes at regional ranges, Bull. Seismol. Soc. Am., 70, 1699-1714, 1980.

Herrmann, R. B., Surface-wave focal mechanisms for eastern North American earthquakes with tectonic implications, J. Geophys. Res., 84, 3543-3552, 1979.

Herrmann, R. B., C. A. Langston, and J. E. Zollweg, The Sharpsburg, Kentucky earthquake of 27 July 1980, Bull. Seismol. Soc. Am., 72, 1219-1239, 1982.

Hill, D. P., Velocity gradients and anelasticity from crustal body wave amplitudes, J. Geophys. Res., 76, 3309-3325, 1971.

Hobson, G. D., A. Overton, D. N. Clay, and W. Thatcher, Crustal structure under Hudson Bay, Can. J. Earth Sci., 4, 929-947, 1967.

Horsfield, W. T., and P. I. Maton, Transform faulting along the De Geer line, Nature, 226, 256-257, 1970.

Hunter, J. A. and R. F. Mereu, The crust of the earth under Hudson Bay, Can. J. Earth Sci., 4, 949-960, 1967.

Jordan, T. J., Continents as a chemical boundary layer, Philos. Trans. R. Soc. London, 301, 359-373, 1981.

King, D. W., and G. Calcagnile, P wave velocities in the upper mantle beneath Fennoscandia and western Russia, Geophys. J. R. Astron. Soc., 46, 407-432, 1976.

Langston, C. A., Aspects of P_n and P_g propagation at regional distances, Bull. Seismol. Soc. Am., 72, 457-471, 1982.

Langston, C. A. and D. V. Helmberger, A procedure for modeling shallow dislocation sources, Geophys. J. R. Astron. Soc., 42, 117-130, 1975.

LeFevre, L. V. and D. V. Helmberger, Source parameters of eastern North American earthquakes using P_{nl}, manuscript in preparation.

Lerner-Lam, A. L., and T. H. Jordan, How thick are the continents?, J. Geophys. Res., 92, 14,007-14,026, 1987.

Liu, H.-L., and H. Kanamori, Determination of source parameters of mid-plate earthquakes from the waveforms of body waves, Bull. Seismol. Soc. Am., 70, 1989-2004, 1980.

Masse, R. P., Compressional velocity distribution beneath central and eastern North America, Bull. Seismol. Soc. Am., 63, 911-935, 1973.

Mauk, F. J., C. Christensen, and S. Henry, The Sharpsburg, Kentucky, earthquake of 27 July 1980: mainshock parameters and isoseismal maps, Bull. Seismol. Soc. Am., 72, 221-236, 1982.

Mereu, R. F., and J. A. Hunter, Crustal and upper mantle structure under the Canadian Shield from Project Early Rise data, Bull. Seismol. Soc. Am., 59, 147-165, 1969.

Nabalek, J. L., Determination of earthquake source parameters from inversion of body waves, Ph.D. theses, 361 pp., Mass. Inst. of Technol., Cambridge, 1984.

Nakanishi, I., and D. L. Anderson, Measurements of mantle wave velocities and inversion for lateral heterogeneity and anisotropy --II. Analysis by the single-station method, Geophys. J. R. Astron. Soc., 78, 573-617, 1984.

Poupinet, G., On the relation between P-wave travel time residuals and the age of continental plates, Earth Planet. Sci. Lett., 43, 149-161, 1979.

Romney, C., B. G. Brooks, R. H. Mansfield, D. S. Carder, J. N. Jordan, and D. W. Gordon, Travel times and amplitudes of principal body phases recorded from GNOME, Bull. Seismol. Soc. Am., 52, 1057-1074, 1962.

Ruffman, A., and M. J. Keen, A time-term analysis of the first arrival data from the seismic experiment in Hudson Bay, 1965, Can. J. Earth Sci., 4, 901-928, 1967.

Simpson, D. W., R. F. Mereu, and D. W. King, An array study of P-wave velocities in the upper mantle transition zone beneath northeastern Australia, Bull. Seismol. Soc. Amer., 64, 1757-1788, 1974.

Soller, D. R., R. D. Ray, and R. D. Brown, A new global crustal thickness map, Tectonics, 1, 125-151, 1982.

Somerville, P. G., J. P. McLaren, L. V. LeFevre, R. W. Burger, and D. V. Helmberger, Comparison of source scaling relations of eastern and western North American earthquakes, Bull. Seismol. Soc. Am., 77, 322-346, 1987.

Stauder, W., and O. W. Nuttli, Seismic studies: south central Illinois earthquake of November 9, 1968, Bull. Seismol. Soc. Am., 60, 973-981, 1970.

Stork, C., and D. Helmberger, A new velocity profile for the Eurasian shield, Eos Trans. AGU, 66, 310, 1985.

Tanimoto, T., The Backus-Gilbert approach to the three-diminsional structure in the upper mantle -- I. Lateral variation of surface wave phase velocity with its error and resolution, Geophys. J. R. Astron. Soc., 82, 105-123, 1985.

Walck, M. C., The P-wave upper mantle structure beneath an active spreading center: The Gulf of California, Geophys. J. R. Astron. Soc., 76, 697-723, 1984.

Wallace, T. C., Long period regional body waves, Ph.D. thesis, 180pp., Calif. Inst. of Technol., Pasadena, 1983.

Wallace, T. C., and D. V. Helmberger, Determining source parameters of moderate-size earthquakes from regional waveforms, Phys. Earth Planet. Int., 30, 185-196, 1982.

Wallace, T. C., D. V. Helmberger, and G. R. Mellman, A technique for the inversion of regional data in source parameter studies, J. Geophys. Res., 86, 1679-1685, 1981.

Wickens, A. J., Variations in lithospheric thickness in Canada, Can. J. Earth Sci., 8, 1154-1162, 1971.

Wickens, A. J., and G. G. R. Buchbinder, S-wave residuals in Canada, Bull. Seismol. Soc. Am., 70, 809-822, 1980.

Wiggins, R. A., Body wave amplitude calculations -- 2, Geophys. J. R. Astron. Soc., 46, 1-10, 1976.

Wiggins, R. A., and D. V. Helmberger, Upper mantle structure of the western United States, J. Geophys. Res., 78, 1870-1880, 1973.

Woodhouse, J. H., and A. M. Dziewonski, Mapping the upper mantle: three-diminsional modeling of earth structure by inversion of seismic waveforms, J. Geophys. Res., 89, 5953-5986, 1984.

Zandt, G., and G. E. Randall, High P-velocity in the shallow mantle beneath E. North America, Eos Trans. AGU, 67, 302, 1986.